Leibniz-Institut für Astrophysik Potsdam

Growth and Saturation of Dynamo in Spiral Galaxies via Direct Simulations

Dissertation
zur Erlangung des akademischen Grades
"doctor rerum naturalium"
(Dr. rer. nat.)
in der Wissenschaftsdisziplin Astrophysik

eingereicht an der
Mathematisch-Naturwissenschaftliche Fakultät
der Universität Potsdam

von
Abhijit B. Bendre

Potsdam, February 2018

Published online at the
Institutional Repository of the University of Potsdam:
URN urn:nbn:de:kobv:517-opus4-407517
http://nbn-resolving.de/urn:nbn:de:kobv:517-opus4-407517

Abstract

We do magnetohydrodynamic (MHD) simulations of local box models of turbulent Interstellar Medium (ISM) and analyse the process of amplification and saturation of mean magnetic fields with methods of mean field dynamo theory. It is shown that the process of saturation of mean fields can be partially described by the prolonged diffusion time scales in presence of the dynamically significant magnetic fields. However, the outward wind also plays an essential role in the saturation in higher SN rate case. Algebraic expressions for the back reaction of the magnetic field onto the turbulent transport coefficients are derived, which allow a complete description of the nonlinear dynamo. We also present the effects of dynamically significant mean fields on the ISM configuration and pressure distribution. We further add the cosmic ray component in the simulations and investigate the kinematic growth of mean fields with a dynamo perspective.

Zusammenfassung

Wir führen magnetohydrodynamische (MHD) Simulationen des turbulenten interstellaren Mediums (ISM) in lokalen Boxen durch und analysieren darin den Prozess der Verstärkung und Saturation der mittleren Magnetfelder mit Methoden der Dynamotheorie mittlerer Felder. Es wird gezeigt, dass der Prozess der Saturation mittlerer Felder teilweise durch eine verl ängerte Diffusionzeit in Gegenwart dynamisch signifikanter Magnetfelder erklärt werden kann. Für höhere Supernovae-Raten spielt auch der nach außen treibende Wind eine essenzielle Rolle für die Saturation. Aus den Simulationen konnten algebraische Formeln für die Rückwirkung des Magnetfeldes auf die turbulenten Transportkoeffizienten abgeleitet werden, die eine vollständige Beschreibung des nichtlinearen Dynamos erlauben. Wir präsentieren zudem den Einfluß signifikanter mittlerer Magnetfelder auf die ISM-Konfiguration und Druckverteilung. Wir fügen der Simulation außerdem kosmische Strahlung als Komponente hinzu und untersuchen das kinematische Wachstum mittlerer Felder aus einer Dynamo-Perspektive.

Contents

List of Figures

List of Tables

Abbreviations

MHD	**M**agneto**h**ydro**d**ynamics
ISM	**I**nter**s**tellar **M**edium
IGM	**I**nter**g**alactic **M**edium
CR	**C**osmic **R**ays
RM	**R**otation **M**easure
SN	**S**uper**n**nova
UV	**U**ltra **V**iolet
FUV	**F**ar **U**ltra **V**iolet
PAH	**P**olicyclic **A**romatic **H**ydrocarbon

Physical Constants

Speed of Light	c	=	$2.997\ 924\ 58 \times 10^{8}\ \mathrm{ms}^{-\mathrm{S}}$
Vacuum Permittivity	ϵ_0	=	$8.854\ 187\ 82 \times 10^{12}\mathrm{Fm}^{-1}$
Vacuum Permiability	μ_0	=	$4\pi \times 10^{-7}\mathrm{NA}^{-2}$
Gravitational Constant	G	=	$6.672\ 84 \times 10^{-11}\mathrm{Nm}^2\mathrm{s}^{-2}$
Atomic Mass Unit	Da	=	$1.660\ 57 \times 10^{-27}\mathrm{kg}$
Solar Mass	$M_\odot$	=	$1.989\ 10 \times 10^{30}\mathrm{kg}$
Solar Radius	$R_\odot$	=	$6.955\ 00 \times 10^{5}\mathrm{km}$
Parsec	pc	=	$3.085\ 68 \times 10^{16}\mathrm{m}$

Symbols

$x/y/z$	distance
t	time
ρ	mass density
$\mathbf{u}$	velocity
p	pressure
$\mathbf{B}$	magnetic field
Ω	angular frequency
g	acceleration due to gravity
T	temperature

Chapter 1

Introduction

1.1 Cosmic Magnetic Fields

Discovery of the existence of magnetic fields in the sunspots [Hale, 1908] has a cardinal relevance to the area of cosmic magnetic fields. Since then, the ubiquity of magnetic field in astronomical objects such as stars, galaxies, protostellar jets, etc. has been supported by an extensive amount of observational data.

Several observations from astrophysics and geology have enabled us to map a detailed spaciotemporal behavior of magnetic field in the celestial objects and in the earth itself [Hathaway, 2010; Love, 2008]. The Solar magnetic field, for instance, evolves in a periodic way, with time period of 22 years (Figure 1.1) and it could be as strong as 3 kG locally. While the Earth's magnetic field is relatively static and dipolar in geometry (although there is ample evidence of temporally irregular flips in its the polarity, that have occurred in the past) and has the average strength of ~ 0.5 G at the surface of the Earth.

Reason for the magnetization of most of the astronomical bodies is usually attributed to the induction effect generated by the motions of electrically conducting plasma [Moffatt, 1978], which can be promisingly encapsulated in a so-called 'dynamo mechanism', a mechanism that converts kinetic energy into magnetic energy [Krause & Rädler, 2013]. Due to its wide range of applicability from stars to the whole galaxies, 'dynamo theory' is considered as one of the most useful tools to explain the peculiarities of observed magnetic fields in these celestial bodies [Rüdiger & Hollerbach, 2006]. However, with the advancement in available computational resources, it is possible to investigate the

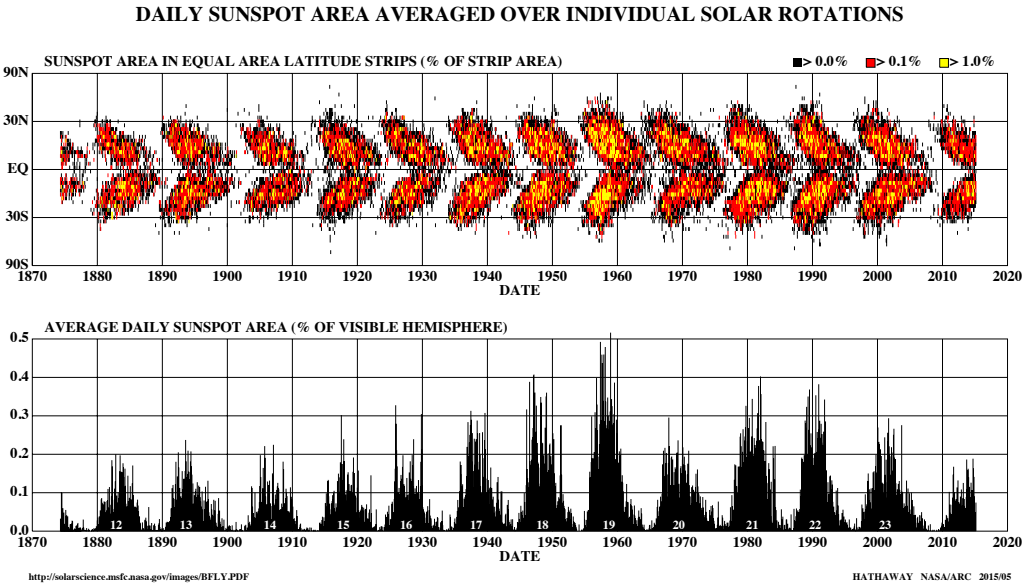

FIGURE 1.1: *Panel-top*: Sunspot area (measured in the units of, equal area latitude stripes) as a function of time and latitude. *Panel-bottom*: Total sunspot area (measured in the units of, visible solar disc area) as a function of time. [Adopted from, Hathaway, 2010].

question of existence of magnetic fields in these objects, to some extent, relying on the first principles [e.g. Glatzmaiers & Roberts, 1995; Ossendrijver, 2003]. While extending this philosophy to explain the galactic magnetic fields (which also is the main focus of this analysis), one is confronted with a number of open questions, which are sequentially discussed in the following sections.

1.2 Galactic Magnetic Fields

1.2.1 Radio Synchrotron Observations

Unlike for the stellar and geomagnetic fields, confirmation of galactic magnetic fields is relatively recent. In fact, only over the course last few decades have observations of the polarized radio synchrotron emission been established as an efficient tool in mapping

the galactic magnetic field, both in strength and geometry [Beck et al., 1996]. A brief summary of this method is as follows:

Supernova shock waves and protostellar jet flows accelerate the charged particles to the relativistic velocities, which are referred to as the cosmic rays (CR). An ensemble of CR electrons gyrating around the galactic magnetic field lines (due to Lorentz force) emit the highly polarized beam of synchrotron radiation in the direction of gyration. Frequency of the synchrotron radiation depends simply upon energy of the gyrating CR particle and strength of magnetic field. The synchrotron radiation we receive from galactic CR belong to the radio range of electromagnetic spectrum [Fermi, 1949; Kiepenheuer, 1950] and are linearly polarized. Its theoretically expected degree of polarization would approximately be 74% if the magnetic fields were purely regular [Beck & Wielebinski, 2013], while the integrated fluctuating component of magnetic field within a particular observed 'pixel' of the galaxy (plus the contribution of unpolarized thermal emission, which may be dominant in the star forming regions) amounts to a certain departure from expected degree of polarization (74%). Hence this departure is used as a measure of the comparative contribution of regular and turbulent magnetic field. It should, however, be mentioned here that the theoretical estimate of the degree of polarization relies upon the approximation of isotropy of fluctuating magnetic field and any anisotropy in it could systematically lead to the overestimation of regular magnetic field. Anisotropy arising form the galactic differential rotation, for example, could lead to additional polarization of $\sim 10\%$ [e.g. Stepanov et al., 2014].

The estimation of total (regular + turbulent) field strength is usually obtained by employing an assumption of equipartition between CR energy and magnetic energy. This assumption makes total intensity of synchrotron radiation a quantitative measure of total field strength [e.g. Arbutina et al., 2012]. It must also be mentioned that the assumption of equipartition may lead to the over/underestimated value of total magnetic fields in several scenarios. If for instance, the CR energy losses are prevalent (e.g. in presence of strong magnetic fields) the equipartition assumption, instead of its true value actually provides a lower limit of the total field strength [Beck & Wielebinski, 2013; Yoast-Hull et al., 2015]. The equipartition argument should hence rather be treated as a first order estimate of the total field strength. Nonetheless, recent γ-ray observations seem to support the validity of the equipartition argument in few cases such as Large Magellanic Cloud, Milky Way, M 82, etc. [Lacki & Beck, 2013; Mao et al., 2012].

To map the topology of regular galactic magnetic field, however, it is indispensable to disentangle its line of sight and perpendicular component, which is achieved as follows. Firstly, to infer the direction of a perpendicular field component (perpendicular to the line of sight) a distinguishing property of the galactic synchrotron radiation is employed, that is, a significantly high degree of plane polarization, wherein the electric field vectors of the radiation stay perpendicular to background magnetic field. By employing this phenomenon, it is in-principle possible to infer the direction of a perpendicular component (with the ambiguity of 180^o). This plane of polarization further gets rotated as the radiation passes through galactic ISM, due to the Faraday effect. The Faraday rotation angle, under certain justifiable approximations, remains directly proportional to the squared of wavelength of radiation and to the strength of a line of sight field component (which is embedded in a so-called rotation measure, RM) [e.g. Sofue et al., 1986; Sokoloff et al., 1998]. Positive and negative values of RM, thus imply a line of sight field component, which is directed towards the telescope and away from it, respectively. A multi-wavelength analysis of RM, along with the independent estimates of total field strength yield the strength of a perpendicular field component as well.

By performing such analysis over a wide range of radio frequencies one can separately map the line of sight and perpendicular components of regular galactic magnetic field. However, the reliability of these results within the far galactic halos (which emit low radio frequency radiation) has to be weighted against the increasing contribution of unpolarized emission and CR loss processes, which makes it utmost necessary to carry out the high resolution imaging of a low radio frequency data [e.g. Van Haarlem et al., 2013]. A few observational findings about galactic magnetic fields are discussed in the following sections.

1.2.2 Face-On Galaxies

As of now, it is a well established observational fact that in most of the disc galaxies regular magnetic field has a spiral structure (with the strength of μG) that roughly follows optical gas arms. This spiral pattern extends over tens of kpc [e.g. Beck, 2009]. Even the galaxies that lack regular structure of optical gas arms seem to posses a fairly coherent magnetic spiral structure, exceeding well over few tens of kpc [e.g. Chyży & Buta, 2008]. In spite of the regular structure, a general decoupling between galactic

magnetic fields and gas flows exists, or in other words, a finite pitch angle between a gas flow direction (which is approximately circular) and magnetic field vectors. Remarkably large values of pitch angles (8^o - 40^o) have so far been reported in many face-on spirals [e.g. Fletcher et al., 2011; Tabatabaei et al., 2008].

Figure 1.2, as a typical example, shows a polarized synchrotron intensity map for a nearby face-on spiral galaxy NGC 4736, in which all the aforementioned characteristics of regular galactic magnetic fields are clearly represented. For instance, magnetic spiral arms extend well over a 10 kpc range, with a strength of the total and regular fields of approximately 17 μG and 10 μG, respectively (at 8.6 GHz). Even the average value of pitch angles is fairly large, $\sim 35^0$ [Chyży & Buta, 2008]. In the recent statistical analysis of the magnetic field data in spiral galaxies [Van Eck et al., 2015], pitch angles are shown to systematically scale with the SN rate, so that a linear correlation exists with a very small error of $\sim 2\%$, moreover there also is a clear direct scaling between pitch angles and total gas surface density. Although the size of the data sample they have used for this analysis is not statistically significant, it revels some of the interesting features of the galactic parameters and their mutual correlations.

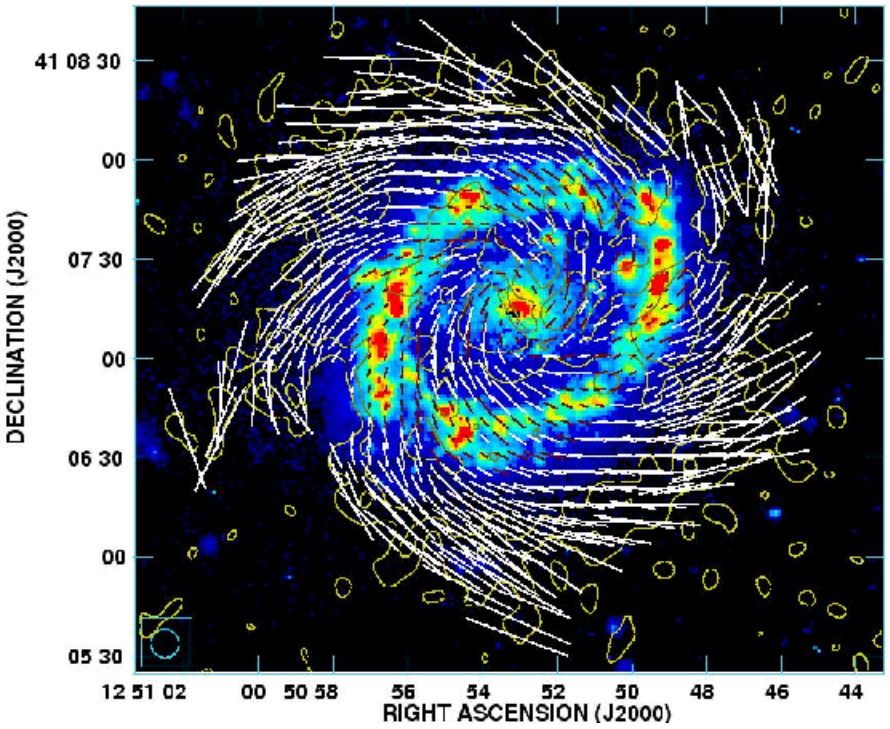

FIGURE 1.2: Polarized intensity contour map at 8.46 GHz for NGC 4736 face-on galaxy, with observed magnetic field vectors overlaid on the optical image for same galaxy. [Adopted from, Chyży & Buta, 2008].

1.2.3 Edge-On Galaxies

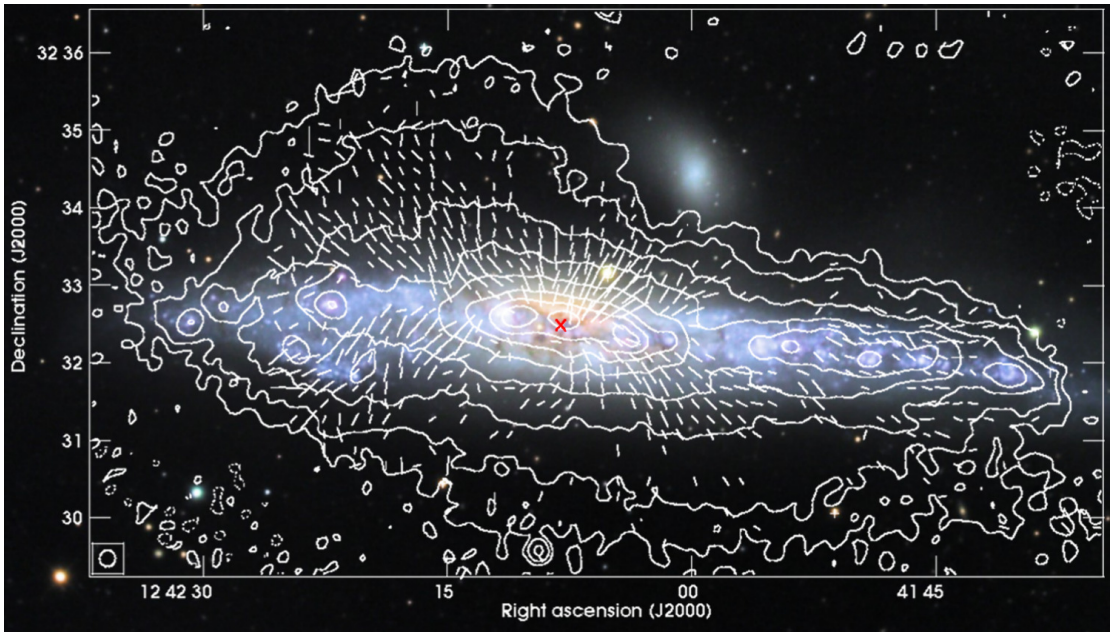

FIGURE 1.3: Polarized radio intensity map of edge-on spiral galaxy NGC 4631 at 4.85 GHz, overlaid on a color-scale optical DSS image, contours represent the apparent magnetic field orientation. [Adopted from, Mora & Krause, 2013].

Observations of radio synchrotron emissions from the galaxies seen edge-on suggest that many galaxies posses a thick radio intensity halo encapsulating the disc. Brightness of this radio halo decays with a distance from the galactic disc, which can be fitted with an exponential curve [e.g. Beck, 2001; Dumke & Krause, 1998]. Consequently the exponential scale-height of a radio halo becomes a measure for the vertical extent of total magnetic field (by assuming equipartition between CR and magnetic energy), such that the scale-height of total field is almost 4 times larger than the synchrotron scale-height [1]. Typical galactic radio halos can be best fitted with the superimposition two exponential curves of scale-heights $\sim 350\,\mathrm{pc}$ and $\sim 1.8\,\mathrm{kpc}$ [e.g. Krause, 2014, 2015], which gives an average scale-height of $\sim 8\,\mathrm{kpc}$ for the total magnetic fields in outer parts of the galaxies.

Similar to its vertical distribution, brightness of the radio halo in many spiral galaxies exponentially decays in radially outward direction, with average scale-lengths of about $4\,\mathrm{kpc}$ (which gives the radial scale-lengths of $15\,\mathrm{kpc}$ for the total magnetic field) [Beck & Wielebinski, 2013]. Total magnetic energy even exceeds the turbulent kinetic energy

[1] However, it must be mentioned that a vertical extent of the radio halos is also controlled by other CR loss processes like inverse Compton, adiabatic losses, etc.

as we go radially outwards. In certain cases [e.g. Beck, 2007] this turnover occurs only at $\sim 2\,\mathrm{kpc}$.

Polarized synchrotron observations of edge-ons also reveal a specific topology of regular fields, which is characterized by the strong regular fields that remain parallel to the disc near the galactic center and deflect in vertical direction in the radially outer parts of the disc. As a result, typical 'X-shaped' geometry of the polarization vectors is observed in the edge-on view of most spiral galaxies, even in those galaxies with a low star formation rate. As a typical example, Figure 1.3 shows a radio polarization intensity map of a nearby edge-on spiral galaxy NGC 4631, in which a thick radio halo and the X shaped pattern is clearly seen. Overall geometry of the regular field, however, is difficult to interpret in a side view, due to inability to disentangle the radial field from the toroidal field but a plausible reason for the observed X shape probably lies in the advective transport of total field due to fast galactic outflows emerging from the disk. Estimated velocities of such outflows in many nearby galaxies, scale roughly as a direct function of SN rate and average strength of the total field [e.g. Krause, 2012]. Implications of the strong outward winds on magnetic field evolution can be understood via numerical simulations, which have been discussed further in this thesis, but to formulate the question properly (Section 1.3), a few observational findings of galactic magnetic fields (which are also explored in further chapters) are summarized below.

1. Galactic magnetic fields show a long range regularity both in radial and vertical directions.

2. Face-on observations show significantly large values pitch angles; even beyond the regular optical arms.

3. Strengths and the vertical scale-heights of the regular galactic fields are seemingly uncorrelated with SN rate.

4. Large ratios of turbulent to regular magnetic fields exist in the galaxies and scale inversely with respect to star formation rate [Chyży & Buta, 2008].

1.3 Overview and Objectives of Numerical Models

On the length scales larger than the mean free path of galactic ISM, it can be described as a vastly inhomogeneous turbulent fluid, one of the important drivers of which is ongoing stellar evolution that leads to the SN explosions on the time scale of $\sim$ Myr and releasing energy of the order of $\sim 10^{51}$ erg into ISM per explosion. Overpressured bubbles of hot ISM gas created during the SN explosions rapidly expand until the SN remnant merges in the surrounding ISM by releasing its thermal and kinetic energy (i.e. until its velocity matches that of the surroundings). Radiative cooling time of such hot gas usually exceeds the turbulent correlation time and, as a result, galactic ISM evolves to a complex turbulent structure characterized by the distinct thermal phases, which can be broadly classified into: *i*) the warm phase, which is strongly ionized by various sources like UV, x-ray, cosmic rays, shock waves, etc., *ii*) the hot phase, which is created mainly as a result of random SN explosions, and *iii*) the cold molecular phase, which is generated as a result of cooling down of interacting SN shock fronts [Shukurov, 2004]. Another important feature of galactic ISM is the vertical stratification arising as a result of non-uniformly vertically distributed SN explosions (these depend upon the distribution of underlying stellar population). This, along with the gravity, leads to a particular vertical arrangement of ISM phases such that the occupancy fraction of lighter hot gas in the galactic disc is lower than in the outer halo, as opposed to the denser phases, which mostly occupy the galactic disc. So, using the first principles, galactic ISM can be viewed as the electrically conducting turbulent fluid and origin of galactic magnetic field as a Magnetohydrodynamical problem.

While explaining the long range regularity of galactic spirals it is natural to attribute its origin to the galactic flow pattern (a passive kinematic winding up of 'frozen in' primordial fields due to the galactic differential rotation). However, the existence of large pitch angles makes this argument less compelling. The large values of turbulent diffusivity ($10^{26}\,\mathrm{cm^2\,s^{-1}}$), on the other hand, could in principle prevent the strong winding up of azimuthal component, but would also lead to the decay of non-axisymmetric magnetic field within $\sim 1.5\,\mathrm{Gyr}$ [Rohde et al., 1998; Shukurov, 1998]. Both of these arguments support the possibility of the existence of a dynamical process governing the field generation. Initial attempts to formulate the mechanism were based upon the mean field theory via a so-called $\alpha\Omega$ dynamo model. Qualitatively speaking, $\alpha\Omega$-dynamo is a

mechanism through which weak 'seed' fields are amplified to large scale regular fields by deriving the energy from the rotational kinetic energy of the system via helical turbulence. This amplification continues until the magnetic fields become strong enough to affect the structure of turbulence. Before elaborating this point; some general technical details of the formulation are discussed.

In mean field dynamo theory, the flow variables (velocity and magnetic field) are split as a sum of their mean and fluctuating/turbulent component. Evolution of the mean magnetic field is then studied for mean flow (velocity) and 'the turbulent electromotive force' (EMF), $\mathcal{E} = \overline{(\mathbf{u}' \times \mathbf{b}')}$ (mean value of the crossproduct of the fluctuating velocity $\mathbf{u}'$ and fluctuating magnetic field $\mathbf{b}'$). With the first order smoothing approximation, $\mathcal{E}$ turns out to be a linear functional of the mean field and its derivatives, with α and η as the multiplying factors. α and η are referred to as the dynamo coefficients for obvious reasons and are interpreted as the 'helicity' and 'diffusivity' of the turbulence, respectively [see e.g. Krause & Rädler, 2013; Moffatt, 1978].

In order to visualize how this mechanism works for galaxies, one needs to take into account the underlying gas dynamics, which is traced by probing the Doppler shifts of stellar spectra. Rotation curves of most of the galaxies (rotational velocity as a function of galactic radial distance) thus measured correspond to the rigid rotation in the radially inner parts of galaxies (below $\sim 5\,\mathrm{kpc}$), while they are flat (indicating the differential rotation) in outer parts, introducing radial shear. Considering its geometry, a disc galaxy can be easily described with a cylindrical coordinate system, with origin placed at the galactic center. Background flow velocity, therefore, has an azimuthal component of rotation. Moreover, there also is a turbulence driven by supernova explosions, which gives rise to hot bubbles of ISM gas, expanding and rising up in the galactic halos. If the initial field were plane parallel, upward rising bubbles would carry the frozen in field along with them producing field loops. Furthermore, such rising bubbles would experience the Coriolis force making these loops twisted. The extent to which the loops will be twisted is encapsulated in the helicity of the turbulent bubble, which is denoted by the quantity α. On the other hand, any radial field component is spirally wound up along with differentially rotating disc, denoted by the Ω effect. Successive rising and twisting of field lines provides a robust mechanism to produce the toroidal (azimuthal) field from the poloidal (radial + vertical) and vice versa. If there were no sufficient α effect; spirally wound up field lines would lead to the negligible pitch angles, contrary

to what is observed in real galaxies. This mechanism is well depicted in Figure 1.4. Thus, this mechanism in principle explains the field amplification process against the diffusive losses along with appropriate values of pitch angles [e.g. Kleeorin et al., 2002; Stix, 1975; Zeldovich et al., 1983]. However, the used values of dynamo coefficients so far relied upon the phenomenological estimates based on the assumed properties of background turbulence, which does not necessarily provide a quantitative description of ISM turbulence. In order to figure out whether this simplistic mechanism describes an actual physical process that would lead to the production of galactic magnetic field, it is necessary to perform the direct MHD simulations of galactic ISM, starting from the first principles along with a realistic source of turbulence driving (usual sources include: SN explosions, jets, instabilities, etc.). The results of such simulations are then need to be analyzed in a context of $\alpha\Omega$-dynamo. Based upon the different mechanisms of turbulence driving, there have been a number of successful attempts of modeling a realistic galactic ISM, for instance Gressel [2010], much similar to Gent et al. [2012], have performed such realistic MHD simulations of a local 3D patch of a spiral galaxy, in which random SN explosions were used to drive the turbulence. Another example is Hanasz et al. [2009], in which SN explosions inject CR energy into the system. All of these models successfully capture the initial fast amplification phase of magnetic field when they are sufficiently smaller than the background turbulent kinetic energy.

In order to adequately examine the properties of galactic magnetic fields and its back-reaction on the ISM properties, one needs to perform such simulations in the regime where total magnetic fields would be sufficiently stronger to reflect the realistic scenario discussed previously (desirably as strong as the turbulent kinetic energy). Phenomenological considerations suggest a general suppression of background turbulence under the influence of dynamically significant mean magnetic fields [Krause & Rädler, 2013]. Helicity and turbulent diffusivity, as a result, should become the inverse functions of mean field itself. Dynamo models based on these hypotheses also have a fast growing solution initially, that saturates when magnetic energy reaches to equipartition with respect to the turbulent kinetic energy [Brandenburg & Sandin, 2004; Elstner et al., 2008; Shukurov et al., 2006]. However, there are a number of problems associated with such models. The first one of them is related to the mathematical description for the suppression of dynamo coefficients, which is usually derived using the order of magnitude estimates based on the phenomenological description. The second problem arises due to assumed

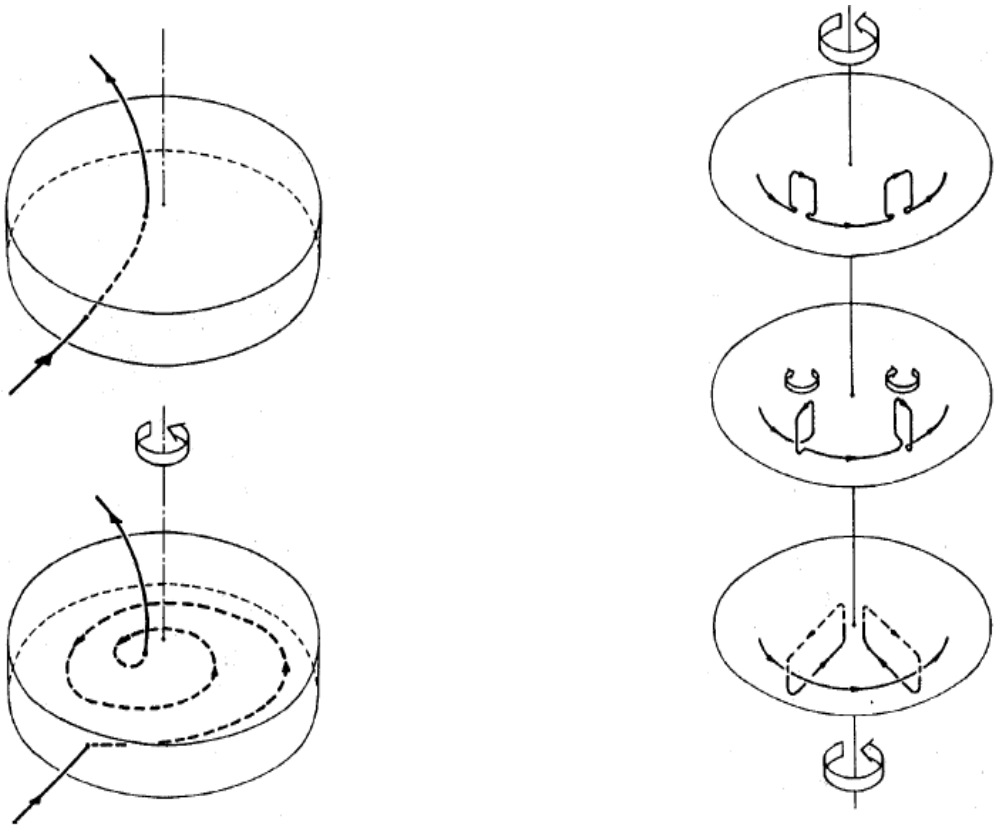

FIGURE 1.4: *Panel-left*: Spiral winding of poloidal field component to toroidal by the virtue of differential rotation (Ω effect). *Panel-right*: Helical twisting of toroidal field component to toroidal due to turbulent helicity (α effect). [Adopted from, Ruzmaikin et al., 2013]

suppression of poloidal field component along with the spiral winding amplification of toroidal component in the differentially rotating flow, a scenario which invariably leads to unrealistically small values of pitch angles.

Composition of realistic galactic ISM, however, involves more complexities than that. As has been mentioned before, the empirical estimates based on the observational findings suggest the existence of fast outward galactic wind in many edge-on spirals, the magnitude of which scales directly with respect to SN rate [Krause, 2012]. Such fast outward winds supposedly have a key roll in the saturation of magnetic fields via the advective transport of small scale current helicity, while preserving the helicity and thereby the value of pitch angle.

A self consistent verification of these processes can only be provided via the magnetohydrodynamic simulations of galactic ISM along with the realistic physical effects important for the dynamo amplification, such as a realistic mechanism for turbulence

driving, a vertical stratification of mass density (which provides a vertical pressure gradient) and the differential rotation. In the present investigation, it is attempted to provide a rigorous explanation for aforementioned problem by comparing the results of realistic simulations with the analytical formulation.

We also present preliminary results of the models involving the cosmic ray component, which in the reality primarily contain the relativistic protons and electrons. Observed energies of these cosmic rays range from ~ 1 GeV to $\sim 10^{11}$ GeV [e.g. Duric, 1988, 1999; Shapiro et al., 1991], thus making them one of the nonnegligible dynamical ingredients of the galactic ISM. SN shocks are thought to have a key roll in energizing the charged particles (produced via stellar processes) to such high magnitudes [e.g. Fermi, 1949, 1954]. The observed spectrum of cosmic rays is fairly smooth with a spectral index of ~ -2.7, which advocates the 'diffusive shock acceleration of SN remnants' as a plausible mechanism of producing the cosmic rays, as suggested by Bell [1978]. Since the cosmic rays are charged particles, their confinement to the large SN remnants is usually attributed to the observed strong magnetic fields frozen within the shock fronts [Bell, 2004]. As the magnetic fields are closely coupled to the thermal plasma, cosmic rays are also correlated to thermal background [e.g. Hanasz & Lesch, 2000]. It is therefore attempted here to explore the possible implications of cosmic rays to the large scale galactic dynamo mechanism [e.g. Boulares & Cox, 1990]. Previous investigations and discussions about the topic involved Parker's idea [Parker, 1992] of the enhanced galactic dynamo action due to additional buoyant support associated with cosmic ray component. More recently, Hanasz et al. [2009] have also demonstrated the initial fast amplification of magnetic fields via direct MHD simulations. It is therefore interesting to analytically verify this process, mainly because of the ability of the analytical approach to provide a self-consistent parametrization of background turbulence. Details of the implementation are provided in the relevant chapters, but the general idea of the mechanism involves the commonly used hydrodynamic approach for CR propagation (in which CR component is treated as an adiabatic fluid that gets injected in ISM via SN explosions and propagates along the magnetic field lines). We do not have much data yet to exclusively point out the differences between thermal SN driven turbulence and CR driven turbulence. Nevertheless, it is attempted here to verify the field amplification as a mean field process.

Chapter 2

Modelling the Interstellar Medium

Our primary aim is to understand the dynamo process in the galactic ISM; with a realistic mechanism of turbulence driving, which supposedly is a plausible reason for the existence of large scale galactic magnetic fields [Beck, 2007]. General background and astrophysical relevance of this conundrum has been adequately formulated in the introduction part of this thesis (Chapter 1). In this chapter we continue with the description of the numerical model. A number of physical effects have been incorporated here, such as SN explosions (with clustering), radiative heating and cooling, resistive and diffusive processes, vertical density stratification, differential rotation and the shear, etc. A reason behind implementation of all these effects is primarily to construct the most realistic numerical model of galactic ISM, which includes the necessary helical turbulence for galactic dynamo to function. Numerical descriptions of these effects are mainly adopted from theory and previous simulations by Gent et al. [2012]; Gressel et al. [2008], etc. To complement this model, we have further included the CR component, which is largely adopted from Hanasz et al. [2009] and Girichidis et al. [2014]. Numerical treatment for CR is discussed in the last part of this chapter. Having said that, we have excluded a number of other physical effects such as photo-ionization, chemical networks, etc. This is largely because we want to study the dependence of ISM properties on the main drivers of galactic turbulence and it is important to tackle this problem in a bottom-up approach. Implementation of these omitted effects is of course necessary to make the

model more realistic. However, as we see in the further chapters, SN explosions and differential rotation are sufficient prerequisites for a functional galactic dynamo.

2.1 Model Equations

As a computational domain we choose local patch of a typical spiral galaxy (Milky Way like) and express it with a Cartesian coordinate system such that $\hat{x}$, $\hat{y}$ and $\hat{z}$ represent the unit vectors in radial, azimuthal and vertical directions respectively. Dimensions of the box are $-0.4\,\mathrm{kpc}$ to $0.4\,\mathrm{kpc}$ in radial (x) direction, $0\,\mathrm{kpc}$ to $0.8\,\mathrm{kpc}$ in azimuthal (y) direction and $-2.133\,\mathrm{kpc}$ to $-2.133\,\mathrm{kpc}$ in a vertical (z) direction (mid-plane is located at $z = 0\,\mathrm{kpc}$). This domain is resolved in $96 \times 96 \times 512$ grid cells (grid scale is $\sim 8.33\,\mathrm{pc}$).

Within this domain, we solve the set of non-ideal MHD equations using NIRVNA MHD code by Ziegler [2008], which solves these equations in the form of flux conservation laws, using a third order Runge-Kutta formulation along with central Godunov discretization scheme for 3D conservation laws. The following set of MHD equations (Equation 2.1) is solved for four unknowns: density ρ, velocity $\mathbf{u}$, total energy e and magnetic field $\mathbf{B}$, in a co-rotating frame of reference (where all symbols have their usual physical meanings):

$$
\begin{aligned}
\frac{\partial \rho}{\partial t} + \nabla \cdot (\rho \mathbf{u}) &= 0\,, \\
\frac{\partial (\rho \mathbf{u})}{\partial t} + \nabla \cdot (\rho \mathbf{u}\mathbf{u} + \mathrm{p}^{\star} - \mathbf{B}\mathbf{B}) &= -2\rho\ \Omega\ \hat{z} \times \mathbf{u} + 2\rho\ \Omega^2 q x\ \hat{x} \\
&\quad + \rho \mathrm{g}\ \hat{z} + \nabla \cdot \tau\,, \\
\frac{\partial e}{\partial t} + \nabla \cdot ((e + \mathrm{p}^{\star})\,\mathbf{u} - (\mathbf{u} \cdot \mathbf{B})\,\mathbf{B}) &= +2\rho\ \Omega^2 q x\ \hat{x} \cdot \mathbf{u} + \rho \mathrm{g}\ \hat{z} \cdot \mathbf{u} \\
&\quad + \nabla \cdot (\tau \mathbf{u} + \eta \mathbf{B} \times (\nabla \times \mathbf{B})) \\
&\quad + \nabla \cdot \kappa \nabla \mathrm{T} - \rho^2 \Lambda\,(\mathrm{T}) \\
&\quad + \Gamma_{\mathrm{SN}} + \rho\ \Gamma\,(z)\ , \\
\frac{\partial \mathbf{B}}{\partial t} - \nabla \times (\mathbf{u} \times \mathbf{B} - \eta \nabla \times \mathbf{B}) &= 0\,.
\end{aligned}
\tag{2.1}
$$

Here τ denotes the viscous stress tensor

$$
\tau = \tilde{\nu} \left(\nabla \mathbf{u} + (\nabla \mathbf{u})^{\top} - \frac{2\,(\nabla \cdot \mathbf{u})}{3} \right)\,,
$$

with the dynamical viscosity $\tilde{\nu}$. We scale $\tilde{\nu}$ with local mass density and define the constant kinematic viscosity coefficient $\nu = 5 \times 10^{24}\,\mathrm{cm}^2\,\mathrm{s}^{-1}$, leading to the constant magnetic Prandtl number $P_m = \nu/\eta = 2.5$ (for the magnetic diffusivity $\eta = 0.02\,\mathrm{cm}^2\,\mathrm{s}^{-1}$). Theoretical estimate suggests that the typical value P_m in galactic ISM ranges up to 10^{11} [Brandenburg & Subramanian, 2005]. For numerical scheme, however, we are restricted to choose the values closer to unity. The reason for this is the need to resolve both ν and η on the numerical grid (otherwise the value of P_m is intrinsically decided by the numerical scheme; based on the value of numerical diffusivity). With the same token; we also define the isotropic thermal conductivity κ as a function of local mass density such that $\kappa = \kappa_0 \rho/\rho_0$, yielding the values of Prandtl number $P_r = \nu/\kappa\rho c_p \simeq 4$. Where the constant κ_0 is 4×10^8. This scaling also leads to a constant value of Prandtl number $P_r = \nu/\kappa\rho c_p \simeq 4$.

Ω denotes the angular velocity of the box with a shearing parameter q, defined as:

$$q = \frac{d \ln \Omega}{d \ln R}\,, \tag{2.2}$$

which corresponds to the flat rotation curve of a typical spiral galaxy, $\Omega = \Omega_0 R^{-1}$ (R being radial separation) for $q = -1$. As an input parameter, we choose $\Omega_0 = 100\,\mathrm{km\,s^{-1}\,kpc^{-1}}$ as initial condition (equivalent of the angular velocity at radial distance $\sim 2.2\,\mathrm{kpc}$ in the Milky Way). A reason to use such fast rotation velocity (unlike $\Omega_0 = 25\,\mathrm{km\,s^{-1}\,kpc^{-1}}$ consistent with the solar circle) is mainly to get the amplification of magnetic energy, E_m in a reasonable physical time. Gressel et al. [2008] points out that, for a similar model set up, $\Omega_0 > 25\,\mathrm{km\,s^{-1}\,kpc^{-1}}$ is a necessary condition for a galactic dynamo to function. Authors further argue that the exponential growth time of E_m is about $\sim 102\,\mathrm{Myr}$ for $\Omega = 100\,\mathrm{km\,s^{-1}\,kpc^{-1}}$. So to achieve sufficiently strong magnetic fields within a reasonable computational time we resort to relatively fast rotation velocities.

With the used value of Ω ($100\,\mathrm{km\,s^{-1}\,kpc^{-1}}$) we yield the value of Reynold's number $Re \simeq 4000$ and magnetic Reynold's number $Rm \simeq 10000$ in all models.

$\Lambda\,(\mathrm{T})$ is a radiative cooling term, the value of which is prescribed for the particular range of temperature.

Term, Γ_{SN} indicates the rate at which SN energy is injected into ISM. Whereas $\Gamma\,(z)$ represents ambient heating by background stellar population.

Term $\mathrm{g}(z)$ indicates the vertical profile of acceleration due to gravity, contributed mainly by the stellar population in the central disc.

$\mathrm{p}^\star$ is a sum of thermal (p) and magnetic ($\mathbf{B}^2/2\mu_0$) pressure components

$$\mathrm{p}^\star \;=\; \mathrm{p} + \frac{\mathbf{B}^2}{2\mu_0}\,.$$

Thermal pressure p is calculated using thermal energy density ϵ, with the assumption of adiabatic equation of state, $\mathrm{p} = (\gamma - 1)\ \epsilon$, where $\gamma = 5/3$ and thermal energy density ϵ is

$$\epsilon \;=\; e - \frac{\rho \mathrm{u}^2}{2} - \frac{\mathbf{B}^2}{2\mu_0}\,.$$

2.2 Boundary Conditions

Consistent with the differentially rotating disc galaxies, we use so-called 'shearing periodic boundary conditions' in radial direction (x). That is, the values of all variables at inner x boundary are the same as their values at the periodic points on outer x boundaries, except that they are shifted in azimuthal (y) direction to account for the differential shear and corresponding shift derived from the used values of Ω and q. Implementation of shearing periodic boundary conditions is mainly adapted from Gressel & Ziegler [2007]. Also, we use the periodic boundary conditions for azimuthal (y) boundaries. Used condition of periodicity in radial and azimuthal directions ensures the conservation of vertical (z) component of magnetic flux subject to the solenoidal constraint on magnetic field. At the vertical boundaries (z), we use the outflow boundary conditions such that the component of velocity directed outside of domain is chosen by assuming its zero vertical gradient and the component of velocity that is directed inside the box is set to zero. Such outflow boundary conditions prohibit any inflow of the material. Boundary conditions for other fluid variables (mass density, total energy, pressure, radial and azimuthal velocity components, magnetic field components and temperature) are simply set by using zero vertical gradient.

2.3 Physical Effects

To model the realistic ISM turbulence, one needs to incorporate several physical effects that actuate on a variety of length scales. Observational evidences suggest that ISM has turbulent structure with multiple thermal phases including cold dense clouds, warm ionized regime and diffuse hot gas [see e.g. Kulkarni & Heiles, 1988; Spitzer Jr, 1990]. Such complex structure of ISM is maintained mainly via SN energy input (and stellar wind component) which can be visualized thusly. Energy inputs from these sources (SN and stellar wind) heat up and partially ionize the interstellar HI regions (through the secondary processes like low-energy CR and soft X rays, radiations from OB stars, etc.).

These regions further cool down radiatively; while segregating ISM in different phases. All of these physical processes are included using the simple self-consistent models as described in the following sections.

2.3.1 Radiative Cooling

ISM gas cools down via distinctive mechanisms in different ISM phases. For instance, the partially ionized hot HI gas cools down while radiating away the excessive energy through the collisional processes (between the free electrons and hot ISM gas). Whereas cooling of the neutral ISM component is mainly contributed by the excitation of fine structure levels of neutral gas (due to impact of free electrons). Hence the cooling efficiency of a particular ISM gas filament becomes a sensitive function of ISM composition [Dalgarno & McCray, 1972].

To incorporate the aforementioned mechanism we use a simple model of piecewise radiative cooling [e.g. Korpi et al., 1999], in which the cooling efficiency of a particular ISM component is treated as a function of temperature itself and cooling law is expressed as

$$\Lambda(\mathrm{T}) \quad = \quad \Lambda_i \mathrm{T}^{\beta_i} \,, \tag{2.3}$$

where parameters Λ_i represent the cooling efficiency of ISM gas belonging to temperature range $\mathrm{T}_i < \mathrm{T} < \mathrm{T}_{i+1}$. Numerical values of these parameters are listed in Table 2.1. The cooling curve for $\mathrm{T} < 6102\,\mathrm{K}$ has been adopted from Sánchez-Salcedo et al. [2002], while for the temperatures higher than 10^5, Λ_i and β_i are taken from Sarazin & White III [1987]. Figure 2.1 shows the resultant radiative cooling efficiency as a function of temperature, along with the corresponding equilibrium pressure curve for ISM gas (shown in inset).

This implementation includes:

1.) a thermally unstable phase between the range of $141\,\mathrm{K} < \mathrm{T} < 6102\,\mathrm{K}$ in a sense that a gas cloud within this temperature range (due to the inverse dependence of pressure with respect to density), once starts to cool down, continues to cool down until it reaches the next thermally stable temperature range and vice versa.

2) a thermally bistable transition temperature range between $6102\,\mathrm{K} < \mathrm{T} < 2.11\times10^{6}\,\mathrm{K}$, in which the SN explosions mainly take place.

TABLE 2.1: Radiative cooling parameters

T_i K	Λ_i $\mathrm{erg\,s^{-1}\,g^{-2}\,cm^{-3}\,K^{-\beta_i}}$	β_i
10	3.420×10^{16}	2.12
141	9.100×10^{18}	1.00
313	1.110×10^{20}	0.56
6102	1.064×10^{10}	3.21
10^5	1.147×10^{27}	−0.20
2.88×10^5	2.290×10^{42}	−3.00
4.73×10^5	3.800×10^{26}	−0.22
2.11×10^6	1.445×10^{44}	−3.00
3.98×10^6	1.513×10^{22}	0.33
2.00×10^7	8.706×10^{20}	0.50

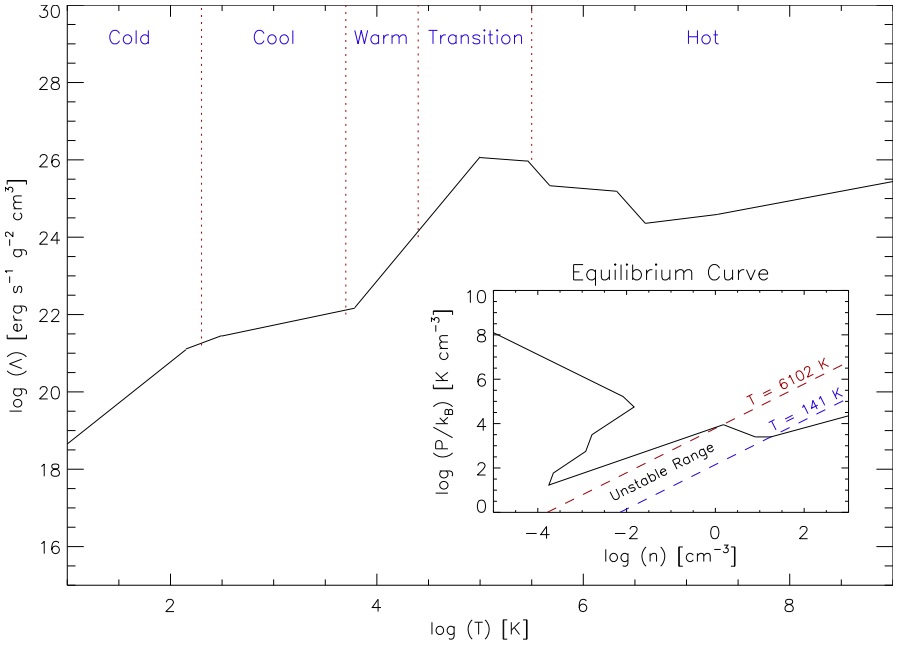

FIGURE 2.1: Radiative cooling efficiency Λ as a function of temperature, along with the nomenclature for different thermal phases described in Chapter 4. Values of relevant parameters are listed in Table 2.1. *Inset*: Equilibrium pressure curve consistent with the used cooling function. A temperature range prone to the thermal instability is bounded by two isothermal lines (blue and red dashed lines).

2.3.2 Diffuse Heating

Diffuse heating of ISM (Γ in Equation 2.1) due to background stellar population (and dust component) contributes significantly to overall ISM energy budget (see Table. 3 and 4 from Abbott [1982]). Primary sources of the diffuse heating are:

1. Heating of HI regions due to background flux of photoelectrons, which originate from the dust grains ionized by the radiations from background OB stars population [Abbott, 1982]. Its contribution to the effective luminosity of the Milky Way disc is about $10^{-25}\,\mathrm{erg\,s^{-1}\,cm^{-3}}$ or $\sim 3\times10^{38}\,\mathrm{erg\,s^{-1}\,kpc^{-2}}$ (for 100 pc height). These estimates are empirically obtained by de Jong [1977]; De Jong [1980] using observational data.

2. Heating of the cold and warm neutral ISM (CNM, WNM) caused by the photoelectrons ejected from FUV irradiated dust grains and PAHs [see e.g. Allamandola et al., 1985; Wolfire et al., 1995]. Contribution of this effect to the Milky Way luminosity is $\sim 10^{-25}\,\mathrm{erg\,s^{-1}\,cm^{-3}}$ as estimated by Draine [1978].

To include the enlisted effects; we use combined, height dependent description for the diffuse heating mechanism given by Joung & Mac Low [2006], as

$$\Gamma(z) \;=\; \Gamma_0 \times \begin{cases} e^{-\frac{z^2}{2z_0 H_\gamma}} & \text{if } |z| < z_0 \\ e^{\frac{z_0}{2H_\gamma}}\left(e^{\frac{z}{H_\gamma}} + 10^{-5}\right) & \text{otherwise} \end{cases} \tag{2.4}$$

for the present model, the characteristic length scales H_γ and z_0 are of 300 pc and 60 pc respectively and the mid-plane heating rate $\Gamma_0 = 0.015\,\mathrm{erg\,s^{-1}}$. These estimates are based upon stellar distribution in the Milky Way. Vertical profile of resultant Γ is shown in Figure 2.2.

2.3.3 Supernova Explosions

In our models, SN explosions are simulated as the spontaneous, localized expulsions of energy, 10^{51} erg/explosion for SN type I and 1.14×10^{51} erg/explosion for SN type II. 14% extra energy attributed to SN type II amounts to the wind contribution of massive stars, the distribution of which is roughly equivalent to the distribution of SN type II [1], [Ferriere, 2001]. SN energy is either injected fully in the form of thermal energy or divided into the CR and thermal energy with a predefined fraction. Numerical implementation of SN explosions is mainly adopted from Gressel [2010].

[1] Although in reality, contribution of the stellar wind component is not as sudden as SN explosions

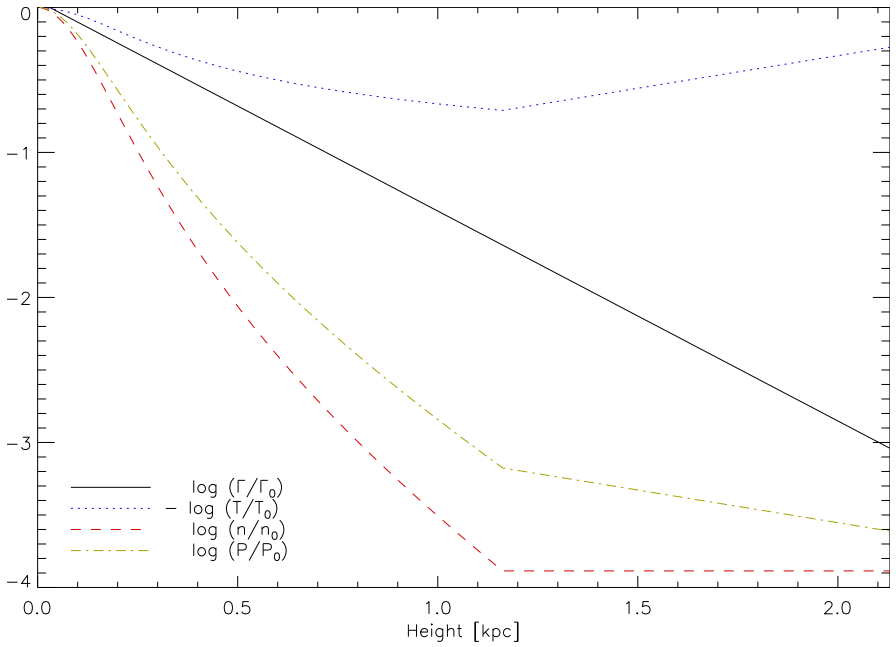

FIGURE 2.2: Vertical profiles of various physical parameters normalized with their mid-plane values. Black-solid line indicates vertical profile of the diffused heating term normalized with $\Gamma_0 = 0.015\,\mathrm{erg\,s^{-1}}$. Blue-dotted line indicates the initial vertical profile of $-1\times$ temperature normalized with $T_0 \simeq 6003\,\mathrm{K}$. Red-dashed line indicates the initial vertical profile of density normalized with $n_0 = 0.6\,\mathrm{cm^{-3}}$ Green-dot-dashed line indicates the initial vertical pressure profile normalized with $P_0 \simeq 8.29 \times 10^{-21}\,\mathrm{Pa}$.

SN energy injections are shaped as a 3D Gaussians of half width $l = 20\,\mathrm{pc}$ in each direction. The shell size l is chosen in such a way that it does not reduce the numerical time step (due to steep gradients) whilst keeping the effect of ghost remnant (due to the periodicity of boundary conditions) as small as possible. SN explosion sites are chosen randomly with an exponential distribution in z direction and a uniform distribution in $x - y$ plane. Scale-heights for the vertical distribution of SN explosions are 325 pc and 90 pc for SN type I and SN type II respectively. It has been reported by Gressel [2010] that a static vertical distribution of SN explosions either sets up the large scale oscillation mode of mid-plane mass density or splits up the central disc if the SN are distributed around the center of mass. By scaling vertical distribution of SN with vertical profile of mass density, however, this problem is tacitly avoided. We furthermore mimic, although very crudely, the spacial clustering effect for SN type II by choosing the probable position of a next SN explosion with a condition that the mass density at that location should be higher than average mass density of the corresponding $x - y$ plane. The subsequent clustering effect allowed by this condition reproduces the observed fraction of clustered and separate SN events [e.g. Ferriere, 2001]. SN explosion rate σ is chosen as the input parameter, which we express in the units of averaged SN rate in the Milky Way. For SN

type I, the reference rate of SN explosions σ_I is $4\,\mathrm{kpc}^{-2}\,\mathrm{Myr}^{-1}$ and for SN type II, σ_{II} is $30\,\mathrm{kpc}^{-2}\,\mathrm{Myr}^{-1}$.

2.3.4 Gravity

We have excluded the effect of self gravity since it is numerically expensive [2]. We instead use the vertical profile of acceleration due to gravity obtained by Kuijken & Gilmore [1989]. Which can be expressed as:

$$\mathrm{g}\,(z) = \frac{-a_1\, z}{\sqrt{z^2 + \mathrm{z_0}^2}} - a_2\, z\,, \tag{2.5}$$

with $a_1 = 1.42 \times 10^{-3}\,\mathrm{kpc\,Myr}^{-2}$, $a_2 = 5.49 \times 10^{-4}\,\mathrm{Myr}^{-2}$ and $z_0 = 180\,\mathrm{pc}$. Values of these parameters correspond to those in the vicinity of the solar circle and are contributed by *i*) the central disc mass, *ii*) a spheroidal ISM bulge and *iii*) the dark matter distribution. In this approach, we tacitly omit the radial component of gravitational attraction, which is a reasonable approximation in the limits of a small vertical extent [see section 7 of Kuijken & Gilmore, 1989].

2.4 Initial Conditions

Initial velocity in our model has only a 'y' component, representing the background shear flow in a co-rotating frame of reference, such that for the shear parameter $q = -1$, $\mathrm{u}_y = \Omega\, x$, (that is $\mathrm{u}_y = \pm 40\,\mathrm{km\,s}^{-1}$ at $x = \pm 0.4\,\mathrm{kpc}$).

Initial value of local magnetic field $\mathbf{B}$ is chosen differently for different models and mentioned in the description of each model.

[2] If the density of cold component becomes sufficiently high to fulfill the Jean's Instability Criteria over the scales of interest, it would not be realistic to exclude the self gravity. However, we later notice that this is not the case.

2.4.1 Density, Pressure, Temperature and Total Energy

Initial vertical profiles of pressure and mass density are calculated by assuming the initial hydrostatic balance between the gravitation pull and vertical pressure gradient. Condition of hydrostatic balance can be expressed as;

$$\frac{\mathrm{d}\rho}{\mathrm{dz}} = \left(\rho \mathrm{g}\left(z\right) - \frac{\partial \mathrm{p}}{\partial z}\right)\left(\frac{\partial \mathrm{p}}{\partial z}\right)^{-1} . \tag{2.6}$$

Equation 2.6 gives an implicit dependency of ρ on $\mathrm{g}\left(z\right)$.

Explicit dependencies $\mathrm{p}(z)$ and $\mathrm{p}(\rho)$ appear from the equation of state and the rate of ambient heating respectively, which can be expressed as

$$\begin{aligned} \frac{\partial \mathrm{p}}{\partial \rho} &= \left(1 - \beta^{-1}\right)\frac{\mathrm{p}}{\rho} . \\ \frac{\partial \mathrm{p}}{\partial z} &= \frac{\mathrm{p}}{\beta \Gamma z}\frac{\mathrm{d}\Gamma \mathrm{z}}{\mathrm{dz}} . \end{aligned} \tag{2.7}$$

By solving Equation 2.6 and Equation 2.7 together, using the second order Runge-Kutta method (subject to the boundary condition that mid-plane mass density $\rho_0 = 1 \times 10^{-24}\,\mathrm{g\,cm^{-3}}$ and mid-plane pressure $\mathrm{p}_0 = 1 \times 10^{-14} Pa$ are chosen as the input parameters), we finally get the vertical profiles of ρ and p as shown in Figure 2.2.

Initial vertical profile of temperature $\mathrm{T_{eq}}\left(z\right)$ is derived from the balance between radiative cooling and ambient heating (that is by solving Equation 2.8 iteratively).

$$\rho \Lambda\left(z\right) \mathrm{T}^{\beta_i} = \Gamma\left(z\right) . \tag{2.8}$$

Initial value of total energy e is then simply calculated from the relation

$$e = \frac{\mathrm{P}}{\gamma - 1} + \frac{\rho \mathbf{u}^2}{2} + \frac{\mathbf{B}^2}{2\mu_0} . \tag{2.9}$$

2.5 Including Cosmic Rays

We use the hydrodynamical treatment for the ensemble of CR particles. Basic implementation of which is mainly adapted from Girichidis et al. [2014]; Hanasz et al. [2009]; Snodin et al. [2006], etc. The physical reasoning behind this assumption is based on the following empirical argumentation.

CRs in ISM are (mostly) relativistic charged particles, which are thought to have accelerated due to the expanding SN remnants [e.g. Bell, 1978; Blandford & Ostriker, 1978]. According to basic electrodynamics, a single charged particle traveling in background magnetic field would 'gyrate' around that field line (subject to the Lorentz force). The 'Gyroradius' for such a particle depends upon the energy of that particle and on the background magnetic field strength, whereas the velocity component parallel to the field line does not get affected at all. Within this scenario, an ensemble of such charged particles can safely be considered as a separate fluid that diffuses along the magnetic field lines. However, this consideration is only valid on the length scales, which are sufficiently larger than the largest Gyroradius within that ensemble.

Now we consider a marginally relativistic CR particle with a component of momentum perpendicular to the field line $p_\perp \simeq 1.5 \times 10^3\,\mathrm{GeV}$. For the values of galactic magnetic field, $\sim 1\,\mu\mathrm{G}$, Gyroradius of this particle becomes $R_\mathrm{g} = |p_\perp/(\mathrm{q\,B})| \approx 0.01\,\mathrm{pc}$ (q, here is an electric charge on CR particle). This R_g is well below our grid resolution ($\sim 8.33\,\mathrm{pc}$) and satisfies the aforementioned condition. Hence CR (energy density) can be adequately modeled with the hydrodynamical 'diffusion-advection' equation [e.g. Snodin et al., 2006] as

$$\frac{\partial e_c}{\partial t} + \nabla \cdot (e_c \mathrm{u} + \mathcal{F}_c) \quad = \quad -\mathrm{p}_c \nabla \cdot \mathrm{u} + \mathcal{Q}_c\,, \tag{2.10}$$

where e_c is the CR energy density. Term p_c represents the CR pressure, which is calculated by assuming an adiabatic equation of state, $\mathrm{p}_c = (\gamma_c - 1)\, e_c$, where $\gamma_c = 14/9$. The system is closed by letting the CR pressure act on flow through the second equation of Equation 2.1 (Navier-Stroke's equation), such that the total pressure term $\mathrm{p}^\star$ should include an additional CR pressure term;

$$\mathrm{p}^{\star} \;=\; \mathrm{p} + \frac{\mathbf{B}^2}{2\mu_0} + \mathrm{p}_c \,.$$

CR energy is injected into the ISM as a predefined fraction of SN energy (on the same length scales as of injections). Term $\mathcal{Q}_c$ in Equation 2.10 represents the rate at which the CR energy is injected.

Term $\nabla \cdot \mathcal{F}_c$ in Equation 2.10 represents an anisotropic diffusion of CR energy density (different rate of diffusion along and perpendicular to magnetic field). The usual approach to ensure the field aligned nature of diffusion is to represent the cosmic ray diffusion flux as

$$\mathcal{F}_c \;=\; -K_{ij}\nabla_j e_c \,, \tag{2.11}$$

with anisotropic diffusion tensor defined as

$$K_{ij} = K_{\perp}\delta_{ij} + \left(K_{\parallel} - K_{\perp}\right)\hat{\mathrm{B}}_i\hat{\mathrm{B}}_j \tag{2.12}$$

where $\hat{\mathrm{B}}_i$ and $\hat{\mathrm{B}}_j$ are the i'th and j'th components of unit vector in the direction of local magnetic field, $\hat{\mathbf{B}} = \mathbf{B}/\left|\mathbf{B}\right|$. While $K_{\parallel}$ and $K_{\perp}$ are the cosmic ray diffusion coefficients (chosen as the input parameters), parallel and perpendicular to the magnetic field respectively. Castellina & Donato [2013] give a theoretical estimate for $K_{\parallel}$, which is approximately $10^{28}\,\mathrm{cm}^2\,\mathrm{s}^{-1}$ and the ratio $K_{\parallel}/K_{perp} \approx 100$. For our simulations, however, these values of diffusion coefficients put a serious restriction on the time step and we are forced to use the smaller values $K_{\parallel} = 3 \times 10^{27}\,\mathrm{cm}^2\,\mathrm{s}^{-1}$ and $K_{\parallel}/K_{\perp} = 100$. We also use the non-Fickian scheme to evolve the CR diffusion flux, unlike Equation 2.11 (reasons described in Appendix A). A common way to incorporate this description is to express the evolution of diffusive flux via the 'Telegraph equation' [Snodin et al., 2006], which represents a non-fickian treatment for CR diffusion flux as

$$\frac{\partial \mathcal{F}_{ci}}{\partial t} \;=\; \frac{1}{\mathcal{T}}\left(-K_{ij}\nabla_j e_c - \mathcal{F}_{ci}\right) \,, \tag{2.13}$$

where $\mathcal{F}_{ci}$ is the i'th component of CR diffusion flux and $\mathcal{T}$ is the finite correlation time which limits the propagation speed of diffusing CR blobs within finite values. This non-Fickian diffusion equation leads to an oscillating solution, as the value of 'Strouhal number' St $= \sqrt{K_{\parallel}\mathcal{T}}/h$ approaches 1. With the typical length scales $h \sim 1\,\mathrm{kpc}$, we get a Strouhal number of the order of 10^{-2}, which is well within the Fickian limit on a large scale and corresponding solution matches significantly with the solution of diffusion equation (Appendix B). For numerical reasons we still include an isotropic Fickian diffusion term with the diffusion coefficient of $0.1K_{\perp}$.

$$\mathcal{F}_{fick} = -K_{fick}\nabla e_c \tag{2.14}$$

For CR models, Equation 2.10 and Equation 2.13 are solved along with Equation 2.1, while using the modified value of total pressure (Equation 2.11).

Chapter 3

Global Evolution of ISM

In this chapter, the results of direct numerical simulations (DNS) without CR component are compiled and SN explosions here are simulated such that they expel only thermal energy into ISM. These models are therefore referred, as 'thermal SN models' hereafter (as opposed to 'CR models' discussed in Chapter 6, in which SN explosions expel either only CR energy or CR + thermal energy).

3.1 Overview of Studied Models

Based on different seed field configurations, the following three types of models have been simulated:

1. Initial field with only a vertical (z) component of strength $0.001\,\mu$G, either with or without the net vertical flux.
2. Strong initial field ($0.1\,\mu$G) with only a vertical component and with either zero or nonzero net vertical flux.
3. Weak initial field with radial and azimuthal components of strength $0.001\,\mu$G (and without flux).

In the models with net vertical flux (type 1 and 2) the initial magnetic field has only a constant vertical (z) component passing through the central disc, while for the models without flux the initial vertical component of magnetic field is a sinusoidal function of

x coordinate. In the models of type 3, in contrast, initial magnetic field has only x and y components (with the strengths of 0.5 nG and 1 nG, respectively) with their vertical profiles leading to a constant value of plasma $\beta \sim 10^7$ throughout the domain.

For the first type of models with net vertical flux (and initial field strength of nG) we further vary the rate of SN explosions while keeping the other parameters constant. Although in reality, the SN explosion rate is probably linked with ISM mass density in the vicinity of the explosion site. So, by artificially keeping the other parameters unchanged, we should be able to analyze the evolution of ISM as a function of turbulence driving mechanism (SN explosions).

A motive behind using the different seed field configurations is primarily to see whether the traces of the initial field configuration are eventually erased in the evolution and whether the magnetic field evolution after all depends upon its initial configuration. Another reason to use the strong vertical flux for the initial field is to invoke the possibility of the existence of Magnetorotational instability (MRI), [e.g. Balbus & Hawley, 1991; Hawley et al., 1995], which supposedly is one of the main sources of ISM turbulence in the outer parts of galaxies, but might be suppressed in the inner disc, where SN induced turbulence is prevalent [e.g. Dziourkevitch et al., 2004; Sellwood & Balbus, 1999]. Resolution we use here coincides with the length scale of fastest growing MRI mode. MRI turbulence is therefore expected to influence the dynamo action in the outer halo of the low SN rate models and recover the observed large scale-heights of regular fields. Nomenclature and corresponding input parameters of the aforementioned models are listed in Table 3.1.

3.2 General Evolution of Thermal SN Models

Starting from initial condition with the temperature ranging between 5000 K and $10^{5.5}$ K (initial distribution of temperature is uniform over the xy plane and its vertical profile is shown in Figure 2.2), ISM in all models quickly splits into a steady multiphase structure within first $\sim$ 50 Myr of evolution (Chapter 4) and achieves a quasi-stationary state characterized by:

1. A steady state of total thermal energy E_{th} scaling roughly with respect to the SN rate as $E_{th} \sim \sigma^{0.5\pm0.05}$

TABLE 3.1: Nomenclature for all thermal SN models with vertical B_z and horizontal (in $x-y$ plane) B_h seed field components. SN rates (σ) are expressed in the units of $\sigma_0 = \left({\sigma_I}^{-1} + {\sigma_{II}}^{-1}\right)^{-1}$. Time t_K indicates the time up to which the kinematic growth phase lasts. The total runtime for simulations is given in the last column.

Name	SN rate σ_0	B_h μG	B_z μG	f_z $\mu\mathrm{G\,kpc}^2$	t_K Gyr	Time Gyr
F	1.00	0.0	0.001	0.00064	0.9	1.5
H	0.50	0.0	0.001	0.00064	1.0	1.8
Q	0.25	0.0	0.001	0.00064	1.2	1.5
QZ	0.25	0.0	0.001	0.0	2.1	2.5
AR	0.25	0.001	0.0	0.0	1.5	1.9
QS	0.25	0.0	0.1	0.064	0.9	1.6
QSZ	0.25	0.0	0.1	0.0	1.1	1.2

2. A steady state of turbulent kinetic energy E_k, which approximately depends upon the SN rate as $\sim \sigma^{0.8\pm0.03}$ (Table 3.4).

3. A stationary vertical profile of mean mass density (average defined on the $x-y$ plane).

Quantitative aspects the stationary state are described in the following subsections.

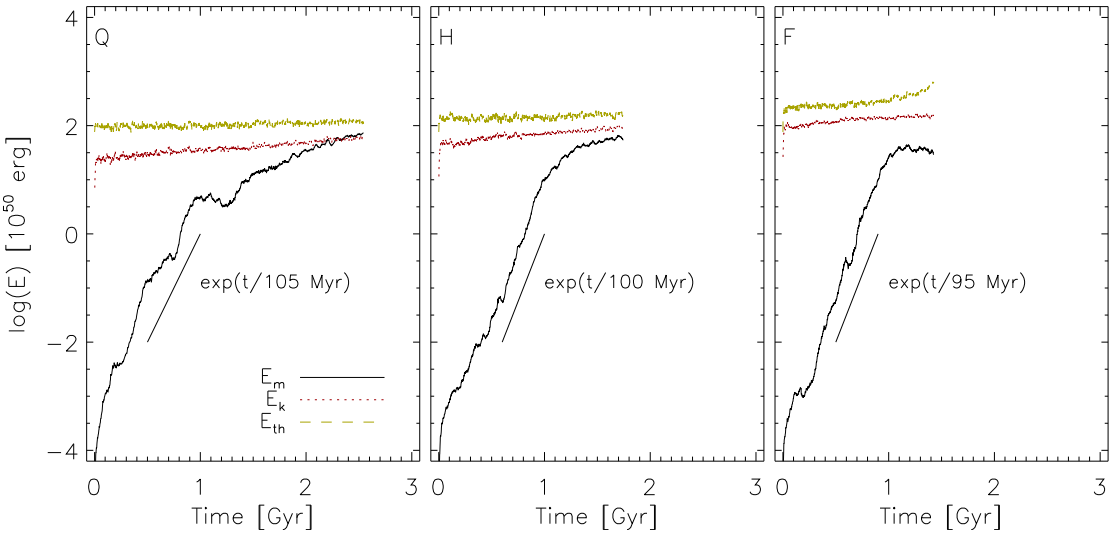

FIGURE 3.1: Evolution of thermal energy E_{th} (green-dashed line), kinetic energy E_k (red-dotted line) and magnetic energy E_m (black-solid line) for models Q, H and F (from left to right).

3.2.1 Kinematic and Dynamical Phase

After the fast exponential growth for initial 50 Myr, total magnetic energy in all models grows exponentially with roughly the same folding time of ~ 100 Myr, irrespective of SN rate. For the models with higher initial seed field strength (QS and QSZ), on the other hand, this exponential growth time is about 200 Myr (for reasons which will become clear in Chapter 5). This amplification takes place for almost a Gyr until it slows down for model Q and H, while it saturates for model F. Physical time at which this transition occurs is different for different SN rates, for instance in models Q and H this growth slows down after ~ 1.2 and ~ 1.0 Gyr respectively, whereas for model F such transition occurs just after ~ 0.9 Gyr. Amplification and saturation of E_m is clearly seen in Figure 3.1 for model Q, H and F, and Figure 3.2 represents the same for the remaining models. Total magnetic energies corresponding to this transition scale directly with SN rate (roughly as $\sigma^{0.6}$), as shown in Table 3.4. Hereafter we refer to the initial exponential growth phase of magnetic energy ($\sim$ 1 Gyr) as the kinematic phase, as opposed to the dynamical phase afterwards. It should be noted that although E_m reaches to equipartition later in the dynamical phase of model Q, the ratio of total magnetic to total turbulent kinetic energy (E_m/E_k) at the beginning of dynamical phase is less than unity for all SN rates (0.25, 0.14 and 0.10 for models Q, H and F respectively). It is also interesting to note that the growth rate of E_m during the dynamical phase is an inverse function of SN rate (it is zero in model F) [1]. Such distinctive behavior of E_m in the dynamical phases of different SN rate models is explained in the context of $\alpha\Omega$ dynamo in Chapter 5. Though the overall turbulence structure for all models remains approximately similar throughout the evolution, the multiphase distribution of ISM is significantly affected during the dynamical phase, mainly because of the additional magnetic pressure, which does not distribute uniformly amongst all ISM phases (see Chapter 4). Evolution of these various parameters during the kinematic and dynamical phases is discussed in the following subsections.

[1] for models QS, QSZ, QZ and AR, the ratio E_m/E_k at the end of the kinematic phase is just same as that of model Q, so are the values of E_k and E_{th}.

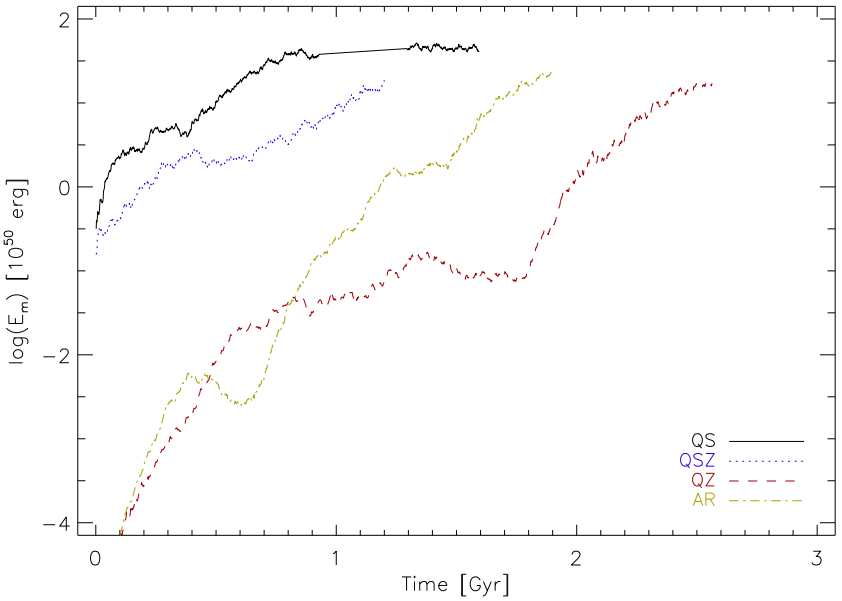

FIGURE 3.2: Time evolution of total magnetic energy for models QS (black-solid line), QSZ (blue-dotted line), QZ (red-dashed line), AR (green-dot-dashed line). Thermal and turbulent kinetic energies are same as those for model Q.

3.2.2 Mean Density

The initial Gaussian vertical profile (with a full width half maximum of 325 pc) of mean density evolves, due to the turbulent kinetic pressure component caused by the SN explosions, to an almost steady vertical profile within the first 50 Myr. This profile is comprised of three visually distinct parts, namely a thin central disc (inside $|z| < 0.2$ kpc), an intermediate thick disc (inside $|z| < 0.8$ kpc) and upper halo part ($|z| > 0.8$ kpc) for all SN rates. The resulting profiles are therefore best fitted with a superposition of three exponential functions such that

$$\rho(z) \simeq \sum_{i=0}^{2} \rho_i \exp\left(\frac{-|z|}{r_i}\right) . \tag{3.1}$$

Where the parameters r_i's correspond roughly with the scale-heights of aforementioned three distinct parts, values of the fitting parameters (ρ_i and r_i) depend slightly on the SN rate, as represented in Table 3.2. These values remain approximately constant throughout the evolution, however, density of the central disc part (ρ_0) decays slightly during the dynamical phase and the corresponding scale-heights r_0 remain constant. As far as the SN rate dependence is concerned, it is evident from Table 3.2 that the scale-heights r_0 stay nearly independent of the SN rate, but the average mid-plane density ρ_0 decreases slightly. In contrast, scale-heights for an intermediate disc and

outer halo (r_1 and r_2) become broader with respect to SN rate, roughly proportional to $\sigma^{0.4}$, concordantly with increased kinetic pressure with respect to the SN rate.

TABLE 3.2: Amplitudes and scale-heights of the $\rho(z)$ profiles (ρ_i and r_i) for all SN rates with there corresponding error bars.

Model	ρ_0 $[\,\mathrm{cm}^{-3}]$	r_0 [kpc]	ρ_1 $[\,\mathrm{cm}^{-3}]$	r_1 [kpc]	ρ_2 $[\,\mathrm{cm}^{-3}]$	r_2 [kpc]
Q	0.6 ± 0.1	0.11 ± 0.04	0.1 ± 0.03	0.25 ± 0.04	0.01 ± 0.002	0.7 ± 0.3
H	0.5 ± 0.1	0.12 ± 0.05	0.1 ± 0.05	0.35 ± 0.08	0.01 ± 0.003	0.9 ± 0.3
F	0.3 ± 0.1	0.12 ± 0.05	0.1 ± 0.05	0.42 ± 0.1	0.01 ± 0.005	1.2 ± 0.5

Note: Fitting parameters for models QS, QSZ, QZ and AR are nearly the same as those of model Q.

3.2.3 Mean and Turbulent Magnetic Fields

The local magnetic field $\mathbf{B}$ can be split as a sum of its mean, $\overline{\mathbf{B}}(z)$ and fluctuating turbulent components $\mathbf{b}'$. Where the mean magnetic field profile is simply defined as

$$\overline{\mathbf{B}}(z) = \frac{1}{L_x L_y} \int \mathbf{B}\, \mathrm{d}x\, \mathrm{d}y\,, \tag{3.2}$$

L_x and L_y are the x and y dimensions of the computational domain (0.8 kpc) (expression for the total magnetic field thus becomes $\mathbf{B} = \overline{\mathbf{B}}(z) + \mathbf{b}'$). Subject to the solenoidal constraint along with periodic (and shearing periodic) boundary condition on y and (x) boundaries, z component of mean field remains unchanged throughout the evolution. The radial $\overline{B}_x(z)$ and azimuthal $\overline{B}_y(z)$ mean field components evolve exponentially such that the absolute values of $\overline{B}_x(z)$ stay about 4-5 times smaller than $\overline{B}_y(z)$, but with the opposite signs during the late phases of evolution (largest values of pitch angles are about 10^o to 18^o). Hence, to avoid the redundancy, we only describe the evolution of azimuthal $\overline{B}_y$ component hereafter. Mean and turbulent magnetic fields (starting from the seed field strengths of 1 nG) also evolve exponentially with a growth time of 200 Myr for almost a Gyr and with slow growth rates afterwards (it saturates for model F), as shown in Figure 3.3. Vertical profiles of mean fields in models Q, H and F go through multiple sign and parity changes as they evolve. Eventually a symmetric configuration (S mode) arises in all models except model QS, where the initially strong antisymmetric

seed field is preserved. For instance, Figure 3.4 and Figure 3.5 show the vertical profiles of mean field at different times. It is to be noted that the temporal fluctuations in the evolution curve of E_m (Figure 3.1) are associated with the parity changes (A mode to S mode or vice versa) in the corresponding mean field profiles. Consistent with this note, a slowly growing intermediate phase in the E_m evolution curve for model QZ (red-dotted line in Figure 3.2, between 0.5 to 2 Gyr), simply linked to the slowly growing, temporarily sustained A mode of $\overline{B}_y(z)$.

The final S mode achieved in model F is a stationary one, unlike models Q and H, where the absolute magnitudes of $\overline{B}_y(z)$ profiles keep increasing with a small growth rate, even in the dynamical phases. At the beginning of the dynamical phase, values of $\overline{B}_y(z=0)$ are 1.5, 1.2 and 0.9 μG for models Q, H and F respectively. However, until the end of evolution, these mid-plane values still grow up to ~ 3 and 2 μG for models Q and H. The best fit for the final symmetric profile of $\overline{B}_y(z)$ is expressed by the superposition of two exponential functions as

$$\overline{\mathbf{B}}_y(z) \simeq \sum_{i=0}^{1} B_i \exp\left(\frac{-|\,z\,|}{h_i}\right), \tag{3.3}$$

with two distinctive scale-heights, h_0 and h_1. Values of the fitting parameters B_i and h_i for models Q, H and F are documented in Table 3.3, from which we see a general increase of h_i with respect to SN rate as $h_0 \sim \sigma^{0.4}$ and $h_1 \sim \sigma^{0.8}$. Even for the models with a strong initial field (i.e. QS and QSZ) halo scale-heights h_1 are same as those of model Q (and also QZ and AR), indicating the absence of MRI modes in outer halo parts. Recent radio observations of nearby edge-on spiral galaxies [Krause, 2011] also reveal a double exponential scaling for magnetic fields with distinctive inner disc plus extended outer radio halo. Typical scale-heights (of the regular fields) in the inner discs of their observed sample galaxies are roughly consistent with our simulations (h_0), however, for the outer halo part we only get half of the observed scale-heights h_1. By using the larger vertical extent for our simulation box, we might be able to recover the observed large scale fields in the halo.

Similar to $\overline{\mathbf{B}}$, the turbulent component $\mathbf{b}'$ also has the exponential growth time of $\sim$ 200 Myr during the initial kinematic phase (that slows down later during the dynamical

TABLE 3.3: Fitting coefficients (B_i and h_i) for the RMS magnetic field $B(z)$. Alfvén velocities at $z = 0$ listed in the last column.

	B_0 [μG]	h_0 [kpc]	B_1 [μG]	h_1 [kpc]	$v'_{\rm A}(z=0)$ [km s^{-1}]
Q	2.8	0.48 ± 0.08	0.32	1.5 ± 0.2	10 ± 0.5
H	2.6	0.58 ± 0.11	0.44	2.7 ± 0.3	14 ± 0.5
F	2.3	0.85 ± 0.10	0.40	4.0 ± 0.4	18 ± 0.5

Notes: Scale-heights for the RMS ($B(z)$) and mean field profiles ($\overline{\mathbf{B}}$) are roughly the same, consistent with a constant ratio of mean to turbulent field component throughout the domain. Alfvén velocities in the mid-plane scale roughly with respect SN rate as $v'_{\rm A} \sim \sigma^{0.4}$.

phase), as shown in Figure 3.3 [red-dotted line]. Final vertical profiles of $\mathbf{b}'$ also fit best with Equation 3.3 and have the same scale-heights as those of the mean field $\overline{\mathbf{B}}$.

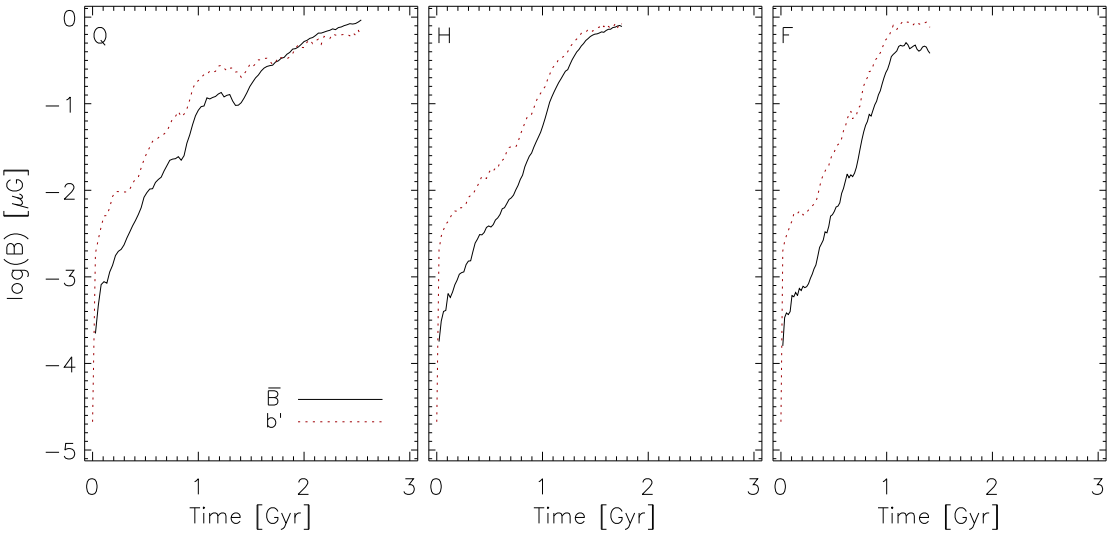

FIGURE 3.3: Evolution of mean magnetic field $\left|\overline{\mathbf{B}}\right|$ (black-solid line) and turbulent magnetic field $|b'|$ for models Q, H and F (from left to right).

The fact, that the scale-heights of $\mathbf{b}'(z)$ and $\overline{\mathbf{B}}_y$ do not differ, suggests that turbulent field component is most probably generated via a mechanism of field-line tangling. In this mechanism, large scale mean field lines ($\overline{\mathbf{B}}$) are tangled up due to background turbulence $\mathbf{u}'$ [2]. In a more systematic way, turbulent field generation can be expressed as $\mathrm{b}' = \overline{B} u' l_c / \eta_c$, where η_c is the diffusion coefficient corresponding to the Ohmic dissipation and l_c is the resistive length scale.

Scale dependent correlation between the radio synchrotron and far infrared emission observed in the spiral galaxies is usually different in the arm and inter-arm regions.

[2] In the most simple scenario, a field line tangling term can be expressed as $\nabla \times (\mathbf{u}' \times \overline{\mathbf{B}})$, unlike a small scale turbulent dynamo term $\nabla \times (\mathbf{u}' \times \mathbf{b}')$.

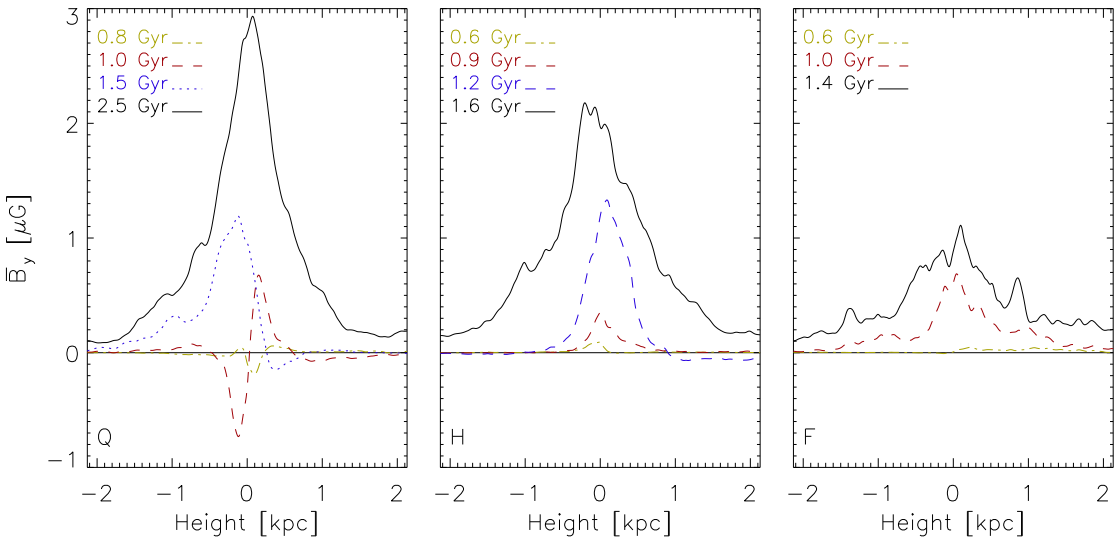

FIGURE 3.4: Evolution of $\overline{B}_y(z)$ profiles for model Q, H and F (from left to right). Intermediate phase reversals and parity changes are clearly visible along with the final S modes. Mid-plane field strengths seem to scale as an inverse function of SN rate.

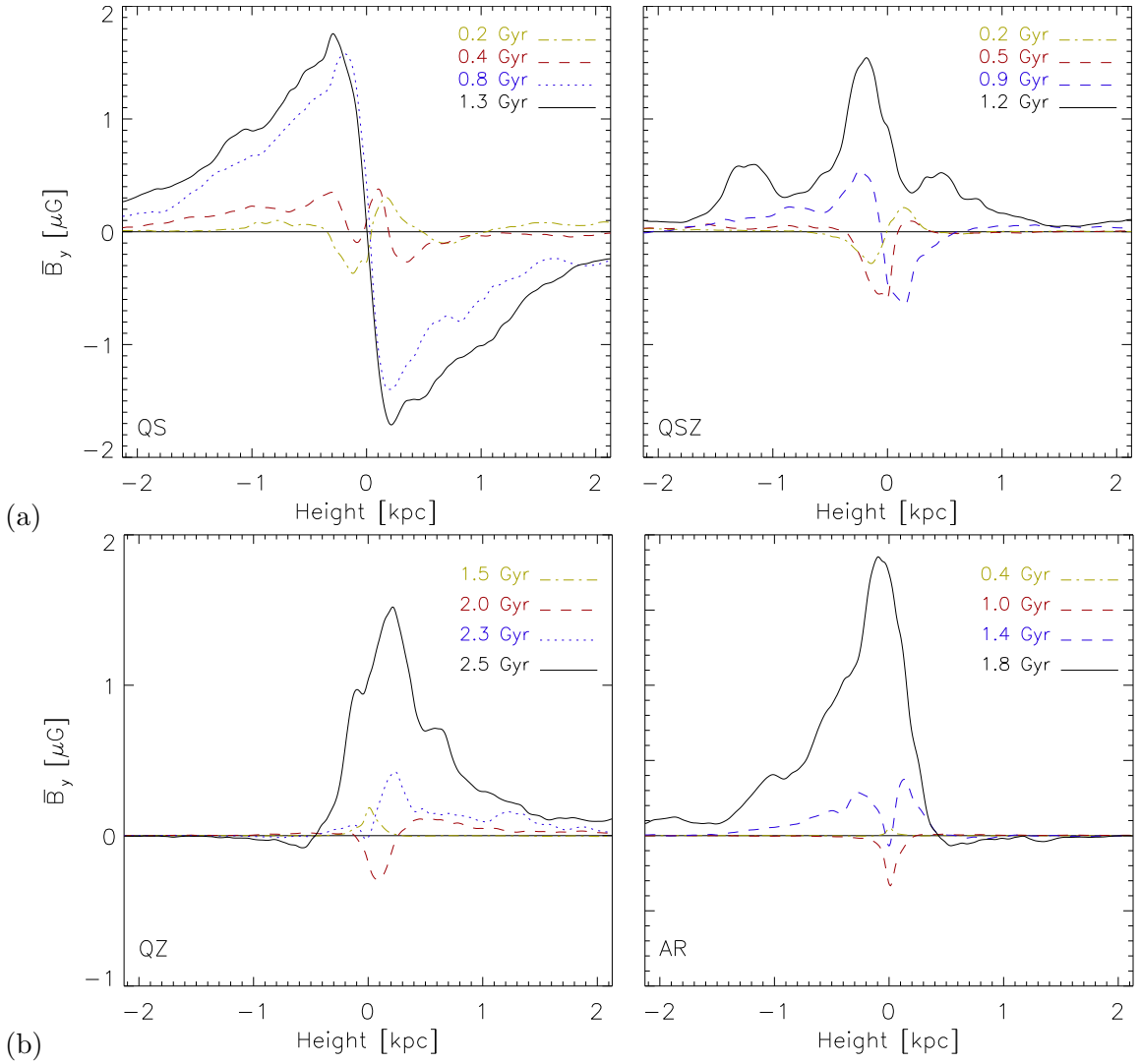

FIGURE 3.5: Same as Figure 3.4, but for models QS, QSZ, QZ, AR.

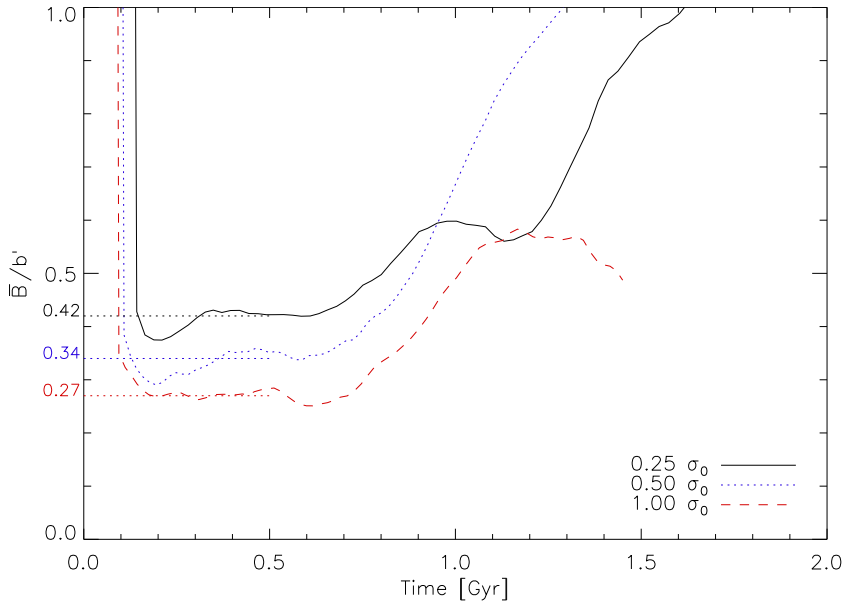

FIGURE 3.6: Evolution of the relative strengths of mean to turbulent magnetic fields $\left|\overline{\mathbf{B}}\right| / |\mathbf{b}'|$, for model Q (black-solid line), H (blue-dotted line) and F (red-dashed line). A constant value of $\left|\overline{\mathbf{B}}\right| / |\mathbf{b}'|$ during the kinematic phase scales with a SN rate as $\sigma^{-0.3}$ (similar to the observations by Chyży [2008]).

This can be interpreted as the correlation between the strength of turbulent field and SN rate [e.g. Beck & Wielebinski, 2013]. Relative strength of the regular and turbulent fields can be expressed in terms of a ratio $\left|\overline{\mathbf{B}}\right| / |\mathbf{b}'|$. For all simulated models, this ratio decreases for initial $\sim 100\,\mathrm{Myr}$, $\left|\overline{\mathbf{B}}\right| / |\mathbf{b}'|$ and remains approximately unchanged throughout the kinematic growth phase. Further in the dynamical phase, it increases linearly, as shown in Figure 3.6. Inverse dependence of this ratio with respect to SN rate is roughly consistent with observed strong ordered fields in the inter-arm regions with low SN rates [e.g. in NGC6946 Tabatabaei et al., 2013]. During the kinematic phase the ratio scales with the SN rate roughly as

$$\frac{\left|\overline{\mathbf{B}}\right|}{|\mathbf{b}'|} = 0.27\sigma^{-0.3\pm0.07}, \tag{3.4}$$

which matches with observations by Chyży [2008].

3.2.4 Field-Density Distribution

The importance of magnetic field in the dynamics of ISM can be inferred from the correlation of total field $\mathbf{B}$ with gas density ρ. A power law correlation $|B| \propto \rho^a$ naturally

arises from the conservation of mass and magnetic flux inside the ISM blob and the exponent a depends upon the mechanism of field amplification and also on the geometry of underlying regular field. For example, $a = 1/2$ implies the isothermal compressional amplification of the field with an equipartition between kinetic and magnetic energies. Equivalently $a = 2/3$ represents the field amplification due to the isotropic compression of ISM gas. Also B remaining independent of ρ is symptomatic of the ISM compression along the field lines (see Tritsis et al. [2015] for details). Interestingly, the observed density dependent nature of exponent a in dense ISM clouds [e.g. Crutcher et al., 2010] implies the influence of magnetic field on the star formation via ambipolar diffusion of magnetic flux out of the ISM clouds, which, however, is beyond the scope of this work. Although, in order to be able to distinguish the amplification mechanism on various scales, it may be worthwhile to study such correlations in the numerical models presented in this subsection.

A scatter plot of the total field versus density is shown in Figure 3.7 (for model Q). The varying behavior between the inner disk ($|z| < 0.5\,\mathrm{kpc}$) and outer halo ($|z| > 0.5\,\mathrm{kpc}$) suggests the presence of different amplification mechanisms. To put this argument in a quantitative manner, we first consider a $B - \rho$ distribution in the inner disc part of model Q, during the initial kinematic phase (Figure 3.7 *Panel lower-left*). The exponent 'a' for this region is approximately 0.5 (with a slight dependence on SN rate), indicating the dominant compressional amplification in approximately isothermal manner. This distribution further splits into two, as the dynamical phase approaches such that, for the (relatively) dense ISM (with $n > 0.01\,\mathrm{cm}^{-3}$), value of a reduces to 0.3 (flattened), and for the lighter ISM, a approaches to ~ 1 (steepened). Flattening of the distribution (within the dense disc) can be explained as follows: During the dynamical phase, strong mean field component backreacts on the turbulence (and thereby reduces the values of dynamo coefficients) and the field amplification takes place *predominantly* due to the passive winding of the field lines in the shearing flow, as opposed to the dominant isothermal compressional mechanism during initial kinematic phase. This distinction straightforwardly leads to the flattening $B - \rho$ distribution, indicating an approximate independence of B and ρ, as is seen in Figure 3.7 *[Panel upper-left]*. Flattening can also be reasoned on the basis of the increasing contribution of the regular component to local magnetic field that remains nearly independent of ρ. This flattening, however, as compared to model Q, is not so significant in the inner disc of model F ($a \sim 0.45$ for

model F and ~ 0.3 for Q, see Figure 3.9). A possible reason for the SN rate dependence probably lies in the different saturation processes, which are elaborated in Chapter 5 in the context of dynamo quenching.

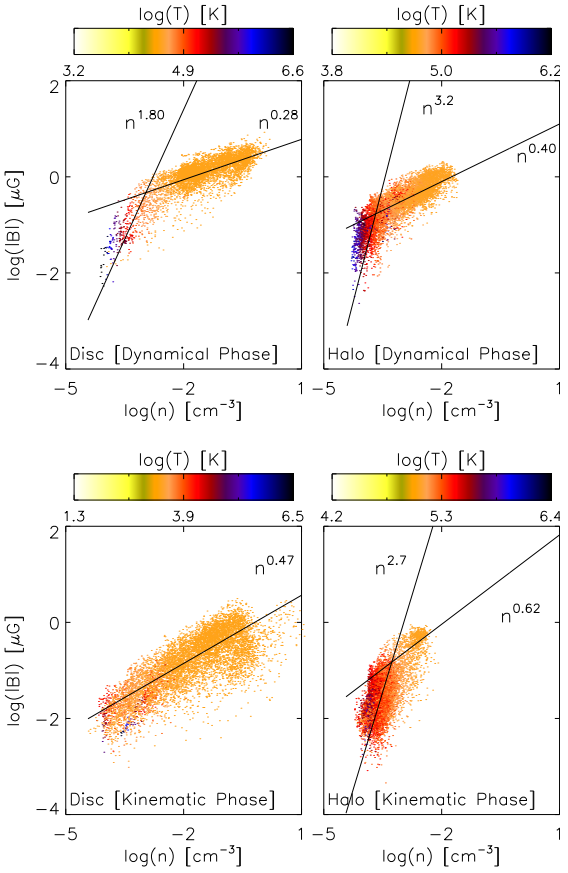

FIGURE 3.7: Distribution of total magnetic field $|B|$ with respect to density ρ during the kinematic as well as in the dynamical phase for model Q.

Now we consider the lighter ISM part ($n < 0.01\,\mathrm{cm}^{-3}$) of the inner disc ($|z| < 0.5\,\mathrm{kpc}$), which comprises of a comparatively steeper tail of $B - \rho$ distribution during the dynamical phase. The exponent of distribution , a for this region, is 1 for model Q. This signifies the transverse compressional amplification of the field, which is frozen longitudinally inside the elongated ISM blobs [e.g. sections 2.1.1 and 2.1.3 of Tritsis et al., 2015]. There is no significant impact of the SN rate on the $B - \rho$ distribution in this region (see; Figure 3.7, Figure 3.8 and Figure 3.8).

The upper halo part ($|z| > 0.5\,\mathrm{kpc}$), possesses a comparatively steeper $B - \rho$ distribution during the kinematic phase, for which the exponent a ranges between $\sim$ 0.8 to 0.6 (changes with respect to SN rate). This is generally indicative of a special case $a = 2/3$, which implies the amplification of B due to the spherical isotropic collapse of ISM clouds,

whereas the departure from isotropic collapse changes the value of a, such that $a < 2/3$ indicates the faster contraction along the field lines as compared to the transverse and vice versa. These distributions also get flatter ($a \sim 0.5$) during the dynamical phase, probably for the same reasons described for the inner disc part.

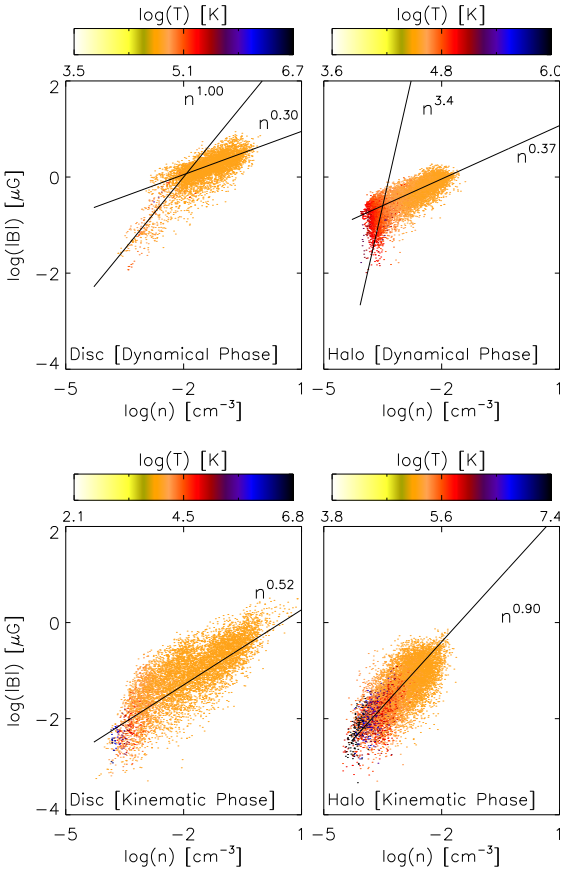

FIGURE 3.8: Same as Figure 3.7, but for model H.

3.2.5 Alfvén Velocities

To characterize the dynamical relevance of magnetic field in the different phases of ISM, it is helpful to compare the Alfvén and the corresponding turbulent velocities. For that we first describe the evolution of root mean squared (RMS) magnetic field profiles, which can be defined as

$$B(z) = \frac{1}{L_x L_y} \left(\int (\mathbf{B} \cdot \mathbf{B}) \, \mathrm{d}x \, \mathrm{d}y \right)^{1/2} . \tag{3.5}$$

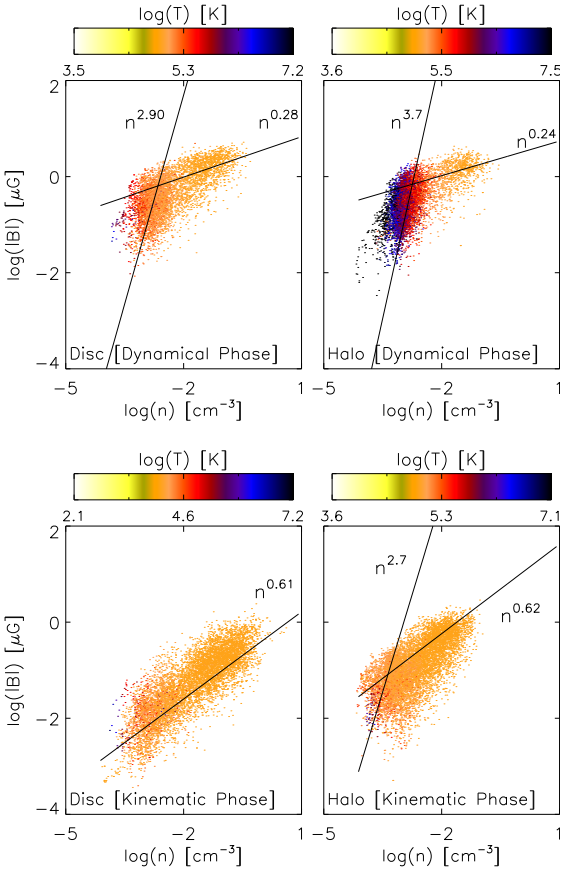

FIGURE 3.9: Same as Figure 3.7, but for model F.

During the dynamical phase, $B(z)$ profiles also evolve to a S mode, having a best fit defined by Equation 3.3, and the fitting parameters B_i and h_i have similar values as $\overline{\mathrm{B}}_y(z)$ (consistent with a roughly constant ratio of mean over turbulent field strength throughout the domain). These profiles get wider with increasing SN rate and mid-plane RMS field strengths go as large as 2 to 3 μG for all models.

Using the vertical profile of B, mean value of Alfveń velocity can be estimated as follows

$$v'_{\mathrm{A}}(z) = \frac{B(z)}{\sqrt{\rho(z)}}\,. \tag{3.6}$$

During the dynamical phase, $v'_A(z)$ profiles attain an inverted bell shape for all SN rates, with its mid-plane values roughly scaling with respect to SN rate as $v'_A \sim \sigma^{0.4}$, while in the outer halo part, v'_A remains nearly a constant for all SN rates (e.g. Table 3.3).

Formal definition of the Alfveń velocity, on the other hand, takes the local statistical correlations into account, such that

$$v_{\rm A}(z) = \frac{1}{L_x L_y} \int \frac{|\mathbf{B}|}{\sqrt{\mu_0 \rho}}\, {\rm d}x\, {\rm d}y\,, \tag{3.7}$$

which is an integral of local Alfveń speed over the $x-y$ plane. Similar to $v'_A(z)$, $v_{\rm A}(z)$ profiles also evolve to an inverted bell shaped function with their mid-plane values scaling roughly with respect to SN rate as $\sigma^{0.4}$ and remain approximately constant above $z = 1\,{\rm kpc}$ (indicating the reduced mid-plane density, Table 3.2). At the end of kinematic phase, amplitudes of $v_{\rm A}$ in the halo region become as high as $28 \pm 5\,{\rm km\,s^{-1}}$.

The straightforward relation between $v_{\rm A}$ and $v'_{\rm A}$ can therefore be simply expressed as

$$v'^2_{\rm A} = v^2_{\rm A} + \frac{\overline{\tilde{v}^2_{\rm A}\tilde{\rho}}}{\overline{\rho}}\,, \tag{3.8}$$

where an over-bar represents the average over $x-y$ plane and a 'tilde' represents the fluctuations of a corresponding quantity from its mean value. The term $\overline{\tilde{v}^2_{\rm A}\tilde{\rho}}/\overline{\rho}$ represents a first order statistical correlation between the local Alfvén velocities, $v_{\rm A}$ and mass density ρ.

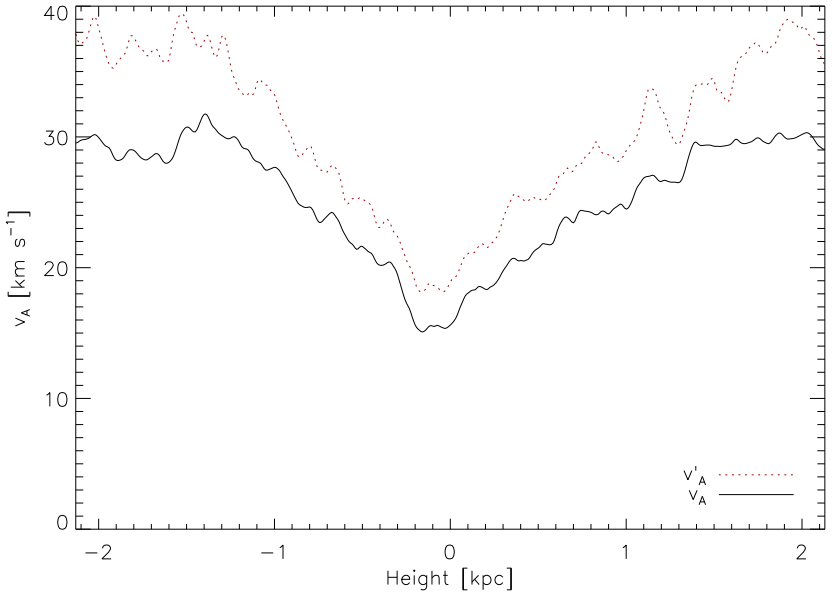

FIGURE 3.10: Typical Alfvén velocity profiles for models Q, H and F (shown for model H), $v_A(z)$ (black-solid lines) and v'_A (red-dotted lines), both during the dynamical phase.

During the initial kinematic phase, $v_{\rm A}(z)$ and $v'_{\rm A}(z)$ differ by approximately 25% in the outer halo part ($|z| > 1\,{\rm kpc}$), with $v_{\rm A} < v'_{\rm A}$, but have, approximately same magnitudes in the inner disc. Later during the dynamical phase, $v_{\rm A}(z)$ and $v'_{\rm A}(z)$ match with a good

accuracy in the inner disc (difference is $< 3\%$), while in the outer halo, this difference is as large as $\sim 15\%$ (with $v_{\rm A} < v'_{\rm A}$). This comparison is well represented in Figure 3.10. Considering this scenario in combination with Equation 3.8, we further argue that during the dynamical phase, statistical correlation between the local Alfvén velocity and a mass density vanishes in the inner disc, although a negligible correlation exists in the outer parts of the box.

3.2.6 Velocities

Similar to the local magnetic fields, the velocity field $\mathbf{u}$ can also be split as a sum of the mean ($\overline{\mathbf{u}}(z)$) and a fluctuating part ($\mathbf{u}'$). The mean velocity is defined as

$$\overline{\mathbf{u}}(z) = \frac{1}{L_x L_y} \int \mathbf{u} \mathrm{d}x \, \mathrm{d}y \, . \tag{3.9}$$

As a consequence of additional kinetic pressure component in the simulations, we get a nonzero vertical component of mean velocity $\overline{\mathbf{u}}_z$, (Similar to previous simulations by Gressel et al. [2008]) and the other components remain negligible. Reason for the insignificant contribution of the radial and azimuthal velocities is the lack of radial or azimuthal gradients of the random SN explosions. Whereas, the origin of vertical wind component can be understood with an idea of galactic fountain mechanism, which can be generally described as follows. SN shocks produce a vertical flow of ISM gas (directed outwards) within the inner disc, which later, due to the compressional cooling, get condensed to form the high density cold clouds. Such heavy clouds accelerate downwards in the gravitational field and fall back onto the disc. This mechanism, on an average, produces approximately linear 'z' profile of $\overline{\mathbf{u}}$, during the initial kinematic phase. Amplitude of the mean velocity, as a consequence, scales directly with respect to SN rate, which in these simulations turns out as $\overline{\mathbf{u}}(z) \sim \sigma^{0.4}$.

Later during the dynamical phase, $\overline{\mathbf{u}}(z)$ profiles become less steeper in the inner disc parts ($|z| < 0.8\,\mathrm{kpc}$) of models Q and H, while remaining nearly unchanged in model F. This 'flattening' can be understood via a SN dependence of the distribution of mass density as follows: ISM gas in the mid-plane is well distributed over a wide density range of almost three orders of magnitude during the kinematic phases of all models (e.g. $0.02\,\mathrm{cm}^{-3} < \mathrm{n} < 5\,\mathrm{cm}^{-3}$, for model Q), except for the high density tail ($n > 1\,\mathrm{cm}^{-3}$),

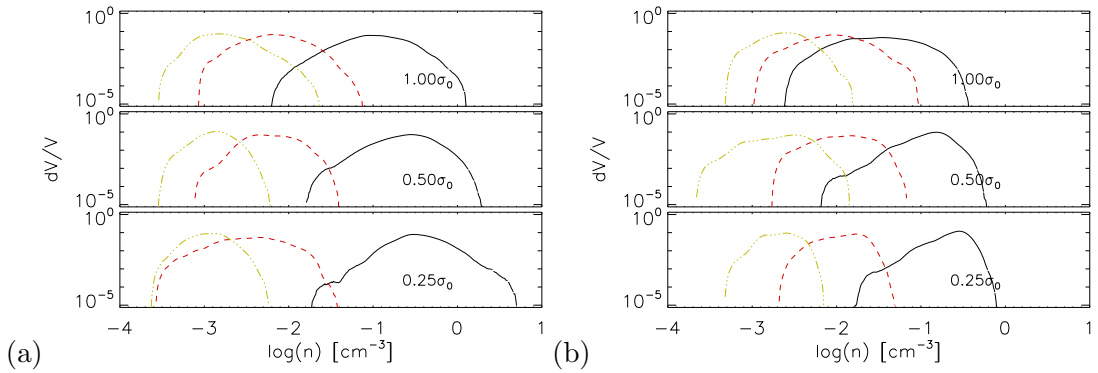

FIGURE 3.11: Distribution of ISM density at $z = 0\,\mathrm{kpc}$ (black-solid lines), at $z = 0.5\,\mathrm{kpc}$ (red-dashed line) and at $z = 1.0\,\mathrm{kpc}$ (green-dot dashed line), plotted for all SN rates, during the kinematic *[Panel a]* phase and during the dynamical phase *[Panel b]*.

the extension of which scales inversely with SN rate, as shown in Figure 3.11 [*Panel a*], (black-solid lines). However, the high density part of these distributions vanishes in the dynamical phase, as a consequence of additional magnetic pressure in the cold dense ISM clouds (described in Chapter 4). Whereas the density distributions at the higher altitudes ($z = 0.5\,\mathrm{kpc}$) shift toward higher density side, with inverse dependence on the SN rate. This still allows a drastic ISM mixing for model F than in models Q and H (as represented in Figure 3.11 [*Panel b*]). Finally, the widths of these distributions (at $z = 0\,\mathrm{kpc}$) narrow down to ~ 2 orders of magnitude, 2.5 for model H, and 3 orders for model F (as the magnetic field does not reach to the dynamically relevant strengths). Lack of the wide range of ISM density, in accordance with a galactic fountain mechanism (described before), reduces the outward wind, predominantly for model Q and, quite less so, for model F. Consequence of such flattening to the dynamo mechanism is elaborated in Chapter 5.

Turbulent velocities in all these models attain the steady vertical profiles within first 50 Myr of evolution, which are inverted bell shaped within the inner disc ($|z| < 0.8\,\mathrm{kpc}$) and linearly decaying in the outer halo part ($|z| > 0.8\,\mathrm{kpc}$). The maximum of $\mathbf{u}'(z)$ is situated at $z = \pm 0.8\,\mathrm{kpc}$, which scales (approximately) with the SN rate as $\sim \sigma^{0.4}$. While for the mid-plane values; we find a much steeper scaling law $\mathbf{u}'(0) \sim \sigma^{1}$ (Table 3.4). The functional form of $\mathbf{u}'(z)$ remains approximately constant throughout kinematic phase, while during the dynamical phase, the maximums of $\mathbf{u}'(z)$ profile shift to $z = \pm 1\,\mathrm{kpc}$, (but follow the same SN scaling law) as shown in, Figure 3.12. Though the approximate shape of $\mathbf{u}'(z)$ and $v_A(z)$ are the same (during the dynamical phase), absolute values of $\mathbf{u}'$ generally remain larger than v_A for all SN rates (this inequality varies significantly

TABLE 3.4: Values of ISM parameters at time 't' listed in the second column. For models Q, H, F and QS t represents the end of kinematic phase. Magnetic energies in models Q and H are still evolving. z values are in kpc

	t [Gyr]	$v_{\rm A}(z=0.8)$ [km s^{-1}]	$\overline{\mathbf{B}}(z=0)$ [μG]		$u'(z=0.8)$ [km s^{-1}]	$u'(z=0)$ [km s^{-1}]	$E_{\rm m}$ [erg]	$E_{\rm kin}$ [erg]
			x	y			$\times 10^{50}$	$\times 10^{50}$
F	0.9	30.0	0.12	1.0	41.2	25.9 ± 4.2	10.5 ± 4.5	119 ± 18.5
H	1.0	26.1	0.10	1.8	31.5	11.8 ± 1.8	7.8 ± 1.2	69.5 ± 6.5
Q	1.2	37.3	0.15	2.0	24.2	6.4 ± 1.0	6.6 ± 1.6	33.0 ± 3
QZ	2.5	20.8	0.10	1.5	29.1	7.0 ± 2.0	10.5 ± 2.5	40 ± 4
QS	1.6	28.1	0.15	2.0	22.2	6.1 ± 0.8	9.5 ± 4.5	36 ± 6
QSZ	1.2	21.1	0.10	1.5	26.0	6.4 ± 1.4	2.1 ± 0.5	33 ± 3
AR	1.9	18.2	0.10	1.7	28.8	6.6 ± 1.6	2 ± 0.6	32.5 ± 4.5

Notes: Values of $\overline{\rm B}_x$ and $\overline{\rm B}_y$ are absolute values. Estimated errors in the components of v_A are ± 5 km s^{-1}.

within the different ISM thermal phases, as explained in Chapter 4).

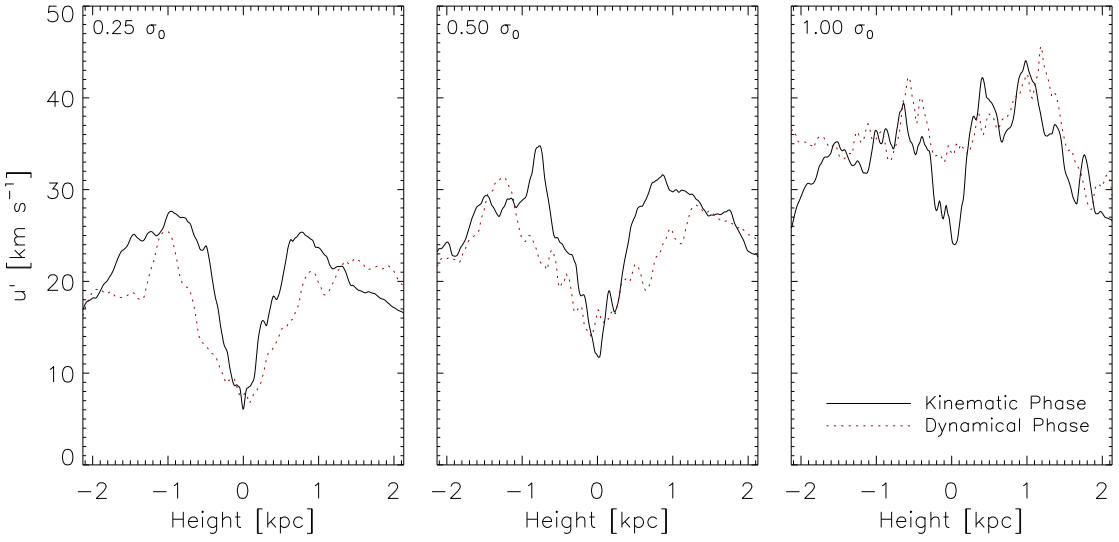

FIGURE 3.12: Typical vertical profiles of u′, during the initial kinematic phase (black-solid lines) and during the dynamical phase (red-dashed line), for models Q, H and F, from left to right.

Chapter 4

ISM Phases

In this chapter we discuss the distribution of ISM in multiple thermal phases and the effects of additional magnetic pressure component on it. In these simulations we were able to replicate some of the observed peculiarities of ISM, although it would be desirable to perform these using a finer resolution; along with the anisotropic heat conduction and the chemical networks, especially to capture the dynamics of cold dense ISM phase. However, our main motivation has been to understand the saturation process of galactic magnetic fields and its implications on the ISM composition. We, therefore evolve these models for longer physical times until the magnetic field amplifies to equipartition strengths and in order for these models to be numerically less expensive, we stick to the relatively coarser resolution. Observationally speaking the roll of magnetic fields on the scale-lengths of dense clouds is not very well understood. It appears that magnetic flux reduces the density contrast in the dense ISM clouds [e.g. Balsara et al., 2001]. Magnetic fields could therefore slow down the rate of core collapse due to magnetic pressure [Tritsis et al., 2015] and may affect the mass distribution and turbulence spectrum of ISM but possibly have a minimal impact on the star formation process itself (considering the fact that the core formation time is much larger than the collapse time itself [e.g. Elmegreen & Scalo, 2004]). Magnetic fields could furthermore affect the field amplification itself via the back-reaction on turbulence, which is discussed in Chapter 5.

4.1 Classification of ISM Phases

For this analysis we divide the ISM in five temperature phases [similar to Hill et al., 2012], nomenclature for these is listed in Table 4.1. Our initial ISM model consists of 40% warm and 60% of transition component, that later splits into a quasi-stationary multiphase structure within initial $\sim$ 20 to 50 Myr and remains almost stationary during the kinematic phase. Transformation to the multiphase structure occurs as a result of the radiative cooling and ambient heating due to SN explosions, which gives rise to a power law correlation between the local density and temperature, $\rho \sim \mathrm{T}^{-a}$, with an exponent a that decreases with SN rate (a = 1.3, 1.1 and 0.9 for models Q, H and F respectively). A qualitative representation of the steady multi-phase structure is shown in Figure 4.1, *[Panel bottom-left]* which shows the density contrast in the mid-plane (as high as $\sim$ 30) that is correlated to the temperature (shown in the adjacent panel). Whereas rest of the panels represent the distributions of other ISM parameters within these phases.

The stationary multiphase state also corresponds to the steady volume and mass filling fractions (VFF and MFF) for all ISM phases which are achieved within 20 to $\sim$ 50 Myr depending upon the temperature. Figure 4.2 represents the time variation of the volume and mass filling fractions of these phases for all SN rates. Values of these fractions generally match with the high resolution simulations which are focused specifically on the study of ISM properties [e.g. Breitschwerdt et al., 2012; Joung & Mac Low, 2006] except for the cold phase, in which we get comparatively smaller VFF and MFF values. This could, however, be attributed to our coarser resolution.

TABLE 4.1: Nomenclature of the ISM thermal components and corresponding average pressures in the mid-plane for model Q. Last 2 columns indicate the percentage VFF and MFF of ISM components for the same model.

	T K	ρ_T cm^{-3}	P_{th} 10^{-14} Pa	P_k 10^{-14} Pa	VFF %	MFF %
Cold	$0 - 200$	10	2	4	0.02	3
Cool	$200 - 5000$	1	5	1.5	1.9	28
Warm	$5000 - 10^{4.4}$	0.1	6	1.5	20	62
Transition	$10^{4.4} - 10^{5.5}$	5×10^{-3}	10	15	55	6.5
Hot	$> 10^{5.5}$	5×10^{-5}	100	50	23	0.25

During the kinematic phase; mid-plane averages of total pressure in cold, cool and

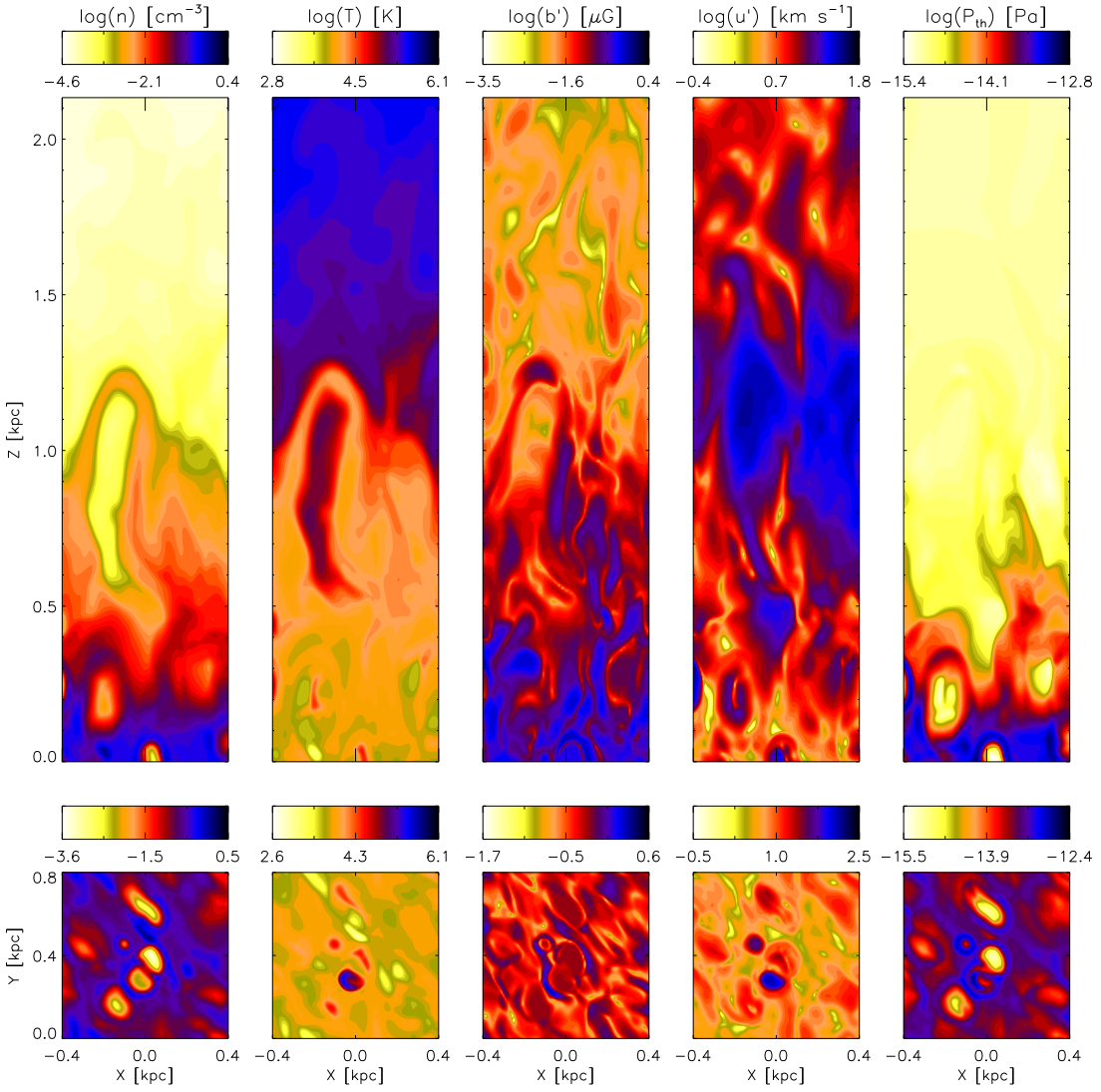

FIGURE 4.1: Horizontal (xy plane, at $z = 0$) and vertical (xz plane, at $y = 0.4\,\mathrm{kpc}$) cross sections of the simulation domain, during the dynamical phase. Color-code represents the strengths of corresponding ISM parameter. Panels from left to right represent number density, temperature, turbulent magnetic field, turbulent velocity and thermal pressure.

warm thermal components are approximately equal. The transition and hot components, however, remain thermally over pressured. In Table 4.1 we have listed a typical average pressure composition in the mid-plane of model Q, in the kinematic phase. This mid-plane pressure composition differs only slightly for model H and F, such that the contribution of $P_{\rm th}$ in hot and transition ISM slightly decrease as we go from model Q to F [1].

Vertical structure of the model is supported via the balance between the gradient of

[1] However, the average pressure composition in the mid-plane is quite different than in the entire box.

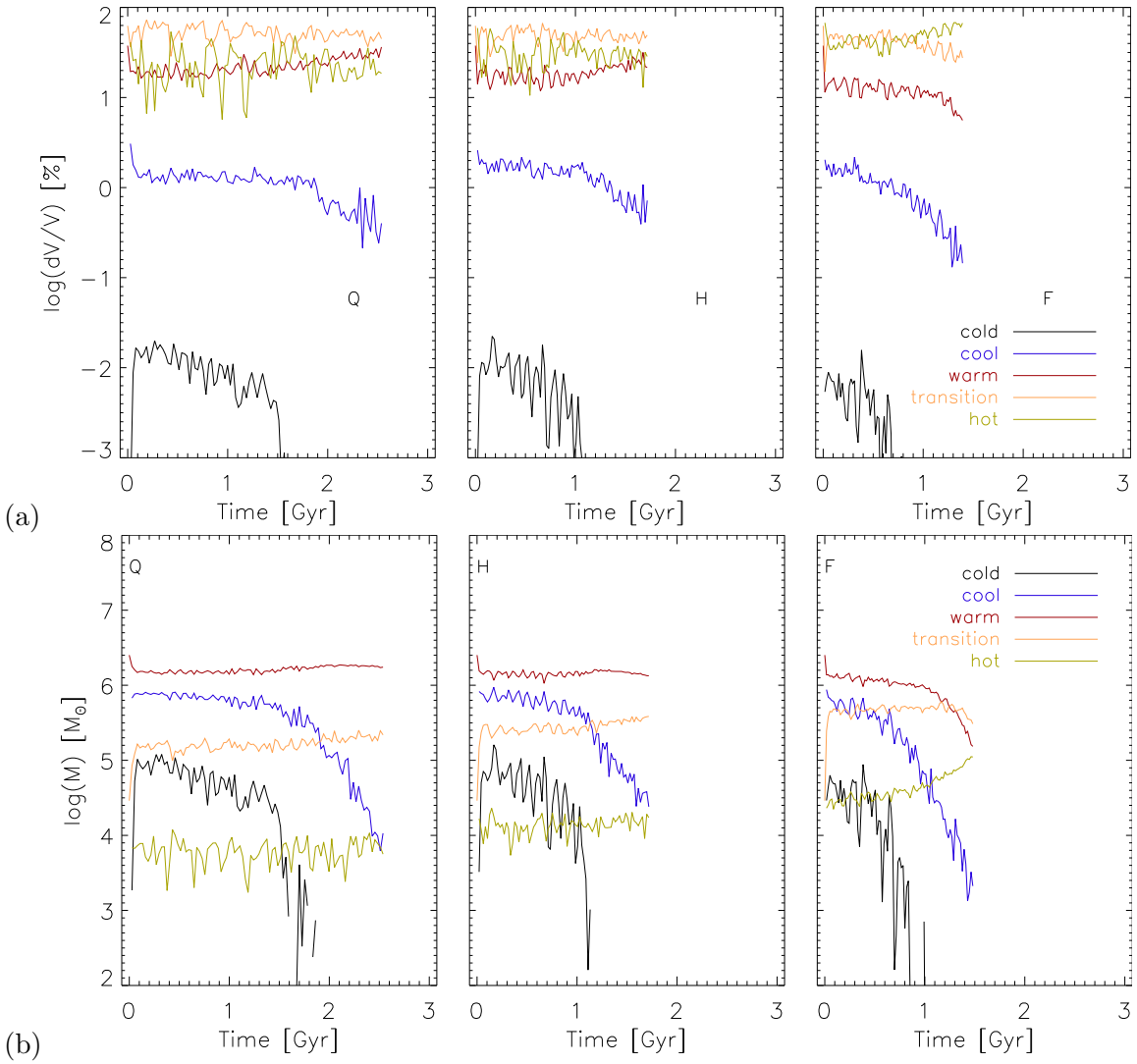

FIGURE 4.2: (a) Evolution of the volume filling fractions of ISM components for, models Q, H and F, from left to right. (b) Same as *[Panel-a]* but for the evolution of total mass of all ISM components for all SN rates.

total pressure, ($P_{\rm tot} \equiv P_{\rm k} + P_{\rm th} + P_{\rm m}$) and gravitational pull. The resultant vertical profiles of average ISM mass density can be expressed as a sum of three different exponential functions, roughly signifying its visually distinctive parts. Namely; central thin disc, intermediate thick disc and upper halo (Equation 3.1). Scale-heights of these exponentials stay approximately constant throughout the evolution but scale roughly as a direct function of SN rate as indicated in Table 3.2. The situation is quite different for each thermal component separately. Vertical profiles of mass density in different thermal components ($\rho^T(z)$), for instance, have distinctive scale-heights, that depend upon the SN rate as well as on the magnetic field strength. We find that the z profiles of ρ^T (except for the cold component) can be split into only two visually identifiable

parts; the middle disc and the broad upper halo. We therefore, chose to fit it with a superposition of two exponential functions with different scale-heights as;

$$\rho T(z) \simeq \sum_{i=0}^{1} \rho_i \, \exp\left(\frac{-|\, z \,|}{r_i}\right) . \tag{4.1}$$

Where r_0 and r_1 roughly correspond to the exponential scale-heights within the disc and in the outer halo, which we further find to have a dependence upon the dynamically significant mean field strengths. Dependence of r_i on the SN rate and magnetic field strength, is mentioned in the description of each thermal component. For the cold component, however, $\rho^T(z)$ profiles are best fitted with the Gaussian function.

Similar to the volume filling fractions, kinetic and thermal energies of all ISM components also remain approximately invariant during the kinematic phase and the kinetic energy is contributed mostly by the transition component. Whereas the hot and warm ISM components dominantly contribute to the thermal energy. In order to get a quantitative feeling of the dynamical importance of magnetic energy (in each component), we have listed the ratios of E_m/E_{th} and E_m/E_{kin} at the end of kinematic phase for each thermal component in Table C.1. The distribution of these ratios within the various ISM components is different for the inner disk ($|z| < 0.5\,\mathrm{kpc}$) and in the outer halo ($|z| > 0.5\,\mathrm{kpc}$). For instance, in the inner disc part, most of the magnetic energy lies within the warm component, whereas if we consider the total box, the ratio E_m/E_{kin} is dominated by the dense cold component.

In the following sections we have analyzed the composition of different ISM components separately for all SN rates. Models QS, QSZ, QZ, and AR are not separately mentioned, since they have the same composition as model Q.

4.2 Cold Component

High density ISM fragments are generated due to the interacting SN shock fronts, which mostly belong to the transition temperature range. These fragments further cool down due to the radiative cooling in assistance with the thermal instability, to form the dense cold component. This component is situated within the vertical range of $\sim 100\,\mathrm{pc}$ in the

TABLE 4.2: Composition of the pressure for all ISM components (at $z = 0$), at the end of kinematic phase. All pressures are expressed in the units of 10^{-14} Pa. t is the e-folding time for the kinematic amplification of E_m within the corresponding thermal component.

	Cold	Cool	Warm	Transition	Hot
model Q					
P_{th}	2	5	6	10	100
P_{kin}	4	1.5	1.5	15	50
P_{mag}	1	0.8	1	0.5	0.1
t [Myr]	45	45	80	120	110
model H					
P_{th}	2	4	6	6	80
P_{kin}	7	2.5	2.5	10	40
P_{mag}	3	1.5	1.5	0.8	0.3
t [Myr]	60	75	95	130	100
model F					
P_{th}	2	4	6	4.5	50
P_{kin}	14	4.5	4.5	7	20
P_{mag}	0.2	1.0	2.5	1.0	0.1
t [Myr]	70	80	80	90	100

form of elongated clouds with average lengths of 20, 30 and 50 pc for models Q, H and F respectively. Average temperature of these clouds ranges from 80 to 150 K (depending upon σ), we further find an approximate scaling between the thermal pressure and mass density, such that $P_{\rm th} \sim \rho^{\gamma}$, with the effective γ of 0.35 for model Q, and 0.65 for model F. γ of 0.65 for model F (with parameter set equivalent to the Milky Way) is comparable to the observations of interstellar CI structures by Jenkins & Tripp [2011] (and also with the simulations by Hill et al. [2012]). We, therefore identify them as the dense molecular clouds of the cold neutral medium (CNM). Although it must be mentioned that; we do not get a highly dense phase with the temperature less than 50 K.

VFF for the cold component increases from 0 to 0.01% within first 50 Myr and stays nearly constant during the kinematic phase (which is much smaller than some previous high resolution simulations which were focused on the analysis of ISM properties [e.g. Breitschwerdt et al., 2012; Hill et al., 2012]. A reason for this probably lies the relatively coarser resolution we have used. Vertical profile of the average density for this component is approximated via a Gaussian profile, for which 'the full width half maximums' seem to scale directly with SN rate, these are 70 pc, 102 pc and 160 pc for model Q, H and F, respectively. Turbulent velocities of this component are approximately 2, 3.5 and 7 km s^{-1} for Q,H and F respectively, which are comparable to observations as discussed in

Sellwood & Balbus [1999], however the cold molecular clouds with average temperatures $< 50K$ are not formed here.

Total magnetic energy corresponding to the cold component, (that is the local magnetic energy density integrated over the volume of cold gas) rises rapidly for initial few 100 Myr (with approximate exponential growth time of 45, 60 and 70 Myr for models Q, H and F respectively) and stays constant during rest of the kinematic phase. Corresponding ratios of magnetic to the turbulent kinetic energies are listed in Table C.1. As models evolve to the dynamical phase cold ISM component is vanished for all SN rates due the additional magnetic pressure. In order to verify whether the loss of cold phase is because of the additional magnetic pressure and not associated with the overall mass loss from the box, we point at the sustained occupancy faction of cold component in model QZ, in which the overall mass loss occurs at a same rate as model Q. But the dynamical phase in QZ is achieved only after $t \simeq 2.3$ Gyr (as opposed to $t \simeq 1.2$ Gyr for model Q). However, unlike model Q; the cold component in model QZ, survives until 2.3 Gyr (Figure 4.4, *[Top panel]*, and inset showing a rate of relative mass loss). Another argument to refute the hypothesis that 'the magnetic pressure is responsible for the destruction of clouds' would be to suggest that: not the overall mass; but the average density (of all ISM components combined) in the thin inner disc ($|z| < 90$ pc, where the cold component is mainly formed), itself reduces to the values so small that the interacting shock fronts could no longer produce a sufficient density contrast to form the cold phase (via radiative cooling). However, we again compare the average densities (of all ISM components combined) in the central discs of models Q and QZ in Figure 4.4, *[Central panel]*. From this figure we infer that the rate at which the central density decays is same for models Q and QZ, while the cold component vanishes at different times, at which the ratio of magnetic to kinetic energy (β_{tot}) in the central disc ($|z| < 90$ pc), is same; as shown in Figure 4.4 *[Bottom panel]*.

Also for model QS, the SN and overall mass loss rates are same as model Q, but the ratio E_m/E_k within the cold component, is only ~ 0.2 for model QS (Table C.2) even in the dynamical phase (for model Q, $E_m/E_k \sim 1$, at the end of kinematic phase Table C.1). Subsequently we see the preservation of cold component until the end of evolution (1.6 Gyr) (Figure 4.3), again indicating that the loss of cold component, in models Q, H and F is associated with the increased magnetic pressure.

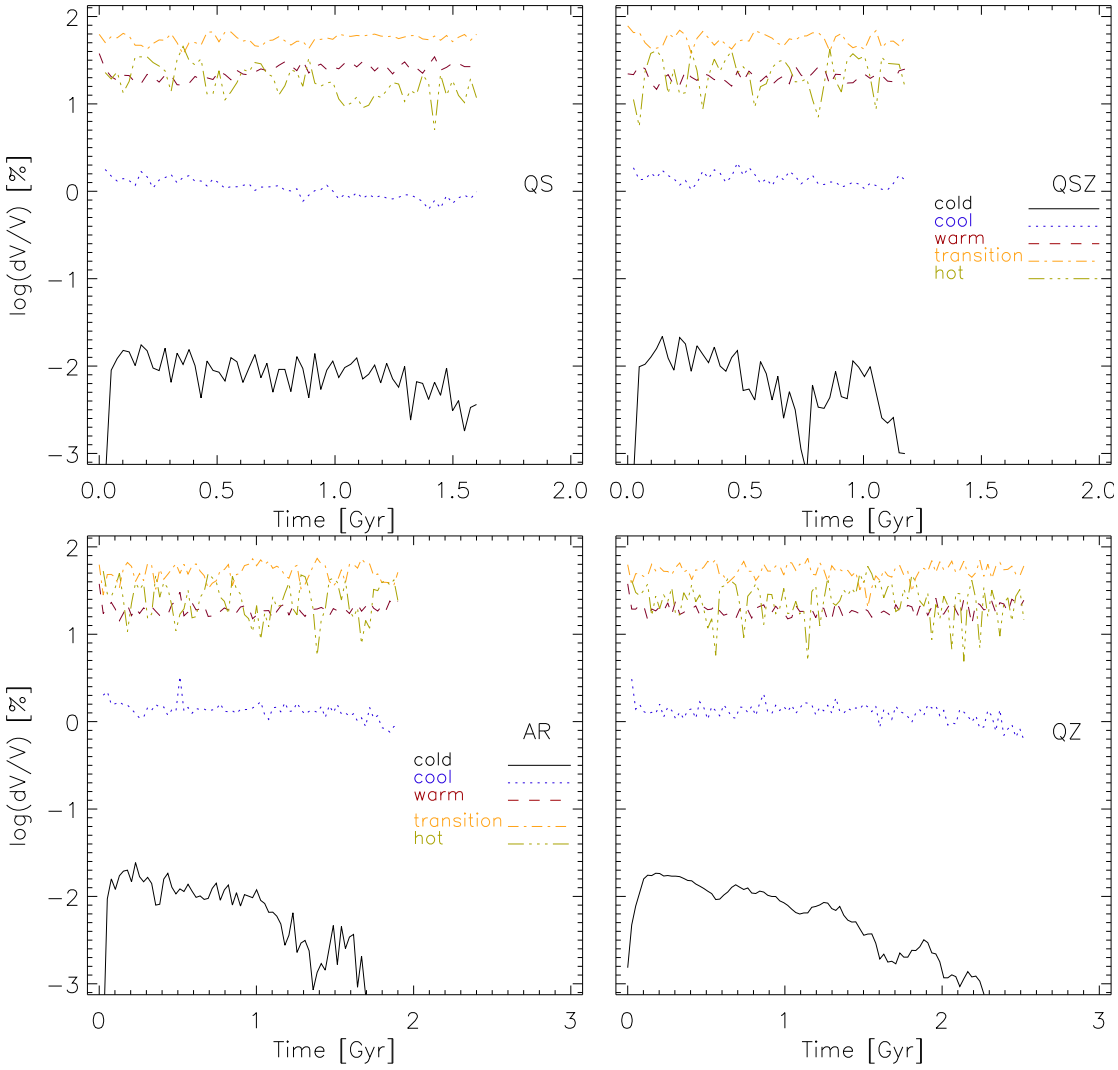

FIGURE 4.3: Evolution of volume filling fractions of ISM components in models QS, QSZ, QZ and AR.

4.3 Cool Component

The cool component is a thermally unstable phase (as established by the cooling curve we have used) that is situated within the range -400 to $+400$ pc also in the form of elongated clouds. Average lengths of these clouds are ~ 100 pc. Cool component builds up within the first 100 Myr (also due to the radiative cooling of dense SN shock fronts) and keeps its VFF constant during the kinematic phase (VFF $\sim 1.5\%$). The average density corresponding to this component is about $0.6\,\mathrm{cm}^{-3}$ and the turbulent velocities are about 8, 10 and $15\,\mathrm{km\,s}^{-1}$ for models Q, H and F respectively. Average density of cool component has the exponential scale-heights; r_0, of 50 ± 5 pc, and $r_1 = 140 \pm 10$ pc, for model Q. We moreover find these scale-heights to be directly proportional with SN

rate as $r_0 \sim \sigma^{0.4}$ and $r_1 \sim \sigma^{0.4}$. Later in the dynamical phase VFF slowly decays by almost 20 - 30%, and scale-heights r_0 and r_1 become wider by about 70% and 40% respectively (for all SN rates). Whereas the average u' and ρ remain constant (even during the dynamical phase). Magnetic energy within this component amplifies initially with e-folding times of $\sim 70\,\mathrm{Myr}$ and saturates eventually during the dynamical phase for all SN rates.

4.4 Warm Component

The warm component is present in the form of shredded clumps of average size, $l \simeq 150\,\mathrm{pc}$ within the inner disc. This size, l, increases with height, such that above $z = 1\,\mathrm{kpc}$; $l \simeq 400\,\mathrm{pc}$. VFF of the warm component also goes to a quasi-stationary value of $\sim 60\%$ in $\sim 50\,\mathrm{Myr}$. Vertical scale-heights of ρ^T for the warm component, scale with σ with the same scaling law; that is $r_0,\ r_1 \sim \sigma^{0.4}$ ($r_0 = 100\,\mathrm{pc}$ and $r_1 = 320\,\mathrm{pc}$ for the model Q). This scaling law preserves later in the dynamical phase as well, however, the exact values of r_0 and r_1, are increased by 20 to $\sim 30\%$, ($r_0 = 120\,\mathrm{pc}$ and $r_1 = 420\,\mathrm{pc}$ for the model Q) consistent with the slight increase in mass during dynamical phase (Figure 4.2). If we consider only the central disc of $|z| < 0.5\,\mathrm{kpc}$, the ratio of total magnetic to turbulent kinetic energy within warm component; is the highest one, but if we consider the total box, the cool component also holds a comparable ratio of E_m/E_k (Table C.1). Other parameters, such as; average cloud size and VFF are also affected during the dynamical phase as explained below. Average size of the warm cloud in the mid-plane increases to $\sim 250\,\mathrm{pc}$ during the dynamical phase, crudely suggesting a transformation towards more uniform ISM in the mid-plane along with loss of dense cold ISM. Since the formation of cold and cool components is hindered during the dynamical phase as a consequence of increased magnetic pressure, the radiatively cooled transition ISM aggregates mostly into the warm component, and the corresponding volume filling fraction rises slowly, until the overall mass loss from the box starts to appear (overall mass loss rates are approximately 240, 455 and $1000 M_\odot\,\mathrm{Myr}^{-1}$ for model Q, H and F respectively).

4.5 Transition Component

Starting from the initial 60% occupancy, VFF of the transition component saturates to $\sim$ 45 to 50% within first 100 to 200 Myr (and corresponding MFF values are 5%, 10%, and 20% for model Q, H and F, respectively). This transformation occurs due to the balance between ambient heating by SN explosions and the radiative cooling of dense ISM clumps formed at the SN shock fronts. Transition component occurs mostly in the form of large clouds within the vertical range of $|z| < 1$ kpc. Average length scale of these clouds is $l \simeq 50$ pc, which is apparently independent of SN rate (l approximately equals to the scale-height of a SN explosion remnants). Above $z = 1$ kpc, transition component exists only in the form of large super bubbles of the average length $l \simeq 200$ pc and with the average density of $\sim 0.001\,\mathrm{cm}^{-3}$ (these remain roughly constant throughout the evolution). Average scale-heights of this component (r_0 and r_1) scale as $\sigma^{0.4}$ during the kinematic phase ($r_0 = 120$ pc and $r_1 = 600$ pc for the model Q). Later in the dynamical phase; inner scale-heights, r_0 increase by about 60% while r_1 remain roughly constant ($r_0 = 200$ pc and $r_1 = 600$ pc for the model Q).

4.6 Hot Component

The hot component is formed as a result of ambient heating of the transition gas and is mainly situated in the outer halo part. VFF of this component saturates to $\sim$ 30% in first 100 Myr of evolution. In the vertical range of approximately 0.8 kpc $< |z| <$ 1.2 kpc, this component is present mainly in the form of large bubbles (with an average size of $\sim$ 250 pc and with the average density of $10^{-3}\,\mathrm{cm}^{-3}$) while above this height ($|z| > 1.2$ kpc) it exists in the diffused continuous form (with the average density of $\sim 10^{-4}\,\mathrm{cm}^{-3}$). In the inner disc ($|z| < 0.8$ kpc) the hot component is scarcely present, but primarily in the form of elongated clouds of average width of $\sim$ 50 pc (which is also equivalent to the average size of the SN remnants) and with average density of $\sim 10^{-2}\,\mathrm{cm}^{-3}$, which is slightly higher than the hot halo. Resulting vertical distribution of the density of this component in the halo, is therefore very broad compared to the distribution within the disc, such that the scale-heights of the average density profile are $r_0 \simeq 50$ pc and $r_1 = 1$ kpc. Both r_0 and r_1 scale with the SN rate as $\sim \sigma^{0.4}$ throughout the evolution but the exact value of r_0 is approximately doubled during the dynamical phase while

r_1 remains unchanged (for all SN rates). Compared to the other components, total pressure within the hot component is about an order of magnitude larger; which is mostly contributed by the thermal pressure (see for example Table 4.2). Whereas the ratio of E_m to E_k, during the dynamical phase is smallest for this component. Average turbulent velocities, on the other hand, are highest for this component and remain nearly unchanged during the dynamical phase ($\mathrm{u}' \sim 80\,\mathrm{km\,s^{-1}}$) as there is no significant impact of the magnetic pressure, which is reflected into the values of corresponding Alfvén velocities $\sim 15\,\mathrm{km\,s^{-1}}$ that are much smaller than the turbulent velocities.

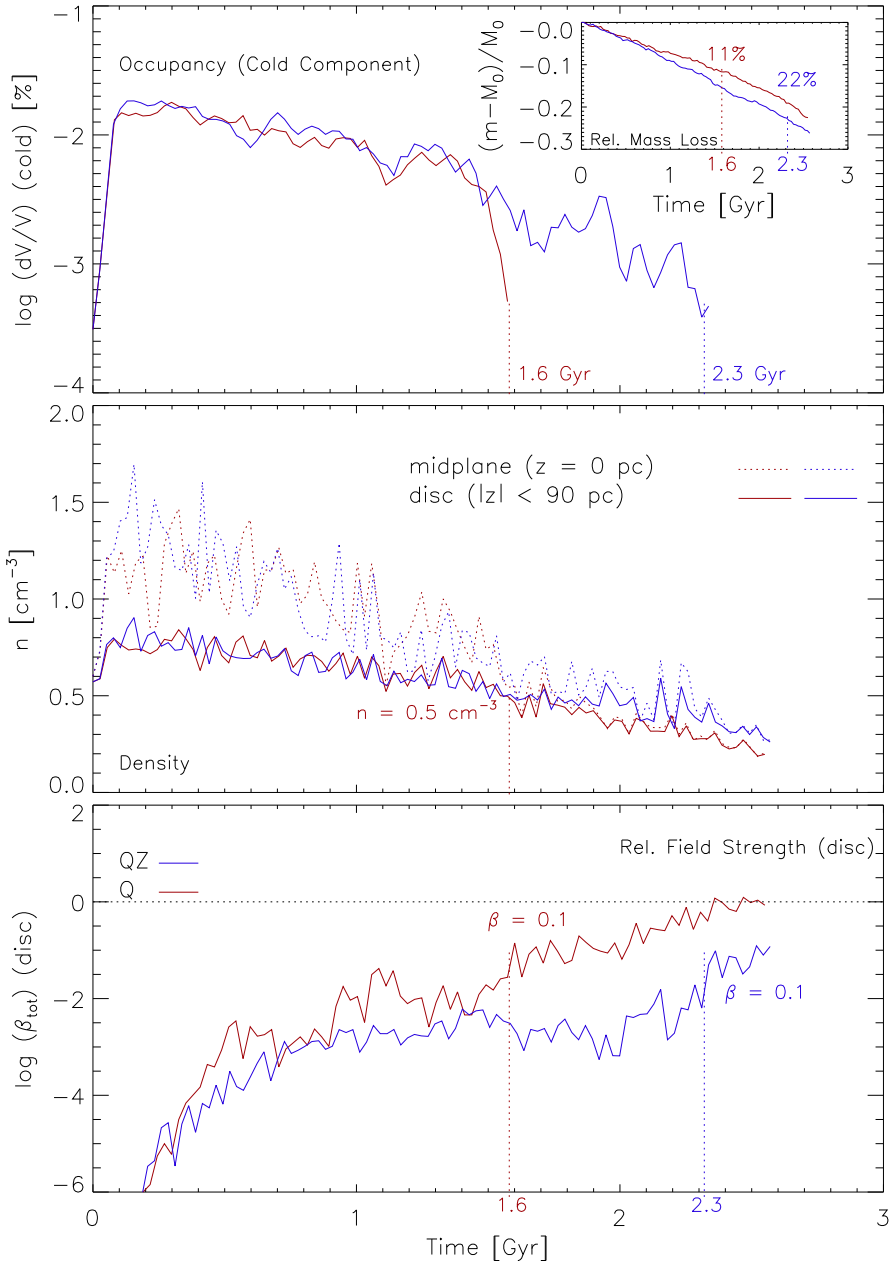

FIGURE 4.4: Blue lines indicate the evolution of model QZ, and the red lines signify the same for model Q; *Upper panel*: Time evolution of the volume filling fraction of the cold component in the models Q and QZ, and the inset shows the relative mass loss for these models versus time. *Central panel*: Time evolution of the average density in the central disks ($|z| < 90\,\mathrm{pc}$) of the models Q and QZ, shown in solid lines and dotted lines indicate the same for mid-plane (at $z = 0$). *Bottom panel*: Time evolution of the total relative field strengths ($\beta_{tot} = E_m/E_k$) in the central discs of the models Q and QZ. Cold component in the model Q vanishes completely at $t = 1.6\,\mathrm{Gyr}$, as opposed to model QZ for which $t = 2.3\,\mathrm{Gyr}$, corresponding β_{tot} for both models is ~ 0.1.

Chapter 5

Saturation of Galactic Dynamo

5.1 Introduction

In previous chapters we have discussed the overall evolution ISM magnetic energy and the dynamics of interstellar gas in various thermal phases, for the different rates of SN driving. General effects of the dynamically significant magnetic fields on ISM parameters have also been elaborated in Chapter 4. Outcomes of these simulations are generally consistent with the typical findings of the observations of nearby spiral galaxies on a $\sim$ kpc scale. Following is a brief summary of the main results of these simulations.

1. Starting from the seed magnetic fields of $\sim$ nG strength, total magnetic energy for all SN rate models, amplifies exponentially, with a typical e-folding time of 100 Myr (roughly independent of the SN rate).

2. After the initial kinematic phase of constant growth, the magnetic energy in all SN models, depending on the SN rate, either saturates or keeps growing with comparatively slow growth rates.

3. Magnitude of total magnetic energy at which the kinematic amplification stops, scales directly with the SN rate.

4. Large scale regular magnetic fields, of a few μG strengths are generated within a $\sim$ Gyr in SN rate models, with the average pitch angles of approximately 10^0, 12^0 and 18^0 for models Q, H and F, respectively.

5. Fast outward winds are generated in all models within the initial few tens of Myr, amplitudes of which depend directly on the rate of SN explosions. During the dynamical phase, however, these amplitudes slowly decline within the inner disc part of approximately $|z| < 0.8\,\mathrm{kpc}$ depending on the relative strength of magnetic field.

In this chapter we interpret above results in the context of the mean field dynamo. The reason to do so is two fold. First one is to provide a self consistent justification for amplification and saturation of magnetic energy and the second one lies in the formulation of a dynamo model itself; as follows. The mean field dynamo model describes the evolution of mean magnetic field in terms of the mean turbulent electromotive force, which can be interpreted as the function of the well defined physical properties of turbulent motions (such as helicity, turbulent diffusion, turbulent velocity amplitude, etc.) and thereby providing an effective means to estimate the importance of each physical effect to the dynamo action, separately. A partially similar approach has already been used by Gressel et al. [2008] to explain the initial kinematic growth phase of magnetic field. Here we use a similar model in assistance with the so called quenching formulation to understand the dynamical evolution of magnetic energy. In first few sections we discuss the general concept and the formulation of dynamo theory and later we analyze the results of DNS in comparison with 1D dynamo simulations.

5.2 Mean Field Dynamo Theory

Formal idea of the dynamo mechanism was first put forth by Parker [1955], which can be described as follows. Considering the geometry of a disc galaxy, it is convenient to use the cylindrical coordinate system, with its origin located at the galactic center, and assume the galaxy as a differentially rotating disc of turbulent plasma, with its angular velocity vector parallel to the z axis. Subject to the thin disc approximation for spiral galaxies, it is possible to neglect all the gradients along radial and azimuthal directions as compared to the verticals ones [e.g. Shukurov, 2004; Soward, 1978, 1992a,b]. It is further possible to decompose the local magnetic field as a sum of its toroidal and poloidal components. For axisymmetric magnetic fields, toroidal and poloidal parts simply turn out to be azimuthal and radial + vertical components respectively. In such

rotating turbulent plasma system any vertically convecting cloud of plasma stretches the planar component (parallel to galactic disc) of the regular field passing through it, in the vertical direction. This continues until the field diffuses away from the cloud (due to the turbulent and macroscopic diffusivity). Such rising cloud rotates under the Coriolis acceleration in the rotating frame of reference and twists the frozen in toroidal field lines to form the poloidal ones. Poloidal field lines (non-axisymmetric; as a general case) on the other hand, are spirally wound up in a differentially rotating flow and form a non-zero toroidal component. High wave number toroidal component, thus formed, is prone to the turbulent diffusion. So the extent to which the spiral winding would occur is decided by the length scales of turbulent diffusivity. This process, if the diffusion is weaker compared to rotation and vertical convection, systematically leads to the exponential amplification of mean magnetic field.

This mechanism can be mathematically formulated with mean-field electrodynamics, in which the flow variables (velocity, $\mathbf{u}$ and magnetic field $\mathbf{B}$) are split as a sum of their respective mean and fluctuating components. Mean part is defined by applying an arbitrary averaging process that satisfies the Reynold's averaging rules (which justifiably hold for the situation in which there is a clear separation of small and large scales Krause & Rädler [2013]). So the magnetic field and velocity can be written as $\mathbf{B} = \overline{\mathbf{B}} + \mathbf{b}'$ and $\mathbf{u} = \overline{\mathbf{u}} + \mathbf{u}'$; implying that $\overline{\mathbf{b}'} = \overline{\mathbf{u}'} = 0$ (overbar indicates the average). In the aforementioned scenario (also depicted in Figure 1.4) average was actually defined over the azimuthal coordinate. By substituting the decompositions of $\mathbf{B}$ and $\mathbf{u}$ in the induction equation (last equation from Equation 2.1) and further averaging, we get the evolution equation for mean magnetic field, such that;

$$\frac{\partial \overline{\mathbf{B}}}{\partial t} - \nabla \times \left(\overline{\mathbf{u}} \times \overline{\mathbf{B}} - \tilde{\eta} \nabla \times \overline{\mathbf{B}} + \mathcal{E} \right) \quad = \quad 0 \,, \tag{5.1}$$

this equation is similar to the regular induction equation, except for an extra term ($\nabla \times \mathcal{E}$). '$\mathcal{E}$' here is referred as the turbulent electromotive force (EMF) and expressed as $\mathcal{E} = \overline{\mathbf{u}' \times \mathbf{b}'}$. Mathematically speaking, $\mathcal{E}$ is a first order statistical correlation between the fluctuating magnetic field ($\mathbf{b}'$) and turbulent velocity ($\mathbf{u}'$). $\mathcal{E}$ is an averaged quantity with a same definition of averaging that was used to define $\overline{\mathbf{B}}$ (and $\overline{\mathbf{u}}$).

Computation of turbulent EMF is a crucial step in the formulation of mean-field dynamo. For that, it is necessary to compute the evolution of $\mathbf{b}'$. Equation for $\mathbf{b}'$ can simply be written using Equation 5.1 and the induction equation as;

$$\frac{\partial \mathbf{b}'}{\partial t} - \nabla \times (\overline{\mathbf{u}} \times \mathbf{b}') - \nabla \times (\mathbf{u}' \times \mathbf{b}') + \nabla \times \mathcal{E} - \tilde{\eta} \nabla^2 \mathbf{b}' \;=\; -\nabla \times (\mathbf{u}' \times \overline{\mathbf{B}})\,. \quad (5.2)$$

This equation implies that, $\mathbf{b}'$ (and $\mathcal{E}$) can be expressed as a sum of a linear, homogeneous function of $\overline{\mathbf{B}}$ and a function independent of $\overline{\mathbf{B}}$. A widely used SOCA approximation (second order correlation approximation) allows to express $\mathcal{E}$ in terms of, mean magnetic field [e.g. Krause & Rädler, 2013; Rädler, 2007], in this approach the terms higher than second order in the Taylor expansion of the homogeneous part of $\mathcal{E}$ are omitted, and within the sufficiently small turbulent correlation time interval τ_c; turbulent EMF is expressed as;

$$\mathcal{E} = \alpha \overline{\mathbf{B}} - \eta \nabla \times \overline{\mathbf{B}}\,. \quad (5.3)$$

Tensorial quantities α and η are referred as the dynamo coefficients, which depend solely on the statistical properties of turbulence. In order physically interpret these parameters let us consider the evolution equation of $\overline{\mathbf{B}}$, after substituting Equation 5.3 in Equation 5.1, such that,

$$\frac{\partial \overline{\mathbf{B}}}{\partial t} - \nabla \times \left(\overline{\mathbf{u}} \times \overline{\mathbf{B}} - (\eta + \tilde{\eta}) \nabla \times \overline{\mathbf{B}} + \alpha \overline{\mathbf{B}} \right) \;=\; 0\,. \quad (5.4)$$

The coefficient η in this equation appears in the form of a diffusion coefficient for mean magnetic field. What it actually represents is the magnetic diffusivity due to the turbulence. While α coefficient encapsulates the effect of the helical flows on the growth of $\overline{\mathbf{B}}$. Both of these interpretations become clearer in a simple case of isotropic and homogeneous turbulence, within the high conductivity limit, where α and η reduce to the following simple forms;

$$\begin{aligned} \alpha_{diag} &= -\frac{\tau_c}{3} \overline{\mathbf{u}' \cdot (\nabla \times \mathbf{u}')}\,, \\ \eta_{diag} &= \frac{\tau_c}{3} \overline{\mathbf{u}'^2}\,, \end{aligned} \quad (5.5)$$

where the product $\overline{\mathbf{u}' \cdot (\nabla \times \mathbf{u}')}$ is actually the kinetic vorticity of turbulent motions.

Validity of these estimates (Equation 5.5), however, is rather restricted to the aforementioned special case. Nevertheless it provides a self consistent way to analyze the effect of the turbulence properties on dynamo.

Using the data from from direct MHD simulations we derive the values of corresponding dynamo coefficients and try to explain the evolution of magnetic energy in direct MHD simulations in the context of mean field dynamo. In following section we describe the method we use to compute the dynamo coefficients in DNS models.

5.3 Dynamo Coefficients

5.3.1 Test-Fields Method

To compute the evolution of the vertical profiles of the coefficients of dynamo tensors α and η in DNS models, we use the test field method [Schrinner et al., 2005, 2007], implemented by [Gressel, 2010]. We first decompose the flow variables into their mean and turbulent parts with the average defined on $x-y$ plane, leaving z as the only independent coordinate. $\mathcal{E}$ in this scenario also becomes a function of z. The choice of periodic boundary conditions in x and y directions along with the solenoidal constraint, assures the conservation of $\overline{B}_z(z)$ throughout the evolution. Now by choosing the small initial magnitude of $\overline{B}_z(z)$, we can furthermore neglect the α part of $\mathcal{E}_z$ and Averaging over $x-y$ plane also allows us to neglect diffusive part of $\mathcal{E}_z$ (since the it only involves the x and y derivative terms, which are zero by the definition of averaging used here). We can, therefore, drop the $\mathcal{E}_z$ component altogether and write Equation 5.3 in the matrix form as;

$$\begin{bmatrix} \mathcal{E}_x \\ \mathcal{E}_y \end{bmatrix} = \begin{bmatrix} \alpha_{xx} & \alpha_{xy} \\ \alpha_{yx} & \alpha_{yy} \end{bmatrix} \begin{bmatrix} \overline{\mathbf{B}}_x \\ \overline{\mathbf{B}}_y \end{bmatrix} - \begin{bmatrix} \eta_{xx} & \eta_{xy} \\ \eta_{yx} & \eta_{yy} \end{bmatrix} \frac{\partial}{\partial z} \begin{bmatrix} -\overline{\mathbf{B}}_y \\ \overline{\mathbf{B}}_x \end{bmatrix} . \tag{5.6}$$

Equation 5.6 is a system of two simultaneous equations with eight unknowns (the elements of dynamo tensors) and we have two known variables from DNS (x and y components of mean magnetic field) which are insufficient to invert Equation 5.6. The mean field formulation based on the SOCA approximation should, however, hold for

arbitrary magnetic field. We can, therefore, evolve any predefined magnetic field vector and invert Equation 5.6, to obtain the values of α and η coefficients, without the loss of generality. Exploiting this freedom, we place four additional 'test field' profiles ($\overline{\mathbf{B}}^{\nu}$, with $\nu \in [1, 2, 3]$) in the computational domain and let them evolve passively along with Equation 2.1. These predefined test field profiles are;

$$\overline{\mathbf{B}}^{0}(z) = \cos(k_1 z)\,\hat{x}\,, \tag{5.7}$$

$$\overline{\mathbf{B}}^{1}(z) = \sin(k_1 z)\,\hat{x}\,, \tag{5.8}$$

$$\overline{\mathbf{B}}^{2}(z) = \cos(k_1 z)\,\hat{y}\,, \tag{5.9}$$

$$\overline{\mathbf{B}}^{3}(z) = \sin(k_1 z)\,\hat{y}\,. \tag{5.10}$$

Fluctuations in each of these profiles are recorded as a function of time. Additionally the components of $\mathcal{E}$, corresponding to each test field, are calculated using the relation ${\mathcal{E}^{\nu}}_{i} = \overline{\mathbf{u}' \times \mathbf{B}^{\nu}}$. '$z$' profiles of the coefficients of α and η tensors are then easily obtained as a function of time by inverting the tensorial equation Equation 5.6 for each SN rate.

Computed dynamo tensors α and η are antisymmetric for all models (such that $\alpha_{xy} = -\alpha_{yx}$ and $\eta_{xy} = -\eta_{yx}$). We, therefore, adopt a simplified notation such that, $\gamma = 0.5\,(\alpha_{yx} - \alpha_{xy})$ and $\delta = 0.5\,(\eta_{xy} - \eta_{yx})$. Off- diagonal terms of the α tensor represent the transport of mean magnetic field components in the vertical direction, due to the gradient of turbulence intensity. The emergent antisymmetry in the α tensor, therefore implies that the γ term can be interpreted as the rate of non-advective transport of magnetic flux. This interpretation can be well understood in the special case of isotropic and homogeneous turbulence within high conductivity limit, where γ simply reduces to the function of the gradient of turbulent intensity; $\gamma = -\tau_c \nabla \mathrm{u}'^2/6$. In the evolution equation of the mean magnetic fields, term γ appears only in the form of a transport term (that is $(\overline{u}_z + \gamma)$). DNS data reveals that $\gamma(z)$ has a sign opposite of $\overline{u}_z$ indicating the fact that the diamagnetic pumping term acts in the downward direction, against the outward wind. This is also reflected in the closure form of γ ($\gamma = -\tau_c \nabla \mathrm{u}'^2/6$), since the intensity of turbulence increases in the outward direction.

Vertical profiles of all dynamo coefficients (α_{xx}, α_{yy}, γ, η_{xx}, η_{yy} and δ) peak at $z \simeq \pm 1.2\,\mathrm{kpc}$, and outside this range the profiles are fluctuating (average errors are of the order of $\sim 20\%$). The profiles $\alpha_{xx/yy}(z)$ and $\gamma(z)$ coefficients are approximately linear within the vertical range of $|z| < 1.2\,\mathrm{kpc}$, while they are inverted bell shaped for $\eta_{xx/yy}$

TABLE 5.1: Dynamo coefficients and outward wind velocities (at $z = 1\,\mathrm{kpc}$), during the initial kinematic phase, along with their maximum errors. Amplitudes of α, η, γ, and $\overline{u}_z$ scale roughly with SN rate as $\sim \sigma^{0.4}$. This table is also appeared in Gressel et al. [2013]

	σ $[\sigma_0]$	α_{xx} $[\mathrm{km\,s^{-1}}]$	α_{yy} $[\mathrm{km\,s^{-1}}]$	γ $[\mathrm{km\,s^{-1}}]$	η_{xx} $[\mathrm{kpc\,km\,s^{-1}}]$
Q	0.25	3.5 ± 0.8 [4.0]	3.8 ± 0.9 [4.5]	9.7 ± 2 [7.6]	1.8 ± 0.5 [1.5]
H	0.50	4.6 ± 1.7 [5.3]	4.9 ± 2.0 [6.6]	12 ± 2 [9.5]	2.5 ± 0.8 [1.9]
F	1.00	6.1 ± 2.0 [7.0]	6.6 ± 3.0 [7.8]	15 ± 4 [13.5]	3.2 ± 1.5 [2.5]
	σ $[\sigma_0]$	η_{yy} $[\mathrm{kpc\,km\,s^{-1}}]$	η_{xy} $[\mathrm{kpc\,km\,s^{-1}}]$	η_{yx} $[\mathrm{kpc\,km\,s^{-1}}]$	$\mathrm{u_z}$ $[\mathrm{km\,s^{-1}}]$
Q	0.25	2.6 ± 0.6 [2.1]	0.3 ± 0.1	-0.2 ± 0.1	14.0 ± 2 [15]
H	0.50	3.3 ± 1.1 [2.7]	0.5 ± 0.2	-0.3 ± 0.2	17.5 ± 4 [18.5]
F	1.00	4.4 ± 1.6 [3.1]	0.5 ± 0.2	-0.4 ± 0.1	22.5 ± 4 [22]

Notes: Bracketed numbers are the values of dynamo coefficients at $z = 1\,\mathrm{kpc}$, obtained after fitting their profiles with odd (or even) Legendre polynomials.

coefficients. All of these profiles remain roughly stationary during the initial kinematic phases of all models but get flattened in the dynamical phase; while subsequently reducing the values of peaks (discussed in Section 5.3.2). We have demonstrated this in Figure 5.1, where the black-solid lines are the profiles of dynamo coefficients during the initial kinematic phase, overplotted with their dynamical phase counterparts indicated by orange-solid lines. These profiles have been averaged over $\sim 100\,\mathrm{Myr}$ (from initial 200 to 300 Myr) to remove the temporal fluctuations and also over five grid points in z direction to get rid of the high wave number contribution. There is a general scaling of dynamo coefficients with SN rate, which can be clearly seen in Figure 5.1. We have documented the values of the peak amplitudes of dynamo coefficients (along with the maximum errors) in Table 5.1, which indicates an approximately identical power law scaling with respect to the SN rate for all dynamo coefficients such that $\alpha/\gamma/\eta \sim \sigma^{0.4}$. In order to get the better statistics, we have averaged these values (Table 5.1) for initial 200 Myr to 300 Myr. We also remark that these scaling laws are in agreement with the previous simulations by Gressel et al. [2008].

5.3.2 Dynamically Significant Fields

While discussing the qualitative picture of galactic dynamo process (first part of this chapter), we explained the amplification of magnetic energy for the prescribed background turbulent flow and tacitly omitted the influence of amplified magnetic field on

the flow. Simple considerations suggest that the back-reaction of magnetic field on turbulence would inhibit the turbulent motions via the Lorentz force and subsequently lead to the damping or the 'quenching' of dynamo coefficients. As a first approximation, it is possible to encapsulate this back-reaction, by expressing the dynamo coefficients α, γ and η as the inverse functions of the strength of mean magnetic field [1] relative to the square-root of turbulent kinetic energy.

5.3.2.1 Magnetic Helicity

A simple justification for such quenching of α coefficients can be given via the τ approximation [Kleeorin et al., 1995; Pouquet et al., 1976]. This, unlike the SOCA approach, relies upon the exact computation of the turbulent EMF, governed by;

$$\frac{\partial \mathcal{E}}{\partial t} = \overline{\frac{\partial \mathrm{u}'}{\partial t} \times \mathrm{b}'} + \overline{\mathrm{u}' \times \frac{\partial \mathrm{b}'}{\partial \mathrm{t}}}\,. \tag{5.11}$$

and $\mathcal{E}$ is further obtained by integrating Equation 5.11, over time as,

$$\mathcal{E} = \overline{\int \frac{\partial \mathrm{u}'}{\partial t} \times \mathrm{b}' \mathrm{dt}} + \overline{\mathrm{u}' \times \int \frac{\partial \mathrm{b}'}{\partial \mathrm{t}} \mathrm{dt}}\,. \tag{5.12}$$

Terms on the right hand side of Equation 5.12 indicate the magnetic and kinetic parts of $\mathcal{E}$ respectively. The regular SOCA approach usually reduces to solving the second term on right hand side of Equation 5.11 (that is, the kinematic term) and omitting the time variation of u'. Therefore, within the realm of SOCA the kinetic term can be expressed as $\alpha_k \overline{\mathbf{B}} + \eta \left(\nabla \times \overline{\mathbf{B}}\right)$, where α_k is the kinematic α, which under the high conductivity limit (and under the assumption of isotropic and homogeneous turbulence) can be written as $\alpha_k = -\tau_c \overline{(\nabla \times \mathbf{u}') \cdot \mathbf{u}'}/3$, where τ_c is the turbulent correlation time. In the presence of strong magnetic field, however, the magnetic part of Equation 5.12 (first term on the right hand side) is also taken into account. This additional term encapsulates the variation of turbulent velocity due to the mean magnetic field. Hence, it can further be written in the form of the 'current helicity', by employing the expression

[1] The diagonal components of α and η tensors, are hereafter referred as just α and η, unless mentioned otherwise.

for Lorentz force, as,

$$\overline{\int \frac{\partial \mathbf{u}'}{\partial t} \times \mathbf{b}' \mathrm{d}t} \;=\; \overline{\int \frac{(\mathbf{j} \times \overline{\mathbf{B}})}{\mu_0 \rho} \times \mathbf{b}' \mathrm{d}t}\,, \tag{5.13}$$

where j is a fluctuating component of current density, which clearly cannot be neglected, when $\overline{\mathbf{B}}$ is strong enough to alter u$'$. μ_0 and ρ are the permeability and local density of ISM. Magnetic part of the EMF can therefore be expressed as;

$$\mathcal{E}_M \;=\; \overline{\int \frac{(\mathbf{j} \times \overline{\mathbf{B}})}{\mu_0 \rho} \times \mathbf{b}' \mathrm{d}t}\,,$$

Assuming isotropy and homogeneity of $\mathbf{b}'$ along with high conductivity, above equation reduces to;

$$\mathcal{E}_M \;=\; \left(\frac{\tau_c}{3\,\mu_0} \overline{\int \frac{\mathbf{j} \cdot \mathbf{b}'}{\rho} \mathrm{d}t} \right) \overline{\mathbf{B}}\,,$$

where τ_c is the typical correlation time. The coefficient $\tau_c \overline{(\mathbf{j} \cdot \mathbf{b}')} / (3\rho\mu_0)$ is a well known helicity effect, which notably has a sign opposite of α_k. This term essentially provides a magnetic back-reaction on the turbulence and is indicated by the notation α_M. The notation of α we use in the previous section thus indicates the total α or $\alpha_k + \alpha_M$.

An obvious question now arises is whether the computed profiles of α (from DNS) also show the aforementioned quenching phenomena? In fact, we do see a substantial flattening of α profiles in a vertical range of $|z| < 1\,\mathrm{kpc}$, during the dynamical phase. This fact is clearly demonstrated in Figure 5.1 [*Panel a*], via the distinction between black-solid lines and red- dotted lines, which represent the profiles of dynamo coefficients during the kinematic and the dynamical phases; respectively. Such flattening could take place via two plausible sources, first one would be the substantial negative feedback from α_M during the dynamical phase, and another one would be the quenching of α_k itself; due to the inhibition of $\mathbf{u}'$ and/or $\nabla \times \mathbf{u}'$. To figure out, which of these processes actually led to the quenching phenomena we observe in the DNS data, we compute the vertical profiles of α_k and α_M for all SN rate models Q, H and F. For that, we use following approximate relations for α in the high conductivity limit and with assumed isotropy

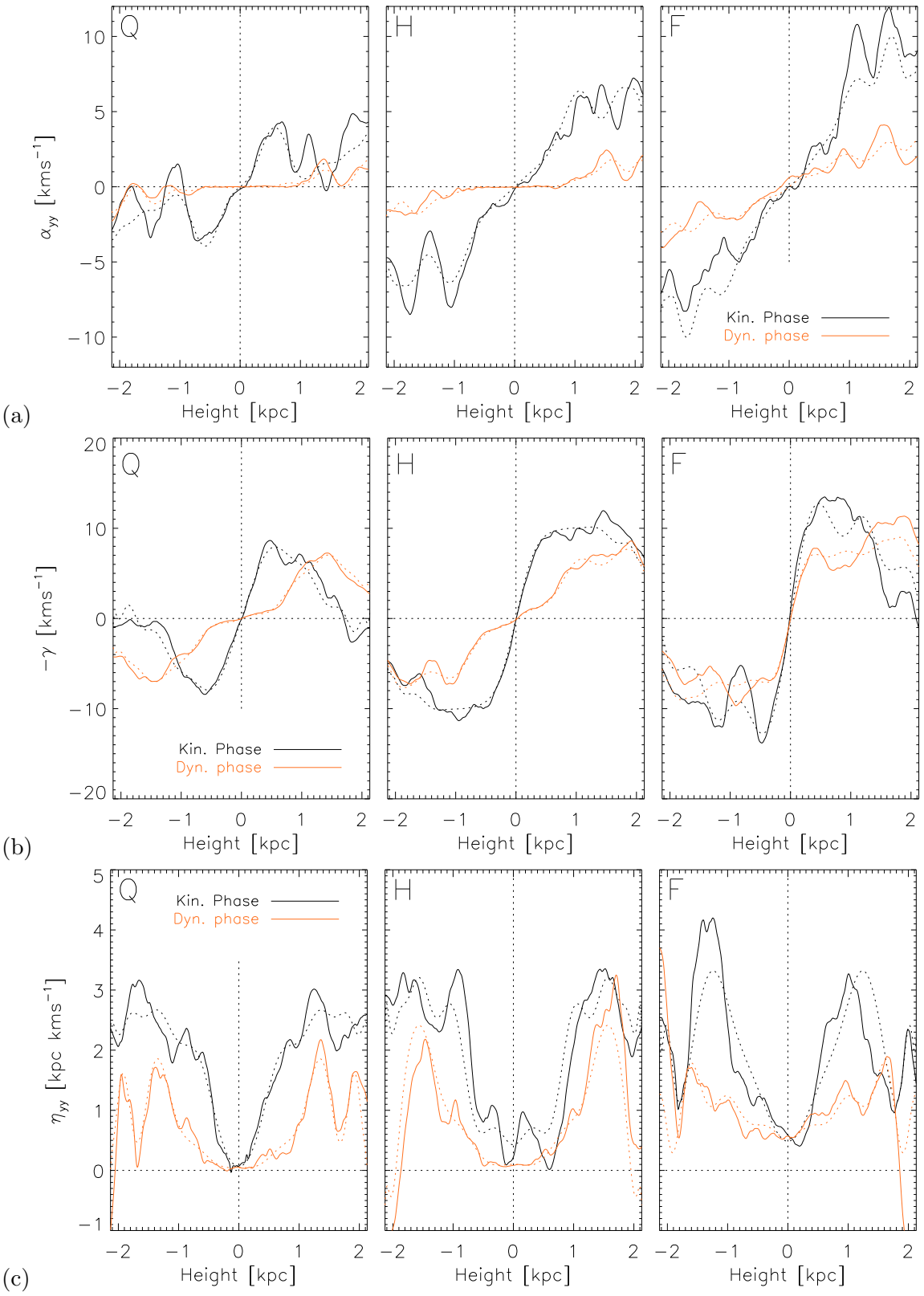

FIGURE 5.1: Vertical profiles of dynamo coefficients α (a), γ (b) and η (c), during the kinematic phase (black-lines) and during the dynamical phase (orange-lines), for models Q, H and F from left to right. Dotted lines indicate the best fit defined by the linear combination of Legendre polynomials.

and homogeneity of ISM turbulence we write, [similar to Pouquet et al., 1976],

$$\alpha_k = -\frac{\tau_c}{3}\overline{(\nabla \times \mathbf{u}') \cdot \mathbf{u}'}, \tag{5.14}$$

$$\alpha_M = \frac{\tau_c}{3\,\rho}\overline{(\mathbf{j} \cdot \mathbf{b}')}. \tag{5.15}$$

where τ_c is the correlation time [2] over which the high conductivity approximation is valid. We estimate the values of τ_c, using the relation $\tau_c \simeq 3\,\eta/\mathrm{u}'^2 \simeq 10\,\mathrm{Myr}$ (owing to the approximation used in Equation 5.5). Since the fluctuating current term '$\mathbf{j}$' can also be represented as $\mathbf{j} = \nabla \times \mathbf{b}'/\mu_0$, α_M can simply be interpreted as the small scale current helicity. Since the applicability of these approximations is in principle restricted to the case of homogeneous and isotropic turbulence, to understand the quenching of α we finally rely upon the DNS test fields data. Nevertheless, the computation of α_M provides a physical insight into the back-reaction of mean magnetic field on turbulent helicity. After estimating the vertical profiles of α_M and α_k, for all SN rates it turns out that during the kinematic phase the total α (derived from the test fields method) is mostly contributed by the α_k. Whereas in the dynamical phase $\alpha_M(z)$ grows to the values comparable to α_k, but with the opposite sign. $\alpha_k(z)$, however, stays relatively unchanged. The profiles of total α, as a result, get substantially quenched. Hence the quenching of α observed in DNS seems to be, mainly a result of the back-reaction of small scale current helicity. In Figure 5.2, for example, we have shown the space-time contour plots of α_M *[Panel-top]*, α_k *[Panel-center]* and α_{yy} *[Panel-bottom]*, [3] for model Q, where the aforementioned characteristics of α_M, α_k and α are clearly represented. Similar contours for models H and F are included in Appendix D.

5.3.2.2 Turbulent Diffusivity Quenching

Similar to α coefficients the vertical profiles of turbulent diffusivity, $\eta(z)$, are also flattened during the dynamical phase, within the vertical range of $-1\,\mathrm{kpc} < \mathrm{z} < +1\,\mathrm{kpc}$. The distinction between its unquenched and quenched profiles is represented by black-solid lines and red-dotted lines in Figure 5.1. Initial vertical profiles of η approximately

[2] Here it should be noted that the times τ involved in Equation 5.15 may not, as a general rule, be exactly equal to the turbulent correlation time τ_c, its only a plausible assumption. These times may not even be equal for α and η [Rädler & Rheinhardt, 2007].

[3] α_{yy} is calculated via the test field method

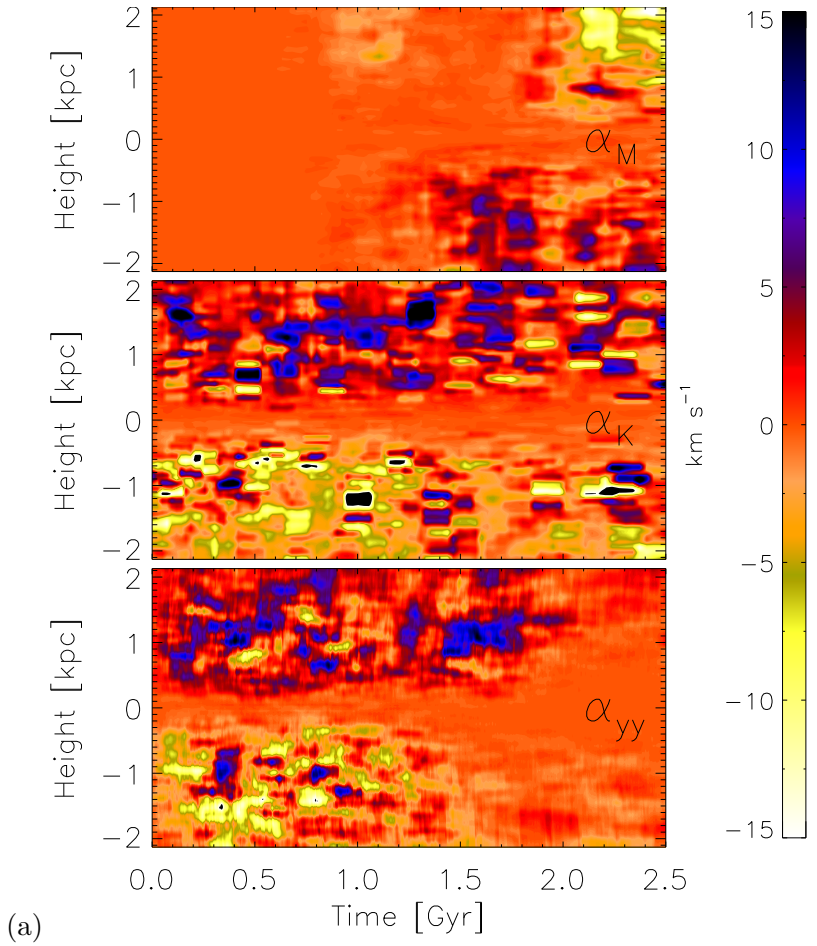

FIGURE 5.2: *Panel-top*: Time evolution of $\alpha_M(z)$ profile for model Q *Panel-top*: Time evolution of $\alpha_k(z)$ profile for model Q. *Panel-bottom*: Time evolution of $\alpha_{yy}(z)$ profile for model Q. All contours have a same color scale defined by the color-bar on right side. Typical magnitude of α_M grows to the values comparable to the kinematic values of α_{yy} except for the opposite sign, while the α_k remains unchanged. We therefore see a subsequent dampening of α_{yy} profiles during the dynamical phase (after ~ 1.5 Gyr).

follow the estimates obtained using the SOCA (Equation 5.5) for all SN rates. In Figure 5.3 we have compared the z profiles of η obtained from DNS (red-solid lines) with kinetic η profiles obtained from Equation 5.5 (black-dashed lines). Used value of the correlation time τ_c is approximately 10 Myr (same as is used to calculate α_M). Rough agreement between the both suggests the validity of SOCA during the kinematic phase. Moreover the quenched profiles of η also follow the SOCA approximation except with the slightly reduced values of τ_c (also shown in the upper panels of Figure 5.3).

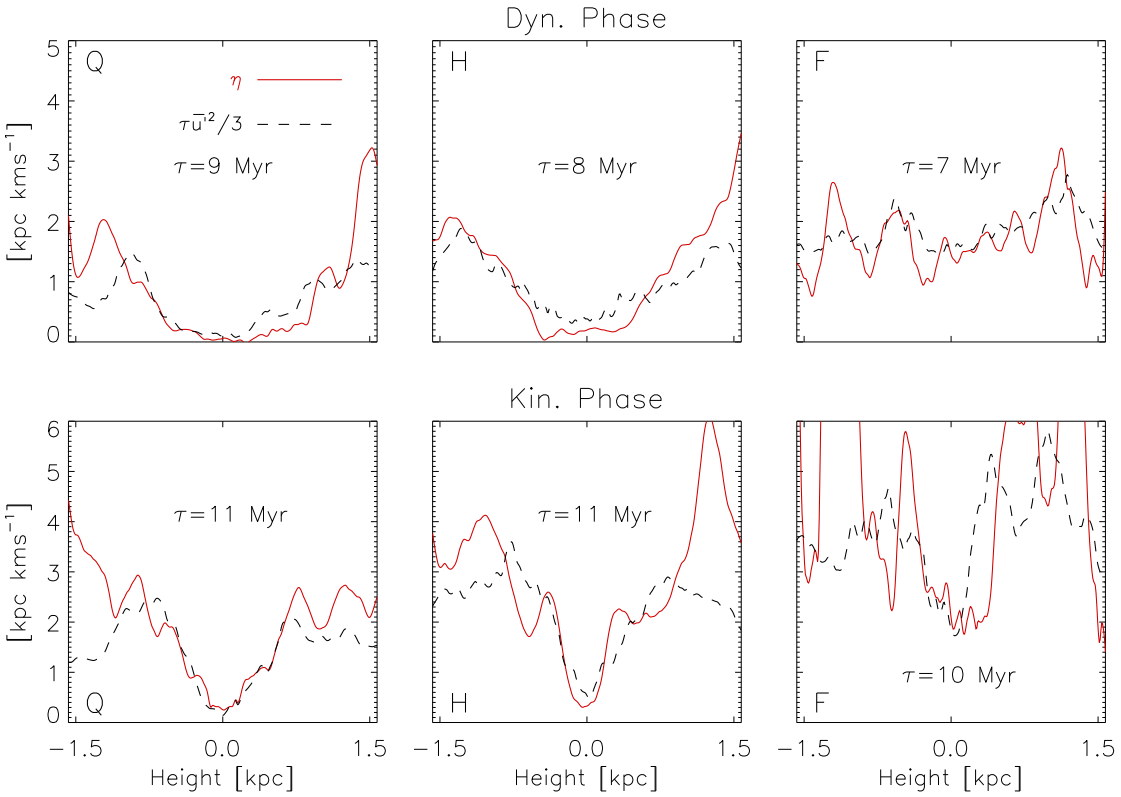

FIGURE 5.3: Vertical profiles of η coefficient (calculated via test fields method) are shown in red-solid lines, overplotted with the corresponding SOCA estimates, $\tau_c\,\overline{\mathrm{u}}'^2/3$ given by Equation 5.5, shown in black-dashed lines, where the $\mathrm{u}'(\mathrm{z})$ profiles are extracted from DNS data at the same time. Three panels in the Bottom represent the vertical profiles during the kinematic phases of models Q, H and F; from left to right. Upper three panels represent the same during dynamical phase. The correlation time τ_c turns out to be $\sim 10\,\mathrm{Myr}$ for all SN rates during the kinematic phase and remains nearly same in the dynamical phase, suggesting that the observed quenching of η takes place mainly via the quenching of turbulence intensity u'^2.

To quantitatively express the quenching of dynamo coefficients, we express them as a function of relative strengths of mean field, which we define by the ratio β;

$$\beta = \frac{\left(\overline{B}_x^2 + \overline{B}_y^2\right)^{1/2}}{\sqrt{\mu_0 \rho\, u'^2}}\,, \tag{5.16}$$

that is; the square-root of the ratio of mean magnetic energy and kinetic energy. Value of β approaching to one, corresponds to the situation of dynamically important mean fields. Since the vertical profiles of the turbulent kinetic energy and mean magnetic energy are approximately Gaussian in shape, $\beta\,(z)$ also evolves to a same functional form during the dynamical phase. Final values of β for models Q and H, in the mid-plane are 2 to 4 times greater than in the halo, and for the model F, the final $\beta\,(z)$ profile is roughly constant e.g. Figure 5.4.

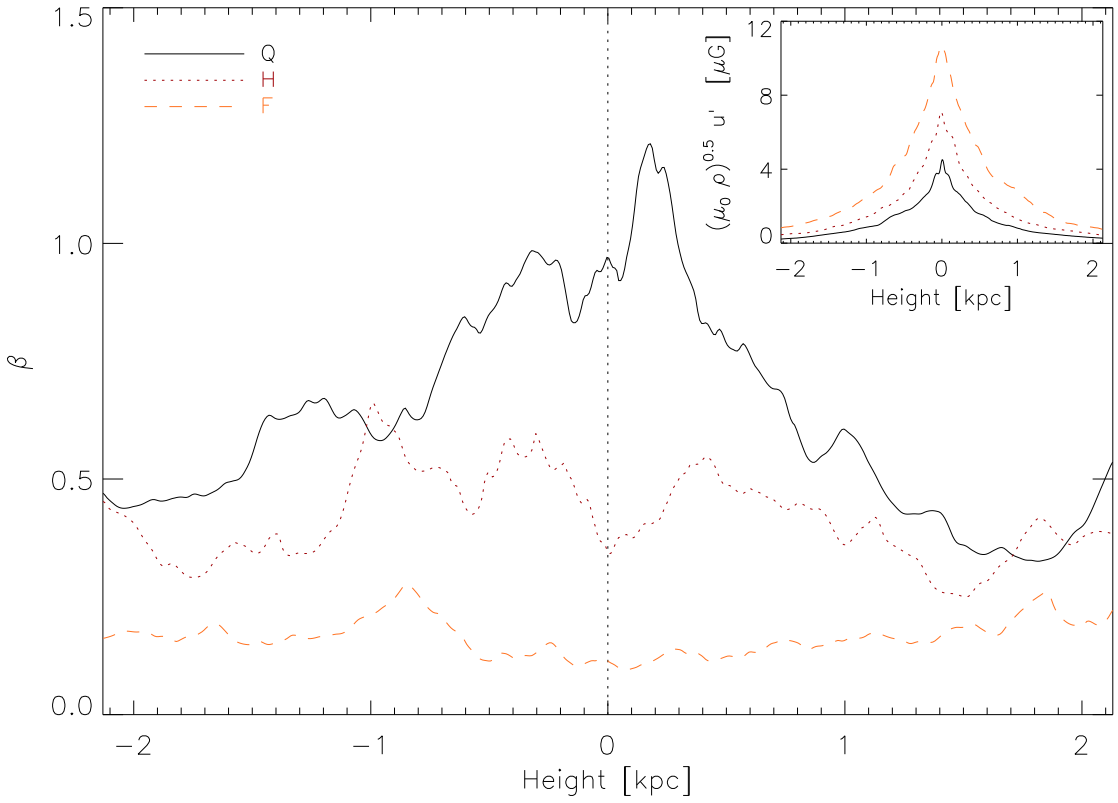

FIGURE 5.4: Vertical profiles of β during the dynamical phase, for model Q (black-line), model H (red-line) and model F (green-line). Inner plot shows the vertical profiles of equipartition fields ($\sqrt{\mu_0\rho}\,u'$)

To derive the dependence of the dynamo coefficients on relative mean field strength, we fit the DNS values of α, η and γ to the algebraic functions similar to Ivanova & Ruzmaikin [1977]; Raedler et al. [1990], such that;

$$\xi(\beta) \;=\; \frac{\xi_0}{1 + a\,\beta^b}\,, \tag{5.17}$$

with two free parameters a and b. The notation $\xi(\beta)$ represents the dynamo coefficients α, η or γ. To obtain the best fits for $\alpha(\beta)$ we consider the inner domain of approximately $|z| < 1.2\,\mathrm{kpc}$, within which the profiles are roughly regular and linear. We then calculate the slopes of these profiles and plot the maximum amplitudes, above and below the mid-plane, (smoothed over $\sim 50\,\mathrm{pc}$) as a function of corresponding β. The fitting parameters for α are $b = 2$ (with maximum error of $\sim 10\%$), and $a = 27$ (with maximum error of $\sim 40\%$), which are independent of SN rates. Large values of a in the context of dynamical quenching would indicate the catastrophic quenching, if a scaled with the magnetic Raynolds number R_m. By using the standard definition of $R_m = L^2\Omega/\eta$ (η

here is the macroscopic diffusivity) we have $R_m \simeq 10000$ on the box scale (for $L \simeq 4\,\mathrm{kpc}$), which is larger than the obtained values of a. If we define the Raynolds number based on the turbulent length scales, that is, $R_m \simeq \mathrm{u'l_0}/\eta$ and get $R_m \simeq 75 - 200$, which is still larger than the value of a.

To obtain the β dependence of γ term we use the similar method, but here we consider the inner domain of $|z| < 0.5\,\mathrm{kpc}$, since the γ profiles are concentrated only in the inner disc part. Obtained fitting parameters are $a = 10$ (with maximum errors of 20%) and $b = 2$ (with maximum error of 25%), these are also roughly independent of the SN rate.

Unlike the α and γ profiles, $\eta(z)$ is roughly quadratic within the vertical range of $|z| < 1\,\mathrm{kpc}$. Hence to obtain the best fits, we restrict within that vertical range and plot the maximum amplitudes of $\eta(z)$ profiles as a function of β. Obtained values of best fitting parameters are $a = 6$ (maximum error of 20%) and $b = 1$ (maximum error 10%), these remain fairly independence of the SN rate.

The quenching relations for α, η and γ, for all SN rates can be summarized as, $\alpha = \frac{\alpha_k}{1+27\,\beta^2}$, $\eta = \frac{\eta_k}{1+6\,\beta}$ and $\gamma = \frac{\gamma_k}{1+10\,\beta^2}$, where α_k, η_k and γ_k are initial *unquenched* amplitudes of the dynamo coefficients during the kinematic phase ($\beta << 1$), which depend only on the SN rate. In Figure 5.5 we have shown these β dependencies for all SN rates. Using the SN rate independence of the quenching functions, we further replace the kinematic amplitudes (α_k, η_k and γ_k) by SN scaling laws obtained in Table 5.1, and finally get;

$$\begin{aligned} \alpha &= \frac{\alpha_0}{1+27\,\beta^2}\,(\sigma/\sigma_0)^{0.4}\,, \\ \eta &= \frac{\eta_0}{1+6\,\beta}\,(\sigma/\sigma_0)^{0.4}\,, \\ \gamma &= \frac{\gamma_0}{1+10\,\beta^2}\,(\sigma/\sigma_0)^{0.4}\,, \end{aligned} \tag{5.18}$$

α_0, η_0 and γ_0 represent the kinematic amplitudes of dynamo coefficients, for the SN rate $\sigma = \sigma_0$, (that is, for model F).

5.3.3 Quenching of the Wind

Similar to the dynamo coefficients, the mean vertical wind profiles $\overline{\mathrm{u_z}}$, also get affected by the strong mean fields within the vertical range of $|z| < 1\,\mathrm{kpc}$. This difference can be

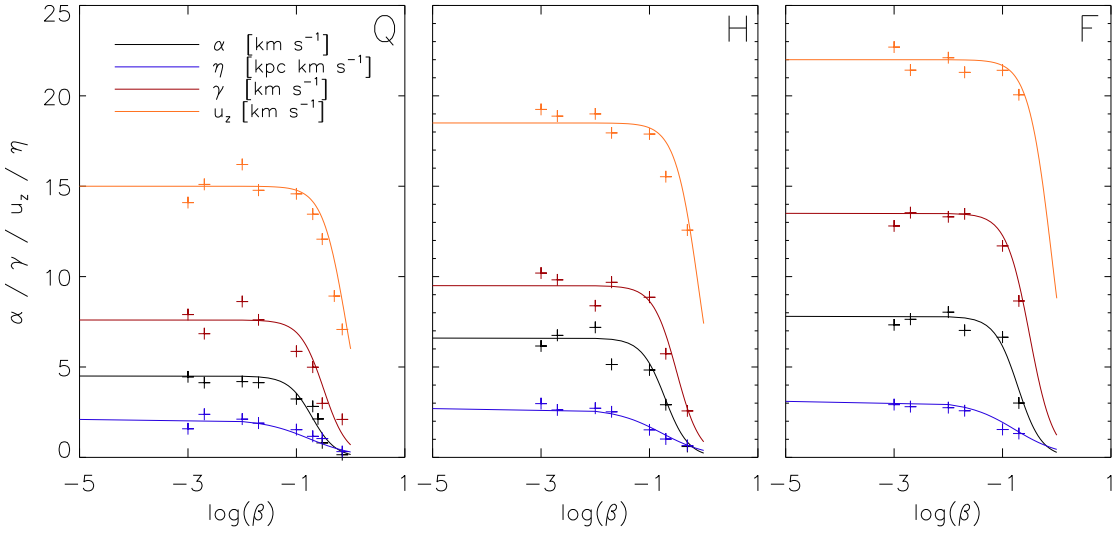

FIGURE 5.5: Dependence of dynamo coefficients, α (black-lines), η (blue-lines), γ (red-lines), and $\overline{u}_z$ (orange-lines) on β, for models Q, H and F (from left to right), computed at $z = \pm 1\,\mathrm{kpc}$. Estimated errors in these fits are $\sim 20\%$ (Maximum).

seen in Figure 5.6, where the black-solid lines represent $\overline{u}_z\,(z)$ profiles, in the kinematic phase, while the dotted-red lines represent the same during the dynamical phase. To obtain the dependence of $\overline{u}_z$ as a function of β we consider roughly linear profiles within the vertical range of approximately $|z| < 1\,\mathrm{kpc}$, and plot maximum amplitudes as the functions of β. Resulting curves are then fitted with Equation 5.17, and the parameters for the best fit turn out to be $a = 1.5$ (with maximum error of 30%) and $b = 2$ (with maximum error of 10%), these are also almost independent of the SN rate. We further replace the kinematic values of $\mathrm{u_z}$ by the corresponding SN scaling law (Table 5.1) and finally get;

$$\overline{u}_z = \frac{\overline{u}_0}{1 + 1.5\,\beta^2}\,(\sigma/\sigma_0)^{0.4}\,, \tag{5.19}$$

where $\overline{u}_0$ is the unquenched amplitude of $\overline{u}_z$ for $\sigma = \sigma_0$. This behavior of $\overline{u}_z$ is shown in Figure 5.6 for all SN rates, where the plus (+) signs represent the average values of $|\overline{u}_z|$ at $z = \pm 1\,\mathrm{kpc}$ for the corresponding β and the solid line indicates the best fit. It is to be noted that the quenching of $\overline{u}_z$ is significantly weaker compared to the other dynamo coefficients (see the multipliers of β in Equation 5.18 and Equation 5.19).

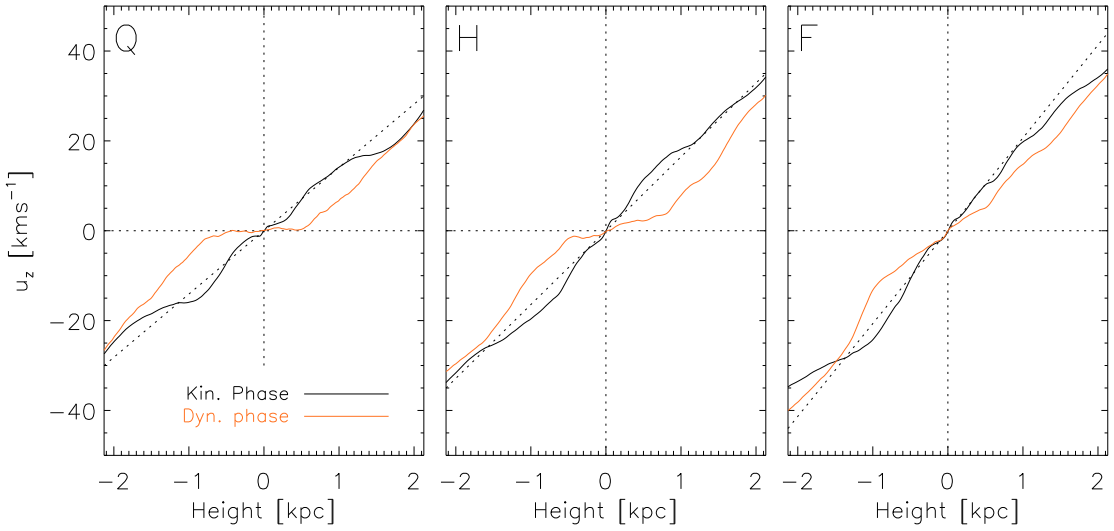

FIGURE 5.6: Same as Figure 5.1, but for the vertical wind, u_z profiles.

5.4 1D Dynamo Model

In light of the prior discussion we argue that the amplification and saturation of E_m seen in DNS, is an outcome of $\alpha\Omega$ dynamo process along with the quenching mechanism for dynamo coefficients. To justify this argument, we write the one-dimensional $\alpha\Omega$ dynamo model equivalent to the DNS box model. For that we decompose the flow variables as a sum of their mean and fluctuating (turbulent) component, the 'mean' here is defined as average over the horizontal $x-y$ planes, this choice leaves 'z' as the only independent variable. The induction equation for the mean field in its component form can then be written as;

$$\begin{aligned}
\frac{\partial \overline{B}_x}{\partial t} &= \frac{\partial}{\partial z}\left(-\left(\overline{u}_z+\gamma\right)\overline{B}_x - \alpha_{yy}\,\overline{B}_y + \eta_{yy}\,\frac{\partial \overline{B}_x}{\partial z}\right), \\
\frac{\partial \overline{B}_y}{\partial t} &= \frac{\partial}{\partial z}\left(-\left(\overline{u}_z+\gamma\right)\overline{B}_y + \alpha_{xx}\,\overline{B}_x + \eta_{xx}\,\frac{\partial \overline{B}_y}{\partial z}\right) + q\,\Omega \overline{B}_x\,, \\
\frac{\partial \overline{B}_z}{\partial t} &= 0\,,
\end{aligned} \tag{5.20}$$

the last equation arises from the solenoidity constraint. For the sake of simplicity we have neglected the comparatively small contribution of off-diagonal η terms (these are about 1-2 orders of magnitude smaller than the diagonal terms). Mean velocity field in

this case; has only two components, one of which is a predefined azimuthal component ($x\,\Omega$), and the other one is the SN dependent outward winds ($\overline{u}_z$).

5.4.1 Evolution of 1D Model

The system of Equation 5.20 is solved by the finite difference method on a staggered grid, over the range of $|z| < 2.133$ kpc. Which is resolved with 512 grid points (similar to DNS). Initial and boundary conditions for this are as described below. Initial $\overline{B}_x(z)$ and $\overline{B}_y(z)$ profiles are chosen directly from the DNS data to have a maximum similarity with DNS. We moreover smooth this initial data over first 50 to 100 Myr to have a sufficiently equal mix of vertical modes and to reduce the stochastic disturbances. Initial 50 Myr are excluded to get rid of the impact of the large scale initial mode. We use the gradient boundary conditions for $\overline{\mathbf{B}}$ consistent with the DNS boundary conditions. Ω is set to 100 Gyr^{-1}, similar to the prescribed rotation profile of the DNS models. Vertical profiles of α, γ and η are computed during the evolution itself, using Equation 5.18, while their initial unquenched amplitudes (α_0, γ_0 and η_0) are extracted from the test fields data (of model F). We average these profiles for initial 100 to 400 Myr of DNS evolution (which is well within the unquenched regime, e.g. Figure 5.5), to remove the noise in the outer halo data. Whereas, the high wave numbered noise corresponding to the inner disc is removed by fitting these profiles with a linear combination of 15 odd (and even) Legendre polynomials, $P_n\,(z)$. Similarly $\overline{u}_z(z)$ profiles are also computed during the evolution by solving Equation 5.19 and the unquenched $\mathrm{u}_0(\mathrm{z})$ profiles are obtained by averaging the DNS values over initial 100 Myr to 400 Myr (of model F), these profiles are best fitted with only linear function of z (first order Legendre Polynomial). Effect of changing the SN rate is modeled with the scaling law $\sigma^{0.4}$ embedded in Equation 5.18 and Equation 5.19. Evolution of dynamo coefficients and the wind profiles clearly, depend on the $\beta(z)$, which is computed from Equation 5.16, during the evolution of 1D model. Constant vertical profile of $\sqrt{\rho}u'$ for the β computation is predefined for each SN rate, which is also extracted from the DNS data (Figure 5.4 inset).

5.5 Comparison of Mean Field and Direct Simulations

Using the 1D mean field dynamo model (with algebraically quenching of the dynamo coefficients) we ware able to reproduce the results of 3D DNS with a remarkable similarity, which we discuss in this section. For simplicity we choose the same notations- Q, H and F for the mean field models as well (depending on the SN rate).

Total magnetic energy in all mean field models grows exponentially with an e-folding time of $\sim 100\,\mathrm{Myr}$, for almost a Gyr. After which it keeps growing only with negligible growth rates for mean field models Q and H and saturates for F. This behavior is very much similar to what we see in DNS. In Figure 5.7 we compare the evolution of total magnetic energy, in DNS models (black-solid lines) with the mean field models (red-dotted lines). We point out the remarkable agreement between these curves, during the kinematic and dynamical phase. Similarly the vertical profiles of $\overline{B}_x$ and $\overline{B}_y$ also show a significant agreement with DNS results, along with the intermediate field reversals and parity changes (as shown in Figure 5.7 [*Panel-left*]). The final 'S' modes of $\overline{B}_y(z)$ in the dynamical phases of all 1D models have comparable scale-heights with DNS, in the outer halo. While in the inner disc, the profiles of mean field dynamo solutions are comparatively narrower, as shown in Figure 5.8 for all SN rates [also see Bendre et al., 2015].

Apart from the ability to reproduce the DNS outcomes; the mean field dynamo formulation also explains the reason for the distinctive behavior of magnetic field in the kinematic and dynamical phases, as follows. During the initial kinematic phase, the transport term in Equation 5.20, $\overline{u}_z + \gamma$, remains negligible in the inner disc ($|z| < 1.1\,\mathrm{kpc}$), for all models. This is because the wind and pumping profiles tend to cancel each other (e.g. Figure 5.1 and Figure 5.6). Magnetic energy under such conditions amplifies exponentially, similar to the solution of $\alpha\Omega$ dynamo and the growth time (normalized with the diffusion time) depends upon the dynamo number (Section 5.6).

Later during the dynamical phase, the profiles of $\overline{u}_z$ and γ quench with different rates and the residual transport term ($\overline{u}_z + \gamma$) starts contributing to the evolution. Since the actual contribution of this term to the dynamo depends on the rate of SN explosions we see the different dynamical behaviors in different SN models. This term encapsulates the residual advective transfer of the magnetic flux and has a crucial roll in the saturation

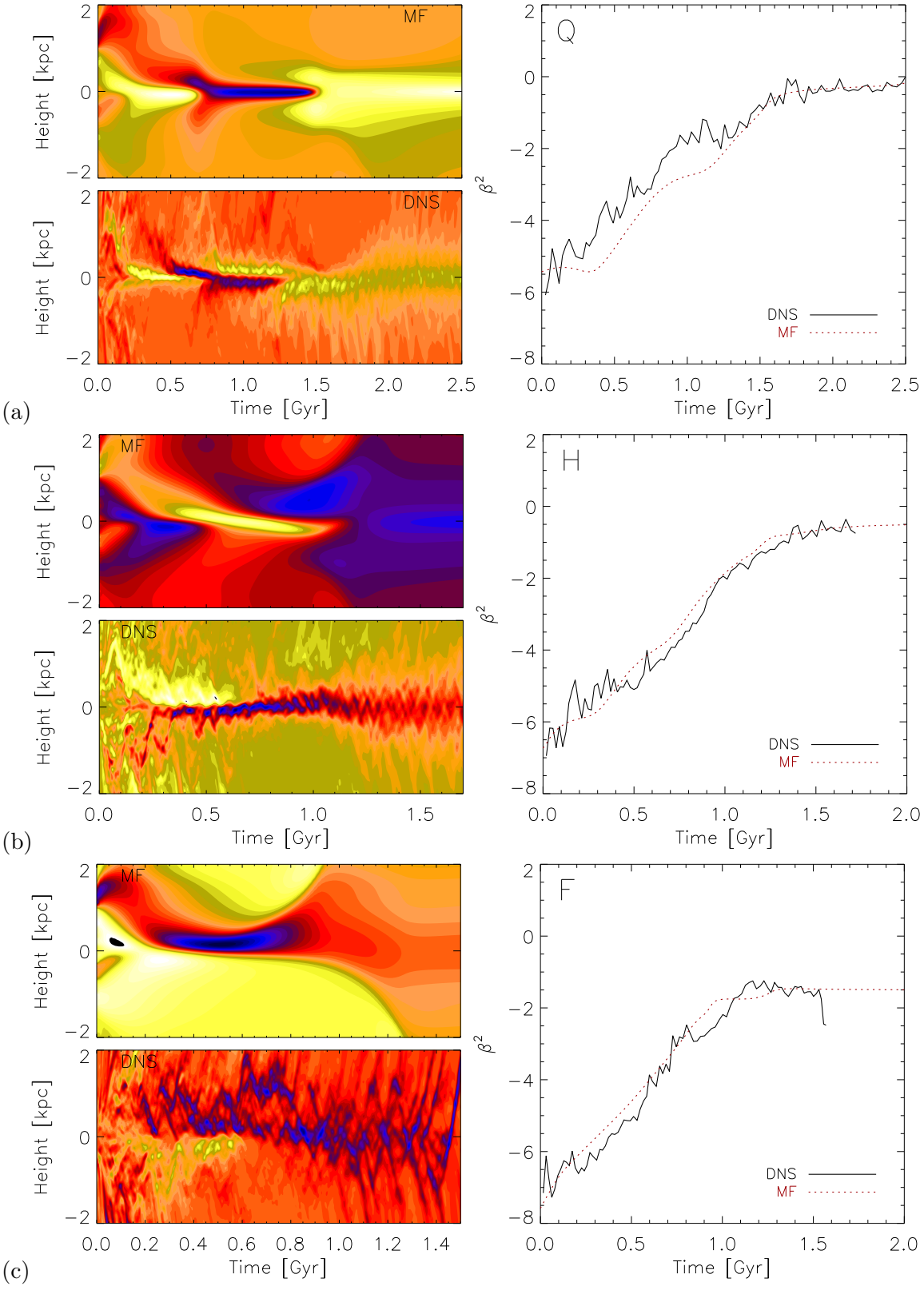

FIGURE 5.7: Left panels show the comparison between space-time profiles of $\bar{B}_y$, obtained from direct numerical simulations (*Panel down*) and from the mean field simulations (*Panel up*). Right panels show the comparison between evolution of β^2 (relative mean field energy) obtained from direct numerical simulations (black-solid lines) and from the mean field simulations (red-dotted lines). Computed for model Q (*Panel a*), model H (*Panel b*) and model F (*Panel c*).

of dynamo. The non-vanishing growth of mean magnetic energy during the dynamical phases of model Q and H, exists simply due to the simultaneous quenching α and η that preserves the dynamo number but leads to the slowly growing solution because of the elongated diffusion time scale (Section 5.6). The transport term in this case has only a negligible roll. Whereas for model F, this term becomes significantly larger, already for the comparatively smaller β values. This strong advection of magnetic flux out of the dynamo active region leads to the saturation of magnetic energy in model F. To prove that the non-vanishing transport term is solely responsible for the saturation, we switch it off in 1D model and get the sustained growth rate of magnetic energy even in the dynamical phase of model F.

Pointing out further similarities in the mean field and direct simulations, we note that the pitch angles of mean magnetic field as seen in the 1D models also match with the DNS results. Which is to say that the significant values of pitch angles are seen only in model F, where the saturation occurs due to the presence of outward wind. While the mere quenching of α and η (similar to model Q and H) leads to the strong reduction of pitch angles during the dynamical phase, which is contrary to the observations [Van Eck et al., 2015].

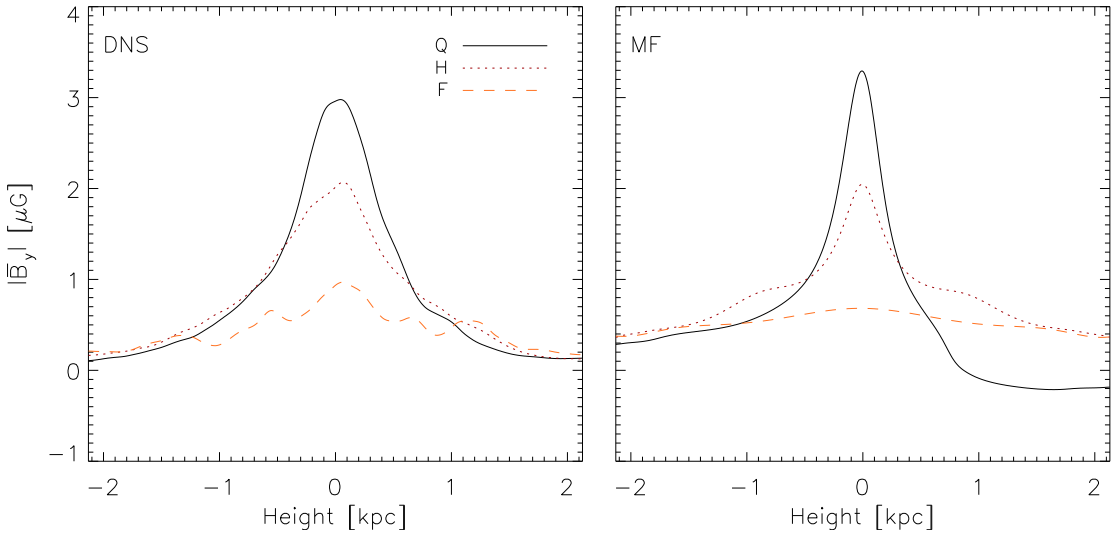

FIGURE 5.8: Vertical profiles of $\overline{B}_y$, during the dynamical phase, from DNS (*left-panel*), and from the mean-field simulations (*right-panel*).

5.6 Analytical Assessment

As far as the global results are concerned, we have pointed out the qualitative similarities between direct and mean field simulations. In this section we analytically justify the kinematic amplification of E_m in terms of dynamo number. We further prove that the sustained growth of E_m during the dynamical phase (of models Q and H) is a consequence of the prolonged turbulent diffusion time t_d, corresponding to the quenched dynamo coefficients. But before doing that, we will first briefly discuss the $\alpha\Omega$ approximation and point out that our mean field models, during the kinematic phase, can be sufficiently described as $\alpha\Omega$ dynamo.

5.6.1 Alpha-Omega Approximation

Dynamo equations (Equation 5.4), with certain justifiable prerequisites, are analytically solvable and are referred to, as the $\alpha\Omega$ dynamo. Conditions under which the $\alpha\Omega$ approximation is valid, are as follows,

1) Non-diffusive transport of the magnetic flux should be negligible compared to contribution of α and diffusion term. This condition is certainly satisfied for our models during the initial kinematic phase, where $\overline{u}_z$ and γ cancel each other within a vertical range $|z| < 1\,\mathrm{kpc}$ (as represented in Figure 5.1 [*Panel c*] and Figure 5.6).

2) The gradient of turbulent η should be negligible compared to the gradient of mean fields (so that it can be taken out of the derivative term $\nabla \times \eta\nabla \times \overline{\mathbf{B}}$). This is also approximately valid within $|z| < 1\,\mathrm{kpc}$ of our mean field models, considering the scale-heights of $\eta(z)$ profiles ($\sim 1\,\mathrm{kpc}$), which are comparatively larger than the mean field scale heights (few 100 pc). (as represented in Figure 5.1 [*Panel b*] and Figure 3.4).

3) The differential rotation term should be the dominant one, so that the helical contribution to the mean poloidal field ($\partial(\alpha_{xx}\overline{B}_x)/\partial z$) can be safely omitted.

Using these constraints in Equation 5.20; we further normalize the coordinate z using a typical vertical length scale H and time t with the diffusion time scale $t_d = H^2/\eta$ ($t = t'\,t_d$ and $z = z'H$) and write;

$$\begin{aligned} \frac{\partial \overline{B}_x}{\partial t'} &= -C_{\alpha'} \frac{\partial \alpha\, \overline{B}_y}{\partial z'} + \frac{\partial^2 \overline{B}_x}{\partial z'^2} \\ \frac{\partial \overline{B}_y}{\partial t'} &= -C_\Omega\, \overline{B}_x + \frac{\partial^2 \overline{B}_y}{\partial z'^2} \end{aligned} \quad , \tag{5.21}$$

where α is normalized by its kinematic amplitude α_0 and the expressions for dynamo parameters are $C_\alpha = \alpha\, H/\eta$ and $C_\Omega = H^2\, q\Omega/\eta$. With an assumption of the separability of variables; above system allows the solutions in the form of expansion of free-decay modes (${B_j}^i$), particularly;

$$\overline{B}_j \simeq exp\left(A\, t'\right) \sum_{i=0}^{\infty} c_i {B_j}^i \,, \tag{5.22}$$

where the index j represents the vector coordinate $\{x, y\}$, and $\mathbf{B}^i$ represents a set of eigenvectors of the solution space of Equation 5.21, in the absence of helical and rotational terms (C_α and C_Ω respectively). Perturbation analysis of the system [e.g. Shukurov, 2004; Shukurov & Sokoloff, 2007], using the basis formed by $\mathbf{B}^i$, further revels that the growth rate 'A' of the dominant mode; can be approximated by a function of dynamo number $D = C_\alpha C_\Omega$, as;

$$A \simeq \frac{1}{t_d}\left(\sqrt{D} - \sqrt{D_c}\right) . \tag{5.23}$$

Constant D_c is the critical dynamo number, such that; for $D < D_c$, $\alpha\Omega$ dynamo does not have a growing solution. Similar expression for 'A' can also be derived via a so called no-z approximation by Mestel & Subramanian [1991]; Subramanian & Mestel [1993]. We use this solution to explain the kinematic growth of mean field in the next subsection.

5.6.2 The Case of 'Zero'D Model

The time at which the kinematic phase ends; can be derived by employing the conditions of the validity of $\alpha\Omega$ dynamo and it proceeds as follows. Using the definition of dynamo number we can write;

$$D = C_\alpha \, C_\Omega = \frac{\alpha \, H^3 \, q \, \Omega}{\eta^2} \, . \tag{5.24}$$

Using the quenching laws for α and η, we express Equation 5.24 as a function of β and SN rate, as;

$$D = D_0 \left(\frac{\sigma}{\sigma_0} \right)^{0.4} \frac{(1+6\beta)^2}{1+27\beta^2} \, , \tag{5.25}$$

where $D_0 = \alpha_0 \, H^3 \, q \, \Omega / {\eta_0}^2$, is the unquenched initial amplitude of dynamo number. By assuming $\overline{u}_z \simeq \gamma$ (consistent with the initial kinematic phase) the approximate solution for $\alpha\Omega$ dynamo (Equation 5.22) [e.g. Shukurov, 2004] can be expressed as;

$$\overline{B(t)} \;\; = \;\; \overline{B_0} \, exp \left(\frac{t}{t_d} \left(\sqrt{D} - \sqrt{D_c} \right) \right) \, , \tag{5.26}$$

here we have neglected the 'space part' of the argument, hence we refer it as a zero-D solution. The physical time t in Equation 5.26 is expressed in the units of diffusion time $t_d = H^2/\eta = (\sigma/\sigma_0)^{0.4} H^2 \, (1+6\beta)/\eta_0$. Now by using Equation 5.25 in Equation 5.26 along with the definition of diffusion time and quenching laws (Equation 5.18), we can write,

$$\overline{B(t)} \;\; = \;\; \overline{B_0} \, exp \left(\frac{\eta_0 \, t}{H^2} \left(\sqrt{\frac{D_0 \, (\sigma/\sigma_0)^{-0.4}}{(1+27\beta^2)}} - \sqrt{\frac{D_c \, (\sigma/\sigma_0)^{-0.8}}{(1+6\beta)^2}} \right) \right) \, . \tag{5.27}$$

This relation gives an approximate evolution equation of the mean fields in $\alpha\Omega$ dynamo; with algebraically quenching coefficients.

Now, to plot the time evolution of β^2 from Equation 5.27, we choose the value of $\overline{B_0}$ such that the ratio $\overline{B(t)}/\overline{B_0}$ at $t = 0$ coincides with the initial value of β in DNS. To have a justifiable comparison with DNS; the values for other parameters (H and η_0) are also chosen form DNS data, which are, $H \simeq 1\,\mathrm{kpc}$ (thickness of the inner disc and the

approximate range over which the transport term is nearly zero) and $\eta_0 \simeq 2\,\mathrm{kpc\,km\,s^{-1}}$ (which is the unquenched turbulent diffusivity in model F averaged over the vertical range H). Values for the critical dynamo number D_c is derived numerically by evolving our 1D model.

In Figure 5.9 we have plotted the evolution of β^2 using the zero-D solution. It shows the exponential amplification of β^2 for almost a Gyr with the growth time of $\sim 100\,\mathrm{Myr}$, for all SN rates. This matches with the kinematic growth of mean field models (and DNS). During the dynamical phase, the prescribed quenching relation (for α and η) does not quench the dynamo number D, below the critical dynamo number D_c for any SN rate. Magnetic energy, therefore, keeps growing with the reduced growth rate even in the dynamical phase of model F and the damped values of α and η in the dynamical phase account for the slow amplification of β^2. Or in the other words the dynamical amplification takes place in the units of prolonged diffusion times $t_d = (\sigma/\sigma_0)^{0.4} H^2\,(1+6\beta)/\eta_0$. The analytical model Q (orange-solid line), however, roughly mimics the entire evolution curve of β^2 from DNS, indicating the minimal contribution of wind for the low SN rate. The sustained growth of β^2, for model F (in zero D case) proves that the complete saturation of dynamo cannot achieved without the contribution of wind term even if the α and η profiles are quenched according to Equation 5.18.

To obtain the analytical expression for the evolution of total magnetic energy E_m we use the relation between turbulent and mean magnetic field as a function of σ (Equation 3.4), and write the total magnetic energy as a sum of magnetic energies from the mean and turbulent field components. We finally get

$$\overline{E_m(t)} = E_0\,\left(1+13.7\sigma^{0.6}\right)\,exp\left(\frac{2\,\eta_0\,t}{H^2}\,\left(\sqrt{\frac{D_0\,\sigma^{-0.4}}{(1+27\beta^2)}}-\sqrt{\frac{D_c\,\sigma^{-0.8}}{(1+6\beta)^2}}\right)\right)\,. \tag{5.28}$$

This relation is valid in the kinematic phases of all models, that is; where the Equation 3.4 is valid. By substituting the appropriate values of β, t and E_0 we get the SN scaling law for magnetic energy at the end of kinematic phase ($E_m \sim 1+13.7\sigma^{0.6}$). This scaling relation roughly estimates the final kinematic values of E_m in DNS, which are listed in Table 3.4.

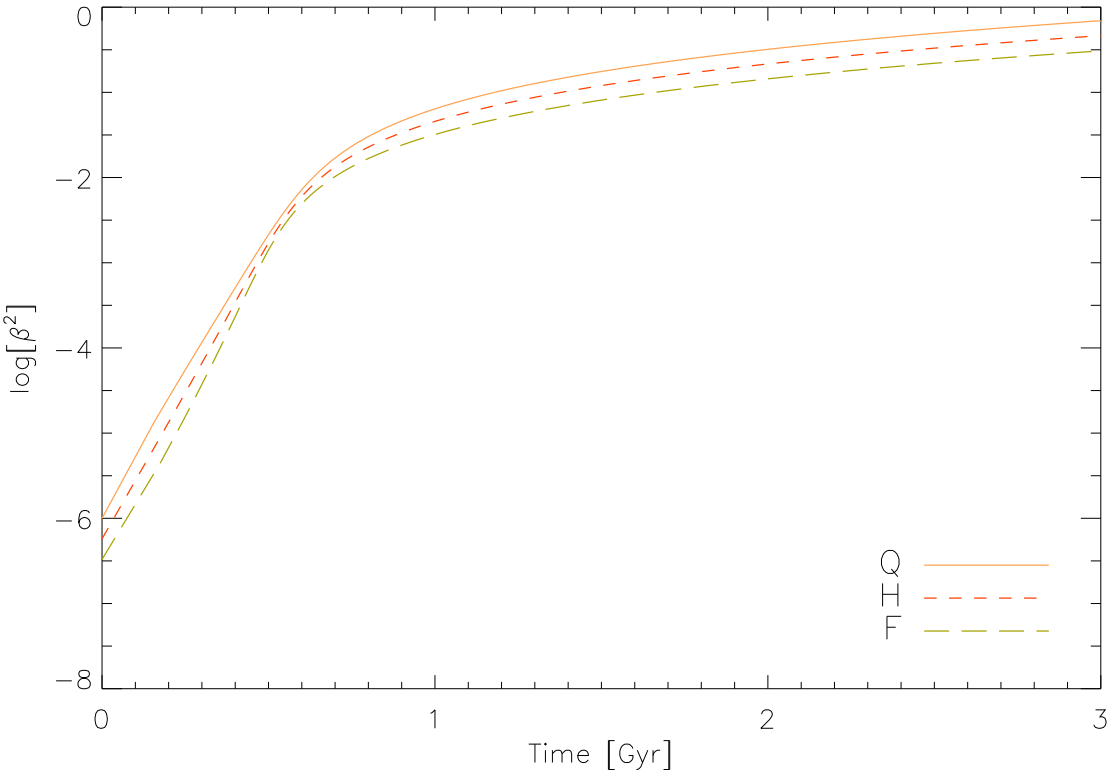

FIGURE 5.9: Evolution of β^2 using the analytical approximation Equation 5.27 where the ratio of $D_0/D_c = 3.5$ and the initial values of β are chosen from the DNS data.

5.6.3 Disc and Halo Distinctions

As Figure 5.7 [*Panel-right*] indicate, the magnetic energy (from mean fields) does not exceed the turbulent kinetic energy until 2.5 Gyr for any SN rate. While the DNS results suggest that; within the inner disc of $z < 0.5$ kpc it is possible to get the β values larger than '1' for the model Q (see e.g. Table C.1). In order to explain this, we again plot the time evolution of β^2 (for all SN rates) using the zero-D solution Equation 5.27; restricted to the inner disc part (using $H = 0.5$ kpc), as shown in Figure 5.10 [*Panel b*]. It should be noted that the final values of β, with this restriction exceed unity for models Q and H. Also they amplify with a faster growth rate (e-folding time $\sim$ 70 Myr) during the kinematic phases of all SN rate models.

To check the consistency of this hypothesis, we evolve the 1D dynamo equations (Equation 5.20) using all parameters restricted to the inner disc. That is; we use the truncated profiles of α_0, η_0, γ_0 and $\overline{u}_0$ only within $|z| < 0.5$ kpc. We also use the initial profiles of mean fields, $\overline{B}_x(z)$ and $\overline{B}_y(z)$, extracted from the DNS but restricted within $|z| < 0.5$ kpc. The final values of β^2; we get in these settings are 1.2, 0.35 and 0.03

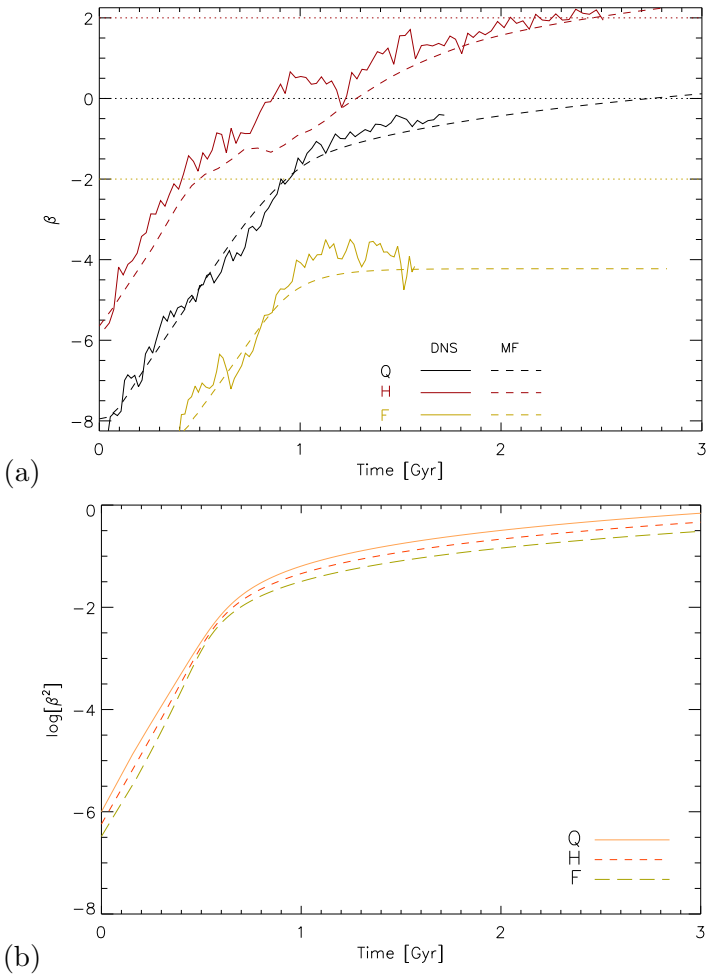

FIGURE 5.10: (a) Comparison of the evolution of β^2 (calculated within the inner disc of $|z| < 0.5\,\mathrm{kpc}$) from DNS (solid lines) and mean field simulations (dashed lines), (calculated using the truncated profiles of dynamo coefficients for $|z| < 0.5\,\mathrm{kpc}$). (b) Same as Figure 5.9 but for $H = 0.5\,\mathrm{kpc}$.

for model Q, H and F respectively (after 2.5, 1.8 and 1.2 Gyr), which are very similar to the results of DNS in the inner disc. Figure 5.10 [*Panel a*] compares the outcome of truncated 1D simulations and DNS restricted to the same vertical range, we find a remarkable agreement between these two. Faster growth rates of β^2 for DNS and truncated 1-D models; during the initial kinematic phase ($\sim 70\,\mathrm{Myr}$) is also consistent with the analytical model discussed earlier (Figure 5.10 [*panel b*]). It is also to be noted that the dynamical phases of models H and F are inconsistent with the results of analytical zero-D model, since we have neglected the contribution of wind for the analytical model.

5.7 The Effect of Net Vertical Flux

The growth rate of E_m in the DNS model QS (with a strong initial vertical flux) is $\sim 200\,\mathrm{Myr}$, until it goes to the dynamical phase and evolves with a slower growth rate. The associated profile of $\overline{B}_y$ is antisymmetric with respect to the mid-plane. Model QSZ (with zero net vertical flux) also shows a similar evolution globally, with a growth rate of 200 Myr during the kinematic phase. Except the geometry of the final $\overline{B}_y(z)$ profile which is symmetric with respect to the mid-plane. This distinction occurs due to the 'vertical flux preserving boundaries'. Using z profiles of the dynamo coefficients and initial mean magnetic fields from the DNS, we simulate the 1D dynamo models (Equation 5.20) equivalent to the models QS and QSZ. In these simulations We find that the overall evolution of magnetic energy is same as that of the DNS and the initially slow growth rate of E_m is a result of large initial values of β. The final asymmetric mode of the mean fields in model QS; turns out to be a consequence of a strong initial 'A' mode that gets preserved throughout the evolution.

Chapter 6

General Evolution of Cosmic Ray Models

6.1 Introduction

In this chapter we discuss the general evolution of the models including the cosmic ray component. Our main motivation here is to explore the effect of cosmic rays on large scale galactic dynamo. The idea of cosmic ray driven dynamo was first discussed by [Parker, 1992]. This predicts, the possibility of enhanced dynamo action by the virtue of additional cosmic ray buoyant instability. Based on a conventional dynamo formulation; Parker suggested a simple model for the flux loss through the gaseous disc due to buoyancy; by substituting the additional transport terms; $-\overline{B}_i/t_d$. These terms are supposed to encapsulate the non advective flux transport, which lead to the fast dynamo action in the characteristic field mixing times $\sim 30\,\mathrm{Myr}$. Hanasz & Lesch [2000] indirectly verified the fast dynamo action via the numerical simulations of rising magnetic flux tubes and found e-folding times of mean field of the order of $\sim 100\,\mathrm{Myr}$. [Girichidis et al., 2014; Hanasz et al., 2004, 2009] quite recently demonstrated the fast amplification of regular magnetic fields via the direct MHD simulation of global galactic ISM including cosmic ray driven turbulence, along with the differential shear (but excluding the viscous term). Using the similar hydrodynamical approach for cosmic ray propagation (explained in Chapter 2), we advance our thermal SN models discussed in preceding chapters. Cosmic rays energy in these models is injected as a predefined fraction of

SN energy. Moreover, by implementing the test fields formulation we also determine the associated dynamo coefficients and discuss the amplification in terms of dynamo mechanism (in next chapter).

6.2 Overview of Studied Models

Dimensions and resolution of the computational domain for cosmic rays models are same as for the thermal SN models described in previous chapters (that is $0.8\,\mathrm{kpc} \times 0.8\,\mathrm{kpc} \times 4.266\,\mathrm{kpc}$ resolved in $96 \times 96 \times 512$ grids). Moreover the initial profiles of mass density, thermal pressure and the rotation are also the same as used in the thermal SN models. Initial magnetic field configuration is chosen in such a way that, $B_x = -10^{-4}\,\mu\mathrm{G}$ in the central disc and decaying outwards with a vertical scale-height of $\sim 325\,\mathrm{pc}$, $B_y = 10^{-3}\,\mu\mathrm{G}$ at $z = 0\,\mathrm{kpc}$ and also decaying outwards with a same scale-height, and constant $B_z = 10^{-3}\,\mu\mathrm{G}$ with a constant net vertical flux of $0.0064\,\mu\mathrm{G\,kpc}^2$ (where B_x, B_y and B_z are x, y and z components of total magnetic field respectively). Used non-zero value of B_z ensures the initial non-zero diffusion of cosmic rays in the vertical direction, which in turn avoids the unphysical initial rise of total cosmic ray energy density inside the box. Used values of the parallel and perpendicular cosmic ray diffusion coefficients ($K_{\parallel}$ and $K_{\perp}$) are $3 \times 10^{27}\,\mathrm{cm}^2\,\mathrm{s}$ and $3 \times 10^{25}\,\mathrm{cm}^2/\mathrm{s}$ respectively. In addition to this, we further include a weak isotropic Fickian diffusion coefficient ensure the diffusion of the grid scale structures [e.g. section 2.2 of Snodin et al., 2006]. Coefficient of the Fickian diffusion, K_{fick} used here is an order of magnitude smaller than $K_{\perp}$. We note that the magnitudes of coefficients $K_{\parallel}$ and $K_{\perp}$ are at least an order of magnitude smaller than the estimated values of Bohm's diffusion coefficients for μG field strengths. A reason to do so, is to get a reasonable computational time step. As a consequence of which; we get a large contribution of total cosmic ray energy throughout the evolution. This possibly affects the distribution of ISM into thermal components. We, therefore, refrain from analyzing the ISM properties in various ISM thermal components and just focus on the evolution of the magnetic energy and the dynamo aspects of the simulations which are possibly least affected by the choice of $K_{\parallel}$ and $K_{\perp}$. Nomenclature and description of CR models is given in Table 6.1

TABLE 6.1: Description of the cosmic ray models with SN rate of $10\%\sigma_0$, 10% of SN energy per explosion is injected in the ISM as cosmic ray energy and rest in the form of thermal energy (E_{th}). All models include a small isotropic Fickian diffusion coefficient $K_{fick} = 3 \times 10^{24}\,\mathrm{cm^2\,s^{-1}}$.

Name	$K_{\parallel}$ $\mathrm{cm^2 s^{-1}}$	$K_{\perp}$ $\mathrm{cm^2 s^{-1}}$	E_{cr} erg	E_{th} erg
`L_CR`	3×10^{27}	3×10^{25}	10^{50}	0
`L_CR_TE`	3×10^{27}	3×10^{25}	10^{50}	9×10^{50}

6.2.1 General Evolution

Starting from the initial total cosmic ray energy $E_{cr} \simeq 6.5 \times 10^{52}\,\mathrm{erg}$, both models evolve to a quasi-stationary state of E_{cr} and E_{kin} within first $\sim 100\,\mathrm{Myr}$. The value of E_{cr} corresponding to this stationary state is ~ 3 times larger for the model involving thermal energy injection `L_CR_TE` (this probably is the adiabatic rise, $\mathrm{p}_c \nabla \cdot \mathrm{u}$). This quasi-stationary states for both cosmic ray models also corresponds to;

1) A multiphase ISM structure, with steady volume filling fractions of all temperature components.

2) Stationary states of total turbulent kinetic E_{kin} and thermal energy E_{th} (Both of these energy contributions are larger in model `L_CR_TH` since the total energy being injected in the box per Myr is 10 times larger than `L_CR`).

3) Steady vertical profiles of average mass density are reached within first 100 Myr.

The initial vertical profile of averaged density is Gaussian with a scale-height of 325 pc, which evolves to the function best fitted with Equation 6.1 within first 100 Myr and remains nearly steady throughout the evolution. Unlike the purely thermal SN models discussed earlier (Q, H, F, etc.), the vertical profiles of average mass density for both cosmic ray models show a visibly distinctive central disc, with a Gaussian functional form within the inner part, $|z| < 0.5\,\mathrm{kpc}$ (this is due to the comparatively larger contribution of dense cold component in CR models, as a result of low energy injection). Within the outer halo however $\rho(z)$ is exponential for both models, with the scale-heights broader than that of the thermal SN models.

$$\rho \;\; = \rho_0 \; exp\left(\left(\tfrac{z}{0.25}\right)^2\right) + \textstyle\sum_{i=0}^{2} \rho_i \; \exp\left(\tfrac{-|\,z\,|}{r_i}\right) . \qquad (6.1)$$

TABLE 6.2: Fitting parameters ρ_i and r_i of $\rho(z)$, using the function Equation 6.1. Where r_0 represents the Gaussian scale-height of central disc and r_1 and r_2 are the exponential scale-heights of outer halo.

Name	ρ_0 cm^{-3}	r_0 kpc	ρ_1 cm^{-3}	r_1 kpc	ρ_2 cm^{-3}	r_2 kpc
`L_CR`	0.2	0.25	0.1	0.32	0.008	1
`L_CR_TE`	0.1	0.25	0.08	0.4	0.01	1.8

Gaussian scale-heights of inner disk, r_0 do not seem to vary very much with the inclusion of cosmic rays. Exponential scale-heights in the outer disc r_1 and r_2, however, are almost 25% and 80% broader respectively for the combined model `L_CR_TE`. Since the total mass in both cosmic ray models is same, the broadening of r_1 and r_2 amounts to the smaller value of average mid-plane density $\sim \rho_0$ in model `L_CR_TE` than model `L_CR`. In Table 6.2 we have listed these fitting coefficients for reference.

After this initial phase of $\sim$ 100 Myr total magnetic energy E_m grows exponentially with the e-folding times of $\sim$ 60 Myr and $\sim$ 70 Myr for models `L_CR` and `L_CR_TH` respectively (which is comparatively faster than the purely thermal SN models with e-folding times of $\sim$ 100 Myr). Both of these models have been evolved up to $\sim$ 600 Myr. The maximum value of ratio E_m/E_{kin} approached until that time is approximately 10^{-3} (in both models). The dynamical effects of magnetic field, therefore, are minimal and we restrict the discussion of the cosmic ray models; only to the kinematic phase. In Figure 6.1 we have shown the time evolution of different energies in both cosmic ray models, which clearly represents the aforementioned properties.

6.2.2 Magnetic Fields

Total magnetic field here is again represented as a sum of mean and turbulent magnetic fields. We also define the average on $x-y$ plane. Looking at the overall evolution of mean field, $\overline{\mathbf{B}}$, we find that the radial component $\overline{B}_x$ stays 3 to 5 times smaller than its azimuthal component $\overline{B}_y$, and has a same functional form except for the opposite sign. So in order to avoid the further confusion we describe only $\overline{B}_y$ component hereafter.

Starting from the weak initial, $\overline{B}_y(z)$ (and $\overline{B}_x(z)$), in both cosmic ray models evolve to a vertically symmetric, double peaked quadrupolar mode, within first $\sim$ 100 Myr. This time also maps to the slow initial growth phase of magnetic energy as seen from Figure 6.1. Maximums of these profiles appear at $\sim \pm 0.2$ kpc. The overall functional

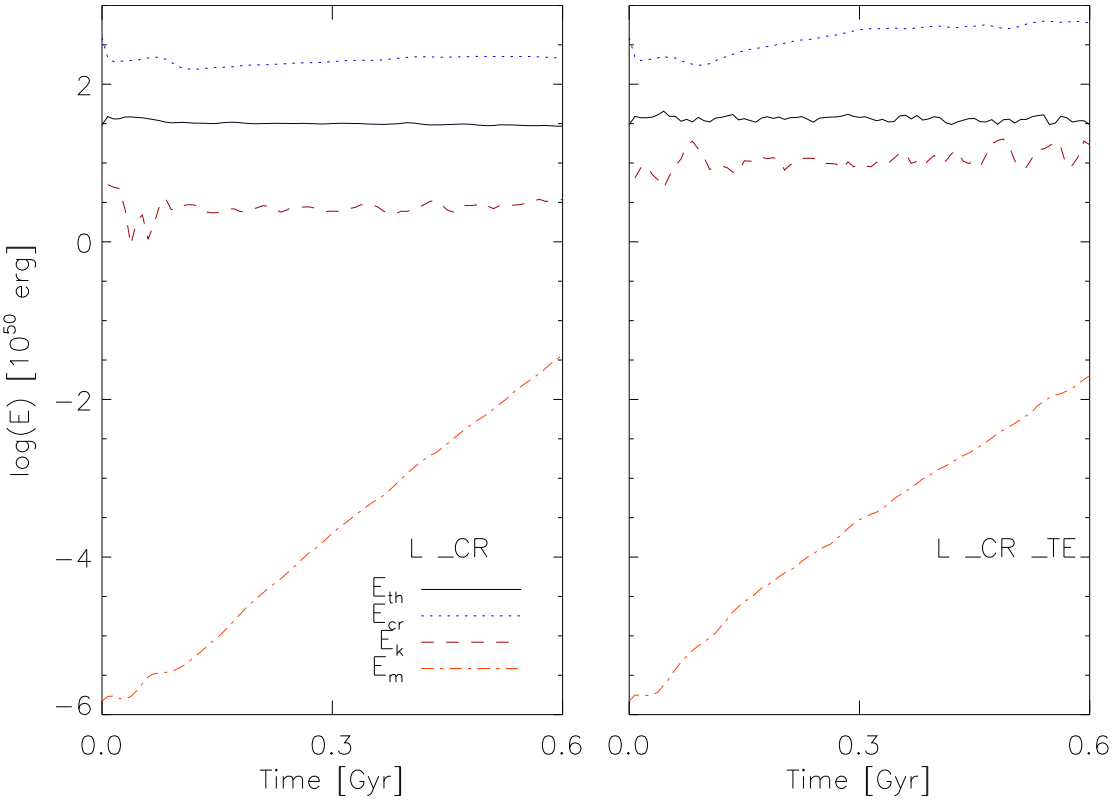

FIGURE 6.1: Evolution of CR energy (blue-dotted lines), thermal energy (black-solid lines), turbulent kinetic energy (red-dashed lines) and magnetic energies (orange-dot-dashed lines) for both cosmic ray models.

form the quadrupolar mode, stays unchanged throughout the evolution, however, the magnitude of mean field grows exponentially with approximate e-folding time of 130 Myr for both cosmic ray models. We evolve these models for ~ 600 Myr up to which the peak values of $\overline{B}_y$ grow to $\sim 0.06\,\mu$G in both models; as shown in Figure 6.2.

Although the functional form of $\overline{B}_y(z)$ is approximately similar for `L_CR` and `L_CR_TE`, central peaks in $\overline{B}_y$ profile of model `L_CR` seem to be narrower and more concentrated in the disk; compared `L_CR_TE`, as shown in Figure 6.2. The exponential scale-heights of $\overline{B}_y(z)$ in the inner range $0.2\,\text{kpc} < |z| < 0.8\,\text{kpc}$ are about 0.25 kpc and 0.15 kpc for models `L_CR_TE` and `L_CR` respectively. Whereas in the outer range $|z| > 0.8\,\text{kpc}$ exponential scale-heights are approximately 0.35 and 0.18 kpc respectively. Broader profile of $\overline{B}_y$ is presumably an outcome of the inadequate advection of mean field in purely CR model `L_CR`, due to a comparatively slower outward wind in the central disk (described in Section 6.2.3).

The symmetric quadrupolar poloidal component predicted in the CR models is possibly present in the disk galaxies, which is also reflected in the X-shaped fields seen in various

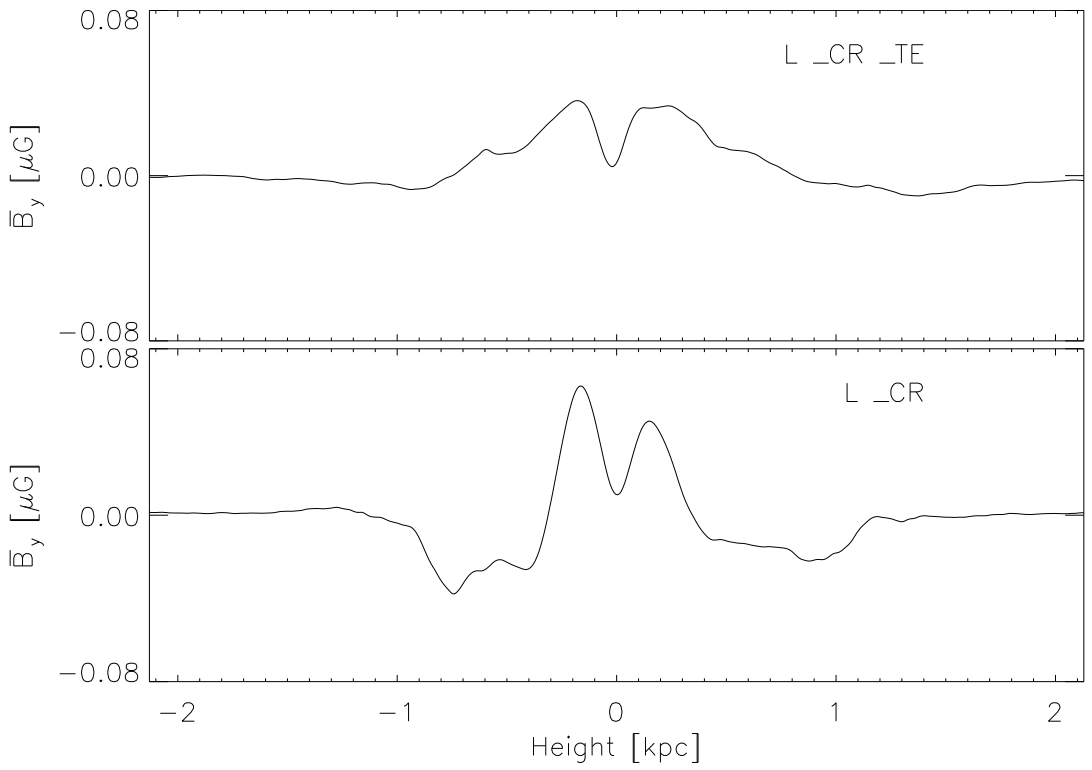

FIGURE 6.2: Vertical profiles of mean azimuthal magnetic fields after 600 Myr, for both CR models.

observations of edge-on spirals [e.g. Beck, 2015; Mora & Krause, 2013]. Whereas, the double peaked structure has not been explicitly seen in the nearby galaxies. It is however premature to compare these scale-heights directly to the observed values, since the models are still in the kinematic growth phase.

Similar to the mean fields ($\overline{B}_y(z)$), the turbulent fields, $\mathbf{b}'_y(z)$, also evolve to a double peaked profile, after about 100 Myr and further amplify exponentially with an e-folding time of ~ 130 Myr, while preserving the overall shape of $\mathbf{b}'_y(z)$. Peak values of these are situated at about 0.2 kpc, with a magnitude of 0.04 μG as shown in Figure 6.3, for both CR models. Exponential scale-heights of turbulent field in the outer halo $|z| > 0.8$ kpc are about 0.75 and 1 kpc for models `L_CR` and `L_CR_TE` respectively. Broader scale-height in the outer halo of model `L_CR_TE` can again be attributed to the efficient advective and (/or) diffusive transfer.

Relative strength of mean magnetic field with respect to the turbulent component is expressed by a ratio, $\left|\bar{\mathbf{B}}\right| / \left|\mathbf{b}'\right|$. Starting from initially larger value (contributed mostly by the seed field) this ratio sharply decays to constant, within first ~ 150 Myr, and stays unchanged throughout the evolution for both models. However, the effect of mean field

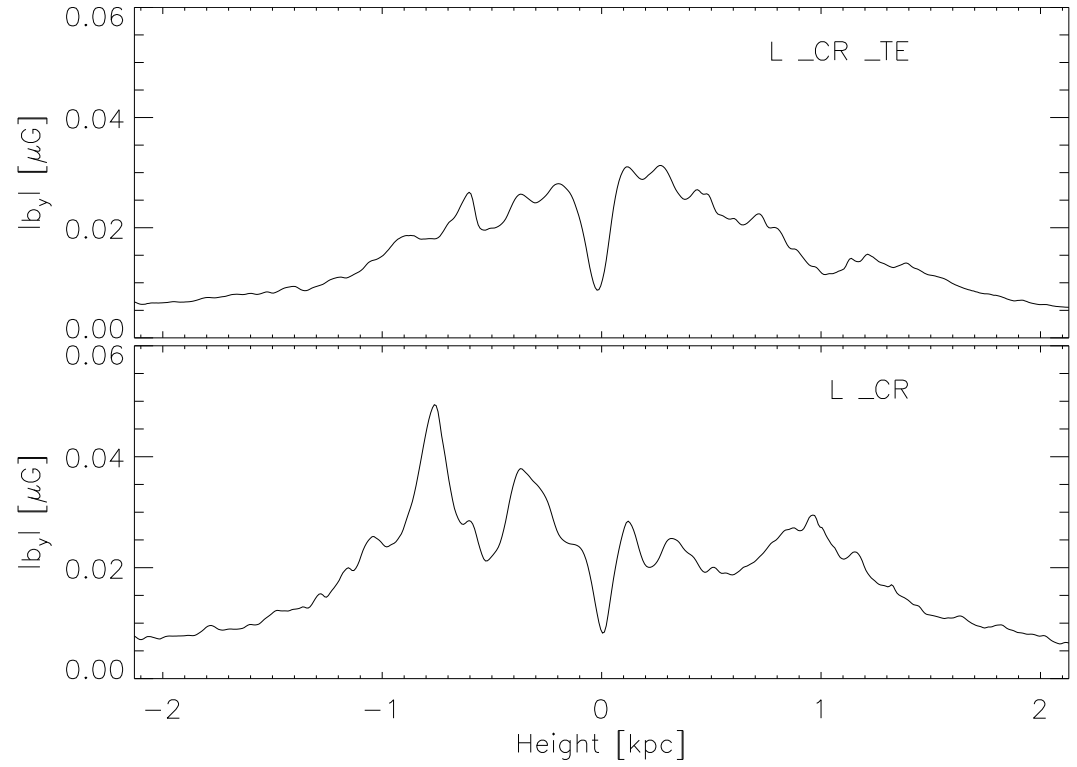

FIGURE 6.3: Vertical profiles of azimuthal components of turbulent magnetic fields after 600 Myr, for both CR models.

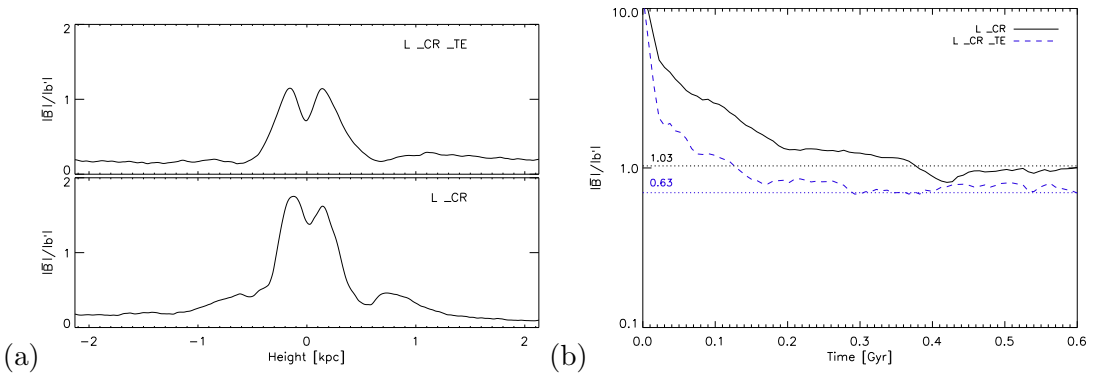

FIGURE 6.4: (a) Typical vertical profiles of the ratio of mean to turbulent magnetic field strengths. (b) Evolution of $\left|\bar{\mathbf{B}}\right| / |\mathbf{b}'|$ for both CR models.

on this ratio is unclear since we have not run these simulations during the dynamical phase. Figure 6.4 [*Panel a*] represents the vertical distribution of $\left|\bar{\mathbf{B}}\right| / |\mathbf{b}'|$ from 150 to 600 Myr, which closely resembles to the shapes of mean field distributions shown in Figure 6.2 in the central part $|z| < 0.8$ kpc, hinting that the generation of turbulent field is probably taking place via the mechanism of field line tangling. If we consider the inner disc part of $|z| < 0.5$ kpc, constant values of $\left|\bar{\mathbf{B}}\right| / |\mathbf{b}'|$ reach to ~ 1.03 and ~ 0.63 for models `L_CR` and `L_CR_TE` respectively, which we have depicted in Figure 6.4 [*Panel*

b]. While in the outer halo part, the turbulent component generally dominates and the value of $\left|\bar{\mathbf{B}}\right| / |\mathbf{b}'|$ drops down to only 0.2, for both cosmic ray models. The constant value of this ratio in the inner disc of model `L_CR_TE` roughly follows the scaling law obtained for thermal SN models ($\sim \sigma^{-0.3}$) it is however elevated in purely CR model `L_CR` probably due to the less total energy injection per SN explosion.

6.2.3 ISM Velocities

ISM velocities $\mathbf{u}$; are expressed as a sum of mean, $\overline{\mathbf{u}}$, and fluctuating $\mathbf{u}'$ parts. Since the distribution of SN is uniform over the $x-y$ planes, we do not see any radial or azimuthal component of mean velocity, and the only surviving component is vertical wind, $\overline{\mathbf{u}}_z$, which achieves a stationary vertical profile within first 100 Myr. Another large scale velocity component is the azimuthal one, which arises due to preset differential shear, mean of this component cancels out in the box frame of reference. Unlike the purely thermal SN models (Q, H, F, etc.), $\overline{\mathbf{u}}_z(z)$ profiles here are roughly linear only within the inner disc ($|z| < 0.8$ kpc) and quadratic in the outer halo, as shown in Figure 6.5 [*Panel left*] for both cosmic ray models, this hints to the possibility of cosmic ray pressure being a driver of wind in addition to the galactic fountain mechanism, and may even be the dominant factor in outer halo.

Amplitudes of the linear segment of $\overline{\mathbf{u}}_z(z)$ (within approximately $|z| < 1.$ kpc) in model `L_CR_TE` is $\sim \pm 5\,\mathrm{km\,s^{-1}}$, at $\sim \pm 0.8$ kpc, which follows the SN scaling law obtained in Chapter 3 (section 3.2.6), corresponding to the SN rate of `L_CR_TE` ($0.1\sigma_0$). Whereas, the quadratic flaring of $\overline{\mathbf{u}}_z(z)$ in the outer halo (above $z = 1.$ kpc) is presumably due to the comparatively larger gradient of CR energy. Similarly for model `L_CR`; there also exists a quadratically growing wind in the halo part (since a same magnitude of cosmic ray energy is being injected), whereas for the inner disc $\overline{\mathbf{u}}_z(z)$ is relatively flatter, due to the absence of thermal energy input. In Figure 6.5 [*Panel left*] we have compared the $\overline{\mathbf{u}}_z(z)$ profiles of both cosmic ray models, and overplotted (red-dotted line) is the scaled down wind profile of model F for the SN rate of $0.1\sigma_0$.

Turbulent velocity component $\mathbf{u}'(z)$, evolves to a quasi stationary state within first 100 Myr, in both cosmic ray models. Radial and azimuthal components of steady $\mathbf{u}'(z)$ profiles are roughly inverted bell shaped within $|z| < 1.8 \pm 0.2$ kpc, and a very steep quadratic functions above this range (in order to eliminate the boundary effect as a

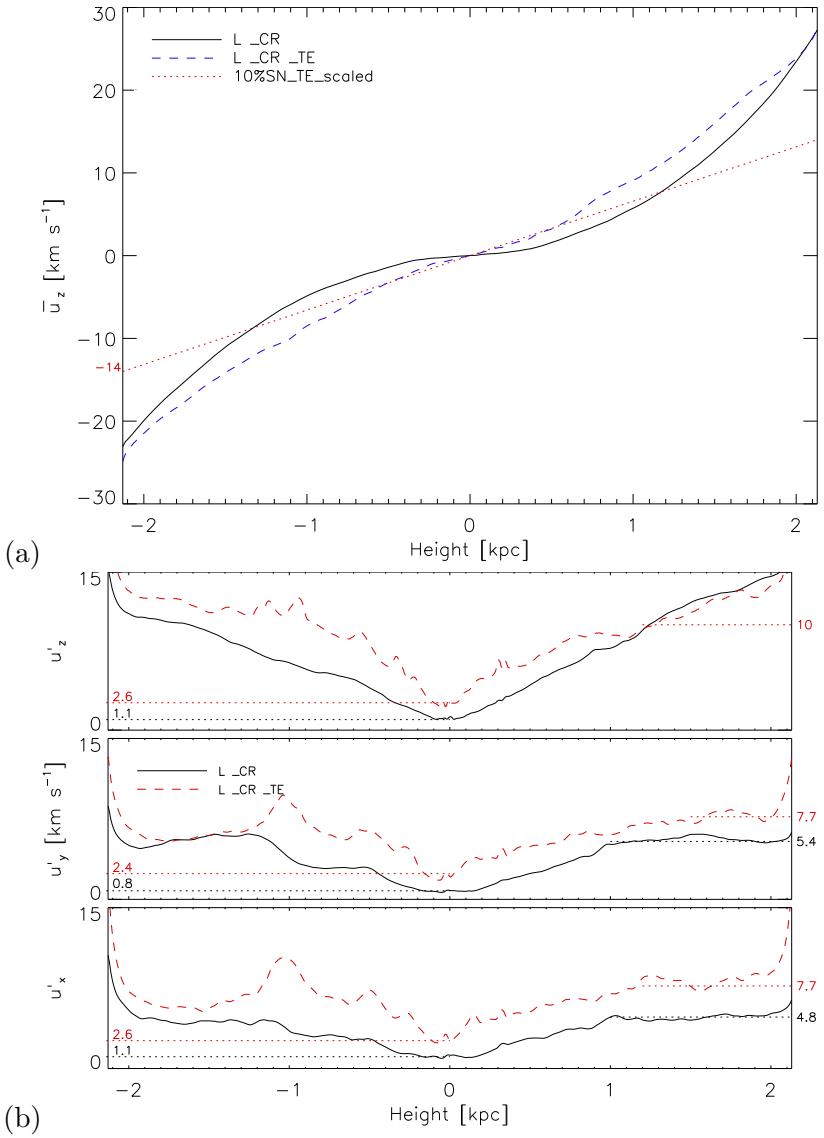

FIGURE 6.5: (a) Vertical profiles of outward wind for model L_CR(blue-dashed line) and L_CR_TE (black-solid line), red-dotted line represents the vertical wind profile of the thermal SN model with equivalent SN rate as CR models, obtained by using the SN scaling law discussed in Section 3.2.6 ($\bar{u}_z \sim \sigma^{0.4}$). (b) Typical vertical profiles of turbulent velocity components for model L_CR (black-solid line) and L_CR_TE (red-dotted line).

plausible reason for the steep outer curves; larger box simulations need to be performed to include the outer radio halo), as shown in Figure 6.5. Maximum amplitudes of the inverted bell part range up to $\sim 5\,\mathrm{km\,s^{-1}}$ and $\sim 8\,\mathrm{km\,s^{-1}}$ for models `L_CR` and `L_CR_TE`, while the very outer steep curves go up to $\sim 15\,\mathrm{km\,s^{-1}}$. While the vertical ($z$) components are the liner functions of z ranging from ~ 1 to $2\,\mathrm{km\,s^{-1}}$ in the mid-plane to $\sim 15\,\mathrm{km\,s^{-1}}$ at the outer boundaries. Mid-plane values of $\mathbf{u}'$ in model `L_CR_TE` are $\sim 2.5\,\mathrm{km\,s^{-1}}$, which are consistent with the SN scaling law for u$'$ obtained in Chapter 3, corresponding to the SN rate of $0.1\sigma_0$, while in the outer halo part these are about 50%

smaller than the scaling estimates for $0.1\sigma_0$, again implying the fact that the additional cosmic ray pressure affects prominently in halo part and suppresses the velocity fluctuations. This is generally true for model `L_CR`, except the mid-plane values of $\mathbf{u}'$ are only about $1\,\mathrm{km\,s^{-1}}$, probably due to the absence of thermal energy injections.

6.2.4 Alfvén Velocity

Using the definition of Alfvén velocities, expressed by Equation 3.6, we calculate, $v_A(z)$ and $v'_A(z)$ profiles for both cosmic ray models. Similar to models Q, H and F, etc., these profiles are also inverted bell shaped within the inner disc ($|z| < 0.8\,\mathrm{kpc}$) and decreasing or constant in the halo ($|z| > 0.8\,\mathrm{kpc}$), with maximum strengths of $2\,\mathrm{km\,s^{-1}}$ in the halo. These are much smaller than the wind velocities. Since the magnetic field has not yet reached to the equipartition strength v_A is still evolving and presumably doesn't have any dynamical impact on ISM on large scale.

Chapter 7

Cosmic Ray Dynamo

7.1 Introduction

In the preceding chapters we have described the several different properties of ISM in purely thermal SN models and in the models involving cosmic ray injections. We also showed that in the model with CR and CR + thermal energy, large scale dynamo effectively works and magnetic amplifies with the fast exponential folding time of 60 to $\sim 70\,\mathrm{Myr}$. However we have not yet analyzed the ISM distribution and the effect of CR pressure on it, we plan to do that in the future. It also interests us to understand this growth as a mean field dynamo. For that we simulate an equivalent 1D dynamo model, similar to the one we have presented in Chapter 5. Dynamo description allows us to indirectly determine the effect of cosmic rays on the underlying turbulence properties.

7.2 Dynamo Coefficients

Using the test fields method described in Chapter 5, we compute the vertical profiles of dynamo coefficients, α and η for both cosmic ray models, as a function of time. It turns out that after the initial mixing phase of $\sim 100\,\mathrm{Myr}$, these profiles reach to a quasi-stationary state, which remain so; for the entire evolution. Also we do not see any effect of magnetic fields on these profiles, since the maximum value of mean magnetic field energy relative to the turbulent kinetic energy (β) at the end of evolution reaches only to ~ 0.05 (in both cosmic ray models). In Figure 7.1 and Figure 7.2 we

have compared the vertical profiles of dynamo coefficients for both cosmic ray models, which clearly shows that $\alpha(z)$ and $\eta(z)$ magnitudes in purely cosmic ray model (`L_CR`) are about 50% weaker than that of model `L_CR_TE`. Unlike the purely thermal SN models (Q, H, F, etc.). The off-diagonal terms of α tensors in both CR models do not contribute as an isotropic diamagnetic pumping term, and the terms α_{xy} and α_{yx} are therefore interpreted as the differential rates of the flux transport for components $\bar{B}_x$ and $\bar{B}_y$ respectively. Furthermore the off-diagonal elements of α tensor do not cancel out outward wind component as they do in the kinematic phases of the thermal SN models; leaving sufficiently large residual transport terms. Another important distinction in the CR models is the non-negligible contribution of the off-diagonal η terms; for instance the ratio $\eta_{xx}/\eta_{xy} \sim 2$ in CR models as opposed to ~ 15 in purely thermal SN models. These distinctions systematically lead to the double peaked structure of mean field as discussed in the next section.

Using the SN scaling laws for dynamo coefficients (obtained in Table 5.1 for purely thermal SN models) we can estimate the values of α and η for model with SN rate of $0.1\sigma_0$, with purely thermal SN explosions, and check whether these match with the numerical values obtained from the DNS. However it turns out that these estimates are 4 to 8 times smaller than the test field results listed in Table 7.1 for both CR models, highlighting the distinction between the CR and thermal SN turbulence. Another approach to estimate the numerical values of dynamo coefficients is the SOCA approximation, under the assumption of isotropic and homogeneous turbulence in high conductivity limit Equation 5.5. The profiles of turbulent intensity and turbulent diffusivity obtained from the DNS along with the SOCA estimates gives the turbulent correlation time τ_c for η; $\sim 35\,\mathrm{Myr}$, which is much prolonged compared to the thermal SN models ($\sim 10\,\mathrm{Myr}$) and the understanding of its effect on the ISM structure warrants, a detailed analysis turbulence properties in different ISM phases, which is beyond the scope of current analysis. It is however to be noted here that, there is an emergent anisotropy in the distribution of turbulent intensity, leading to the asymmetric α tensors; which imply for CR models that the SOCA estimate is only approximately valid.

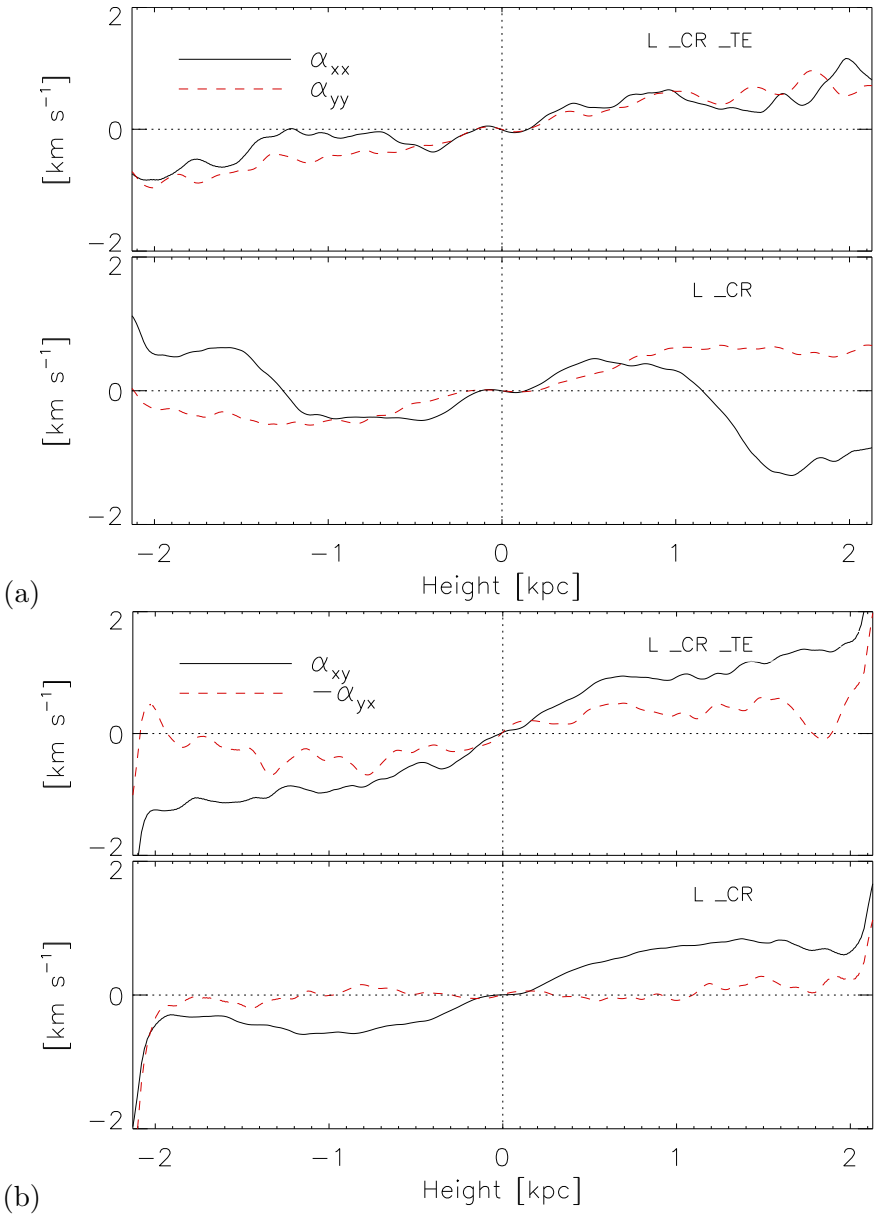

FIGURE 7.1: Vertical profiles of the α coefficients for both cosmic ray models averaged for 100 to 200 Myr. Top panels represent model L_CR_TE and bottom panels represent the model L_CR. *Panel a* : $\alpha_{xx}(z)$ and $\alpha_{yy}(z)$, *Panel b* : $\alpha_{xy}(z)$ and $\alpha_{yx}(z)$

7.3 Outline of the Mean Field Model

To understand the underlying dynamo mechanism involved in the amplification of E_m, we use 1D mean field dynamo model, with the horizontal averages defined on $x-y$ planes. This model is similar to the one used in Chapter 5 (Equation 5.20), the difference however arises from the emergent asymmetric nature of α tensor ($|\alpha_{xy}| \neq |\alpha_{yx}|$), and non-negligible off-diagonal η tensor. But we have still neglected the microscopic diffusivity

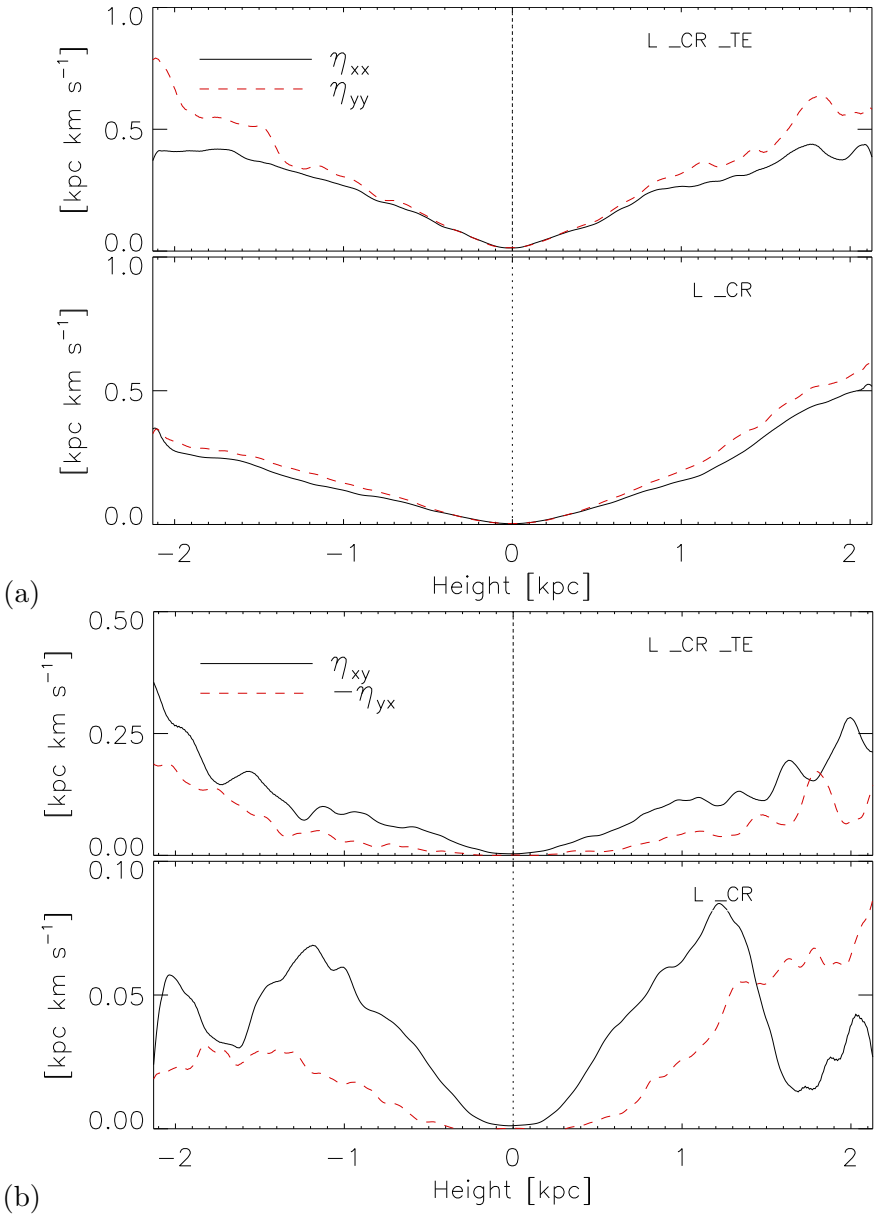

FIGURE 7.2: Vertical profiles of the η coefficients for both cosmic ray models averaged for 100 to 200 Myr. Bottom panels represent model L_CR_TE and top panels represent the model L_CR. *Panel a* $\eta_{xx}(z)$ and $\eta_{yy}(z)$ *Panel b* $\eta_{xy}(z)$ and $\eta_{yx}(z)$

$\tilde{\eta}$, since it is more than an order of magnitude smaller than the turbulent diffusivity. We finally get the following set of equations,

$$\begin{aligned}
\frac{\partial \bar{B}_x}{\partial t} &= \frac{\partial}{\partial z}\left(-\left(\bar{u}_z + \alpha_{yx}\right)\bar{B}_x - \alpha_{yy}\bar{B}_y + \eta_{yy}\frac{\partial \bar{B}_x}{\partial z} - \eta_{yx}\frac{\partial \bar{B}_y}{\partial z}\right), \\
\frac{\partial \bar{B}_y}{\partial t} &= \frac{\partial}{\partial z}\left(-\left(\bar{u}_z - \alpha_{xy}\right)\bar{B}_y + \alpha_{xx}\bar{B}_x + \eta_{xx}\frac{\partial \bar{B}_y}{\partial z} - \eta_{xy}\frac{\partial \bar{B}_x}{\partial z}\right) + q\,\Omega\bar{B}_x\,. \quad (7.1)
\end{aligned}$$

TABLE 7.1: Dynamo coefficients for both cosmic ray models, at $z = 1\,\mathrm{kpc}$, Averaged over 200 Myr.

	α_{xx} $[\mathrm{km\,s^{-1}}]$	α_{yy} $[\mathrm{km\,s^{-1}}]$	α_{xy} $[\mathrm{km\,s^{-1}}]$	α_{yx} $[\mathrm{km\,s^{-1}}]$
L_CR	0.3± [0.08]	0.5± [0.15]	0.5± [0.20]	0.0± [0.10]
L_CR_TE	0.6± [0.15]	0.8± [0.20]	1.0± [0.30]	0.5± [0.20]
	η_{xx} $[\mathrm{kpc\,km\,s^{-1}}]$	η_{yy} $[\mathrm{kpc\,km\,s^{-1}}]$	η_{xy} $[\mathrm{kpc\,km\,s^{-1}}]$	η_{yx} $[\mathrm{kpc\,km\,s^{-1}}]$
L_CR	0.2± [0.03]	0.2± [0.04]	0.06± [0.01]	0.04± [0.01]
L_CR_TE	0.3± [0.03]	0.4± [0.08]	0.10± [0.03]	0.07± [0.02]

Notes: Bracketed numbers indicate the maximum errors.

Similar to the thermal SN models, we evolve Equation 7.1, using the finite difference approach on a staggered grid of resolution $n = 512$. Initial conditions for $\bar{B}_x(z)$ and $\bar{B}_y(z)$ are chosen from the DNS magnetic field data; averaged over 70 to 90 Myr (over the $x-y$ plane). This choice is justified since the growth of magnetic energy starts only after $\sim$ 80 Myr. Steady vertical profiles of the dynamo coefficients are also obtained by averaging DNS data over 70 to 90 Myr. To reduce the high wave number noise in their z profiles, we $\alpha(z)$ (and $\eta(z)$) with 15 odd (and even) Legendre polynomials. z profiles of the outward wind, $\bar{u}_z(z)$ are also taken from DNS results and fitted with 15 odd Legendre polynomials.

Since the maximum values of β achieved in both cosmic ray models (until 600 Myr) are only ~ 0.01, we ware not able to derive the magnetic quenching relations for the dynamo coefficients. In the 1D models however, we can presume the validity of Equation 5.18 and Equation 5.18; even for the CR models, allowing us to predict the field strengths corresponding to the dynamical phases of equivalent models.

7.4 Comparison of Mean Field and Direct Simulations

To avoid the complication; we refer 1D equivalents of DNS cosmic ray models also by the names `L_CR` and `L_CR_TE`. Comparison between these two is discussed in this section.

Apart from initial mixing phase of approximately 80 Myr, we ware able to reproduce entire evolution curve of the mean field magnetic energy using 1D dynamo models, and the results match remarkably. This fact is well represented in Figure 7.3, where

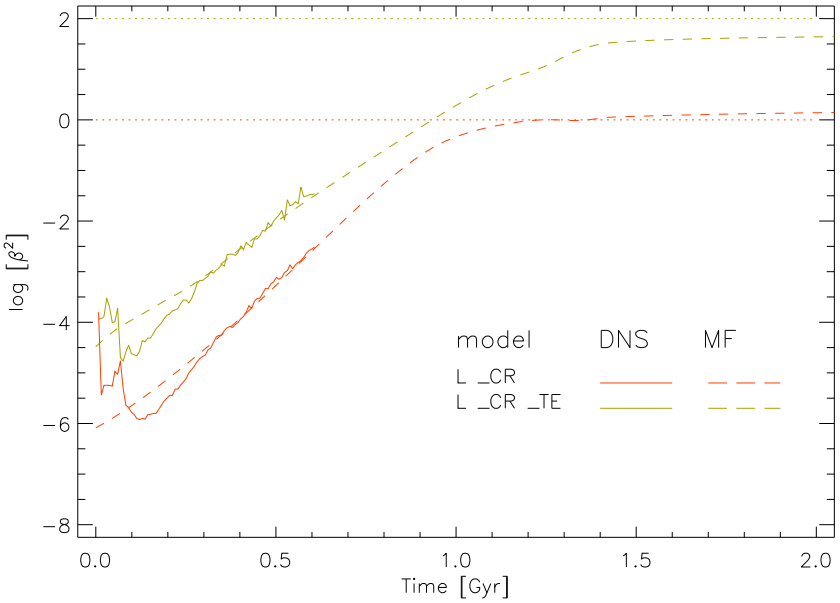

FIGURE 7.3: Evolution of the relative strength of mean magnetic fields (β^2) calculated from DNS models (solid lines) and from 1D models (dashed lines) for both cosmic ray models. Red lines indicate the evolution of β^2 in model L_CR whereas green lines indicate the same for model L_CR_TE. Dotted horizontal lines at $\beta^2 = 1$ and 100, signify the equipartition energy for corresponding models. β^2 in L_CR_TE is multiplied by 100.

solid lines show time evolution of the mean field magnetic energy (normalized with the kinetic energy) in DNS cosmic ray models, and dashed lines represent the same for equivalent 1D models. To avoid the clutter we have multiplied the energy in model `L_CR_TE` (green lines) by 100; the dashed horizontal lines at $log[\beta^2] = 0$ and 2 therefore represent the equipartition in corresponding model. Initial drop of the magnetic energy seen in DNS models corresponds to the time it takes for vertical profiles of cosmic ray energy and outward wind to become roughly stationary in time. So; as far as we are concerned about the stationary growth of magnetic energy, this initial phase can be omitted (with a simple dynamo perspective). For the mean field models therefore, we have used the α and η profiles averaged over the linear part of E_m, consequently initial drop of magnetic energy is absent in 1D models. We also see a relatively fast growth rates of mean magnetic energy, compared to the thermal SN models, which can be attributed to the turbulent diffusion time (t_d) and associated parameters as follows. Firstly the amplitudes of dynamo coefficients for CR models are smaller than their expected values from SN scaling laws. The outward wind profiles, on the other hand, are stronger than their expected amplitudes. As a result, the transport term in cosmic ray models is non-zero, already in the kinematic phase. Characteristic vertical length scale, H, over which the off-diagonal α terms cancels the outward wind, is only about

$\sim 0.30\,\mathrm{kpc}$, this is significantly smaller than the analogous length scale in purely thermal SN models ($\sim$ 1 kpc see Section 5.6.2). This length scale signifies the domain over which $\alpha\Omega$ dynamo approximation is valid, as described in Section 5.6.1. The turbulent diffusion time (H^2/η) for both cosmic ray models, however is still relatively longer than the thermal SN models and the unquenched values of dynamo number D_0 are higher leading to the the faster growth of mean field in both cosmic ray models. We support this hypothesis with the analytical 0D model discussed in Section 5.6.2. By substituting the appropriate values of H and dynamo coefficients in Equation 5.27 we recover the faster initial growth in CR models Figure 7.4 (*Panel left*). Whereas, with reducing the turbulent diffusion time (for $H \sim 1\,\mathrm{kpc}$) we find that the growth time again falls down to 100 Myr, same as thermal SN models Q, H and F. We further crosscheck this, by replacing $\overline{\mathrm{u}}(z)$ profiles in 1D models by approximated linear profiles that match $\alpha_{xy}(z)$ in the inner 1 kpc scale (equivalent to thermal SN models) and recover the slow growth rates of $\sim 100\,\mathrm{Myr}$ as expected (Figure 7.4, *Panel right.*)

1D dynamo model also explains entire time evolution of the vertical profiles of mean field. For example in Figure 7.10 and Figure 7.5 we compare the space-time contours $\bar{B}_x$ and $\bar{B}_y$ calculated via DNS and 1D models. The qualitative structures of $\bar{B}_x$ and $\bar{B}_y$, as shown in the aforementioned figures, are well reproduced in 1D model, along with the initial split of symmetric S mode to the double peaked structure, at around 200 Myr. To have a more quantitative comparison we plot the final vertical profiles of $\bar{B}_x$ and $\bar{B}_y$, using the DNS models and 1D models, and compare the corresponding scale-heights and amplitudes, which are remarkably similar in both approaches, as shown in Figure 7.6 as well as Figure 7.9. Reason for the double peaked symmetric structure of the mean field (unlike the thermal SN models), as a first approximation, can be assigned to the following qualitative differences; in the profiles of dynamo coefficients of CR and thermal SN models: (i) Unequal absolute values of the off-diagonal elements of α tensors, leading to the anisotropic non-advective transport of magnetic flux. (ii) non-negligibly contributing off-diagonal terms of η tensor, indicating the transverse diffusive transport of magnetic flux [1]. (iii) Non-linear (approximately quadratic) outer profiles of $\overline{\mathrm{u}_z}(z)$, leading to the enhanced advection in the outer halo. To figure out which one (or a combination) of these three factors lead to the double peaked geometry of mean fields, we run 1D dynamo model in the different regimes of parameter space. This exercise reviles

[1] in the special case of isotropic and homogeneous turbulence in high conductivity limit, coefficients η_{xy} and η_{yx} simply reduce to $\overline{\mathrm{u}'_x\,\mathrm{u}'_y}\,\tau_c/3$ [Choudhuri, 1998]

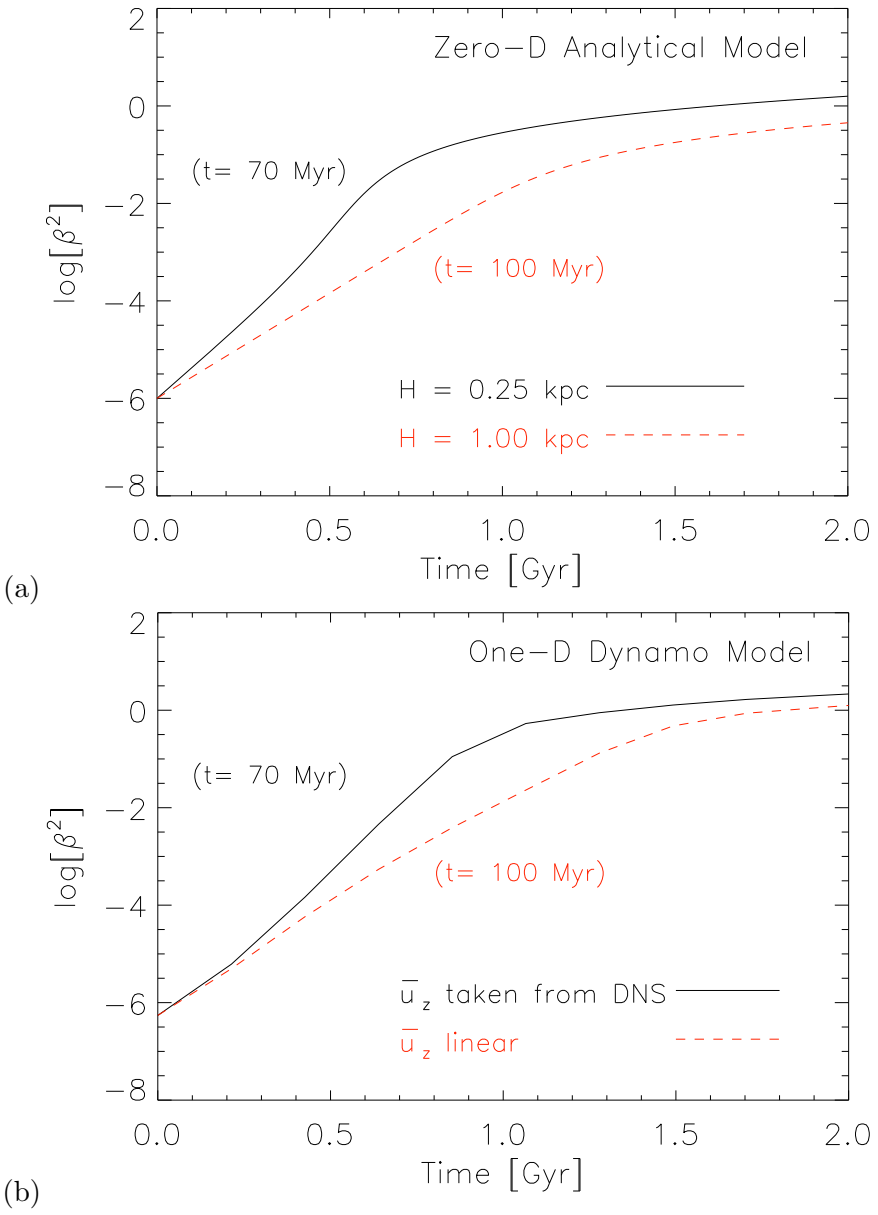

FIGURE 7.4: *Panel a*: Time evolution of the relative strength of total magnetic energy (β^2), calculated analytically. Black solid lines indicate the model with the vertical scale-length $H = 0.25\,\mathrm{kpc}$, whereas the dashed orange lines correspond to the scale-length of $H = 1\,\mathrm{kpc}$. Exponential growth times in these models are $\sim 70\,\mathrm{Myr}$ and $100\,\mathrm{Myr}$ respectively. *Panel b* : Same as *Panel a* but calculated with one-D dynamo model, by varying the vertical wind profiles.

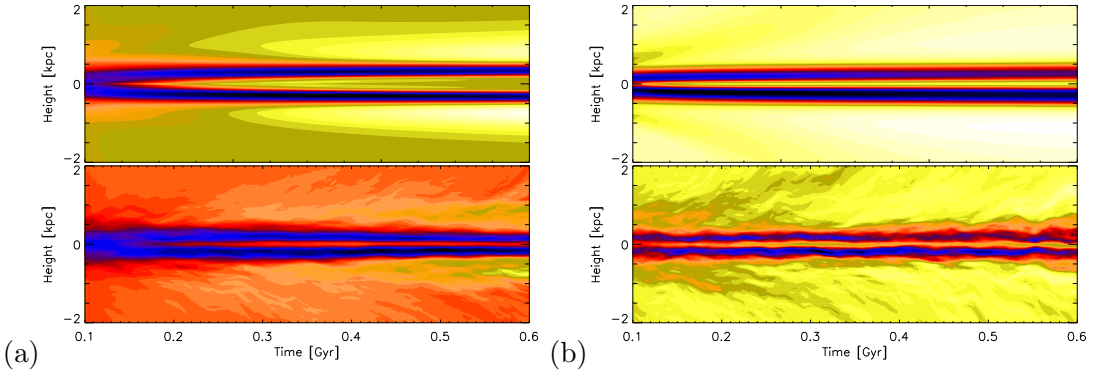

FIGURE 7.5: Space-time diagrams of $\bar{B}_y$ calculated from DNS (*Panel down*) and via 1D simulations (*Panel up*) for, (a) model L_CR (b) model L_CR_TE color code here indicates the strength of mean azimuthal magnetic field normalized with the square-root of magnetic energy.

that the S modes of $\bar{B}_y$ appear only when the outward wind is linear in z (matching with its DNS profile in the inner part; as shown in Figure 7.8) and off-diagonal terms of η are zero. Asymmetric contribution of the diamagnetic term ($\alpha_{xy/yx}$) has a very little impact on final geometry of the mean field and even on its growth rate. This implies that the double peaked structure is a combined outcome of excessive wind in outer halo and anisotropic diffusive transport of magnetic flux. Parameters space analysis of 1D model is briefly summarized in Table 7.2 (in the last two columns we have listed the final geometry of the mean field) and the S modes of $\bar{B}_y$ corresponding to case 3 and 4 in aforementioned table are shown in Figure 7.7.

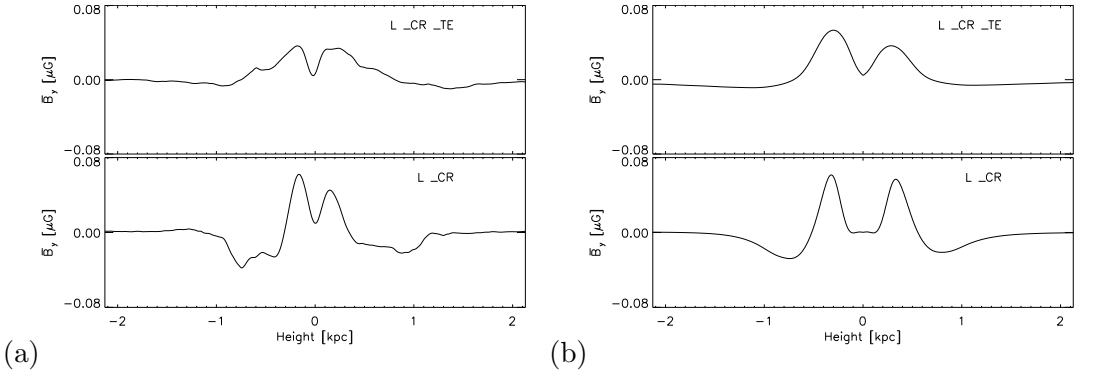

FIGURE 7.6: Vertical profiles of $\bar{B}_y$ calculated for model L_CR (*Panel up*) and model L_CR_TE (*Panel down*) calculated via (a) Direct numerical simulations (b) 1D dynamo simulations.

If the same quenching laws (Equation 5.18 and Equation 5.19) for dynamo coefficients and wind are to be assumed for the CR models, growth rates of E_m in both CR models drop significantly after ~ 1 Gyr, as shown in Figure 7.3. A reason for this, is a strong non-advective transport term (wind - pumping) in the dynamical phases of both CR models,

TABLE 7.2: Final geometries of mean field in 1D dynamo model, for the different sets of dynamo coefficients.

	α_{xy} and α_{yx}	η_{xy} and η_{yx}	$\overline{B}_y(z)$ at 600 Myr	$\overline{B}_y(z)$ at 3 Gyr
		$\overline{\mathrm{u}}_z(z)$ = Linear		
Case 1	$\alpha_{xy}(z)$ DNS $\alpha_{yx}(z) = -\alpha_{xy}(z)$	$\eta_{xy}(z)$ DNS $\eta_{yx}(z)$ DNS	double peaked same amplitudes	double peaked different amplitudes
Case 2	$\alpha_{xy}(z)$ DNS $\alpha_{yx}(z)$ DNS	$\eta_{xy}(z)$ DNS $\eta_{yx}(z)$ DNS	double peaked different amplitudes	double peaked different amplitudes
Case 3	$\alpha_{xy}(z)$ DNS $\alpha_{yx}(z) = -\alpha_{xy}(z)$	$\eta_{xy}(z) = 0$ $\eta_{yx}(z) = 0$	**single peaked** **S mode**	**single peaked** **S mode**
Case 4	$\alpha_{xy}(z)$ DNS $\alpha_{yx}(z)$ DNS	$\eta_{xy}(z) = 0$ $\eta_{yx}(z) = 0$	**single peaked** **S mode**	**single peaked** **S mode**
		$\overline{\mathrm{u}}_z(z)$ = DNS		
Case 5	$\alpha_{xy}(z)$ DNS $\alpha_{yx}(z) = -\alpha_{xy}(z)$	$\eta_{xy}(z)$ DNS $\eta_{yx}(z)$ DNS	double peaked same amplitudes	double peaked different amplitudes
Case 6	$\alpha_{xy}(z)$ DNS $\alpha_{yx}(z)$ DNS	$\eta_{xy}(z)$ DNS $\eta_{yx}(z)$ DNS	double peaked different amplitudes	double peaked different amplitudes
Case 7	$\alpha_{xy}(z)$ DNS $\alpha_{yx}(z) = -\alpha_{xy}(z)$	$\eta_{xy}(z) = 0$ $\eta_{yx}(z) = 0$	double peaked same amplitudes	double peaked same amplitudes
Case 8	$\alpha_{xy}(z)$ DNS $\alpha_{yx}(z)$ DNS	$\eta_{xy}(z) = 0$ $\eta_{yx}(z) = 0$	double peaked different amplitudes	double peaked same amplitudes

Notes: Final structures of mean field at 0.6 and 3 Gyr are described in last two columns, in the different regions of dynamo parameter space. $\alpha_{xx/yy}(z)$ (and $\eta_{xx/yy}(z)$) profiles are chosen from DNS data by fitting it with odd (and even) Legendre polynomials. In first 4 cases, approximated linear profiles of $\overline{\mathrm{u}_z}(z)$ are used, these profiles are shown in Figure 7.8. Whereas for the last 4 cases $\overline{\mathrm{u}_z}(z)$ are directly taken from DNS. Final 'S' modes appear only in case 3 and case 4.

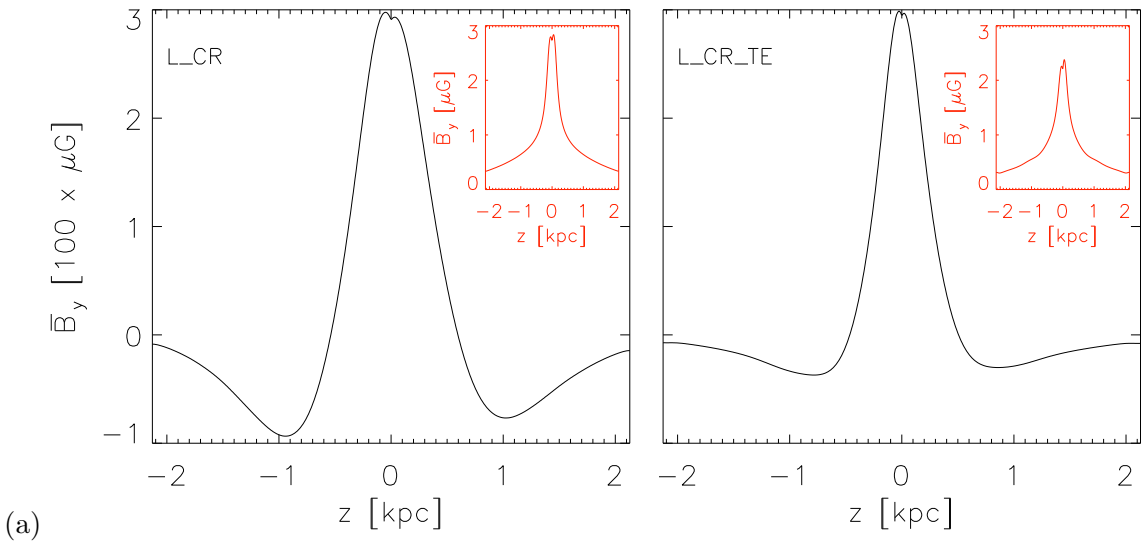

(a)

FIGURE 7.7: Vertical profiles of $\bar{B}_y$ calculated for 1D model L_CR (*Panel left*) and 1D model L_CR_TE (*Panel right*) at 600 Myr. Inset represents the same at 1 Gyr for the corresponding model. $\overline{u_z}(z)$ here is replaced with the approximated linear profiles shown in Figure 7.8 and $\eta_{xy/yx}(z)$ are neglected consistent with case 3 and 4 in Table 7.2

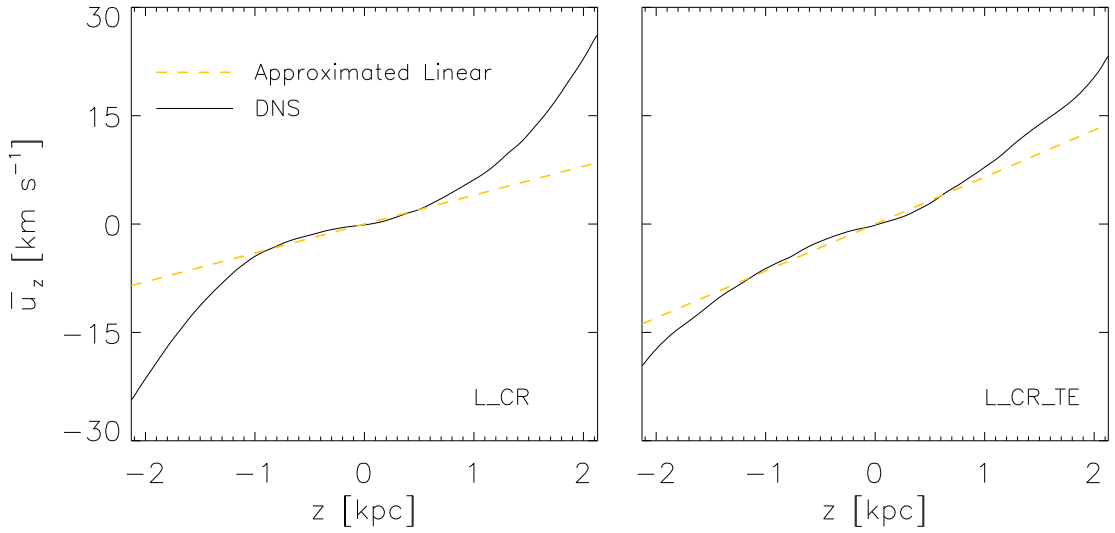

FIGURE 7.8: *Black-solid lines*: Vertical profiles of $\overline{u_z}$ from DNS models. *Orange-dashed lines*: Approximated linear profiles of wind for the parameter space analysis of 1D model. *Panel left* model L_CR. *Panel right* model L_CR_TE.

which however is not sufficient to completely saturate the dynamo. If we furthermore neglect the off-diagonal α terms altogether, mean field saturates after ~ 1 Gyr. However, to deeply investigate this scenario we need a sufficiently longer DNS runs (at least up to 2 Gyr), for various SN rates, and with a larger vertical extent.

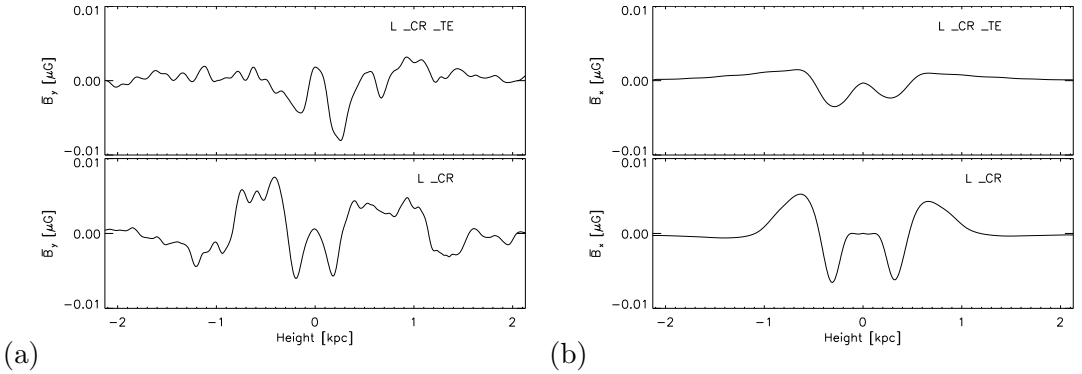

FIGURE 7.9: Vertical profiles of $\bar{B}_x$ calculated for model L_CR (*Panel up*) and model L_CR_TE (*Panel down*) calculated via (a) Direct numerical simulations (b) 1D dynamo simulations.

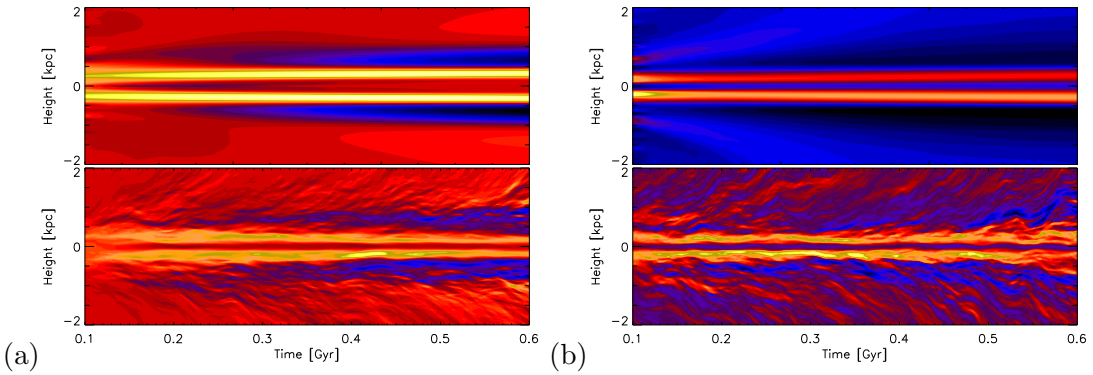

FIGURE 7.10: Space-time diagrams of $\bar{B}_x$ calculated from DNS (*Panel down*) and via 1D simulations (*Panel up*) for, (a) model L_CR (b) model L_CR_TE color code here indicates the strength of mean azimuthal magnetic field normalized with the square-root of magnetic energy.

Chapter 8

Summary and Outlook

In this thesis, we have presented new results of the simulations of stratified galactic ISM along with differential shear and turbulence driven by SN explosions that expel thermal energy and/or cosmic ray energy into ISM. With the simulations including purely thermal SN explosions, we have been able to illustrate the amplification and saturation process of magnetic energy in the context of mean field dynamo mechanism, for varying SN explosion rates. Firstly, we were able to demonstrate that magnetic fields can be amplified up to the equipartition strength with respect to turbulent kinetic energy (with a fast exponential growth time of 100 Myr) within ~ 1 Gyr and may not completely saturate in the dynamical phase. For instance; in models with lower SN rates (model Q and H with 25% and 50% of SN rates respectively; compared to the average SN rate of the Milky Way) magnetic energy continues to amplify, albeit with a declined growth rate (growth time exceeds ~ 1 Gyr), even in the presence of dynamically significant field. For model F with a parameter set consistent with the Milky Way, it appears that magnetic energy amplifies only up to one fifth of the equipartition value and saturates thereafter. Similarly, starting from initial ~ 1 nG values, the regular component of magnetic field evolved to symmetric 'S' mode with a few μG peak strengths and exponential scale-heights of ~ 1 kpc in outer halo, which are notably consistent with the Synchrotron observations [e.g. Krause, 2012, 2014]. However, the values of pitch angles of magnetic field seen in models Q and H ($\sim 10^0$) are smaller than the observed values. In model F, on the other hand ($\sim 18^0$), it is fairly consistent with observations [e.g. Fletcher et al., 2011; Van Eck et al., 2015], mainly in the outer halo region. Unlike previous simulations, our main focus here has been to trace down the origin of different dynamical phase

behaviors of magnetic fields seen at different SN rates and to study its implications on the properties of ISM for different SN rates. We have therefore analyzed the turbulence properties as well as the distribution of ISM in various thermal phases and demonstrated that, these are generally consistent with observations (e.g. observations discussed in Sellwood & Balbus [1999] and Jenkins & Tripp [2011]). However, it must be mentioned that the term 'ISM phases' used here is somewhat more restricted than in the sense that it is in the context of observations, primarily because we have distinguished these phases solely on the basis of temperature and not on explicit chemical composition. Detailed understanding of the morphological features of ISM therefore warrants higher resolution simulations-preferably along with the implementation of chemical networks. Nonetheless, we found these to be in approximate agreement with a few previous high resolution simulations, which are specifically focused on the analysis of ISM properties [e.g. Breitschwerdt et al., 2012; Hill et al., 2012]. This study furthermore revealed that dynamically significant magnetic field backreacts on the ISM and changes its distribution in various thermal phases. It also affects the properties of ISM turbulence such as turbulent velocity, correlation length scales and volume filling fraction of the dense cold ISM phase. As one of our main results, we have been able to demonstrate that in the dynamical phase dynamo coefficients in all models quench an the inverse function of the strength of magnetic energy relative to the turbulent kinetic energy. We have explicitly shown, using the SOCA estimates, that suppression of dynamo coefficients α is a direct consequence of backreaction of the magnetic helicity (Equation 5.15) to the kinetic helicity. These coefficients may be indirectly estimated by combining the observable galactic parameters (turbulent velocity, turbulent eddy scale, vertical length scales, etc.). However, it must be noted that this combination may lead to different estimates for the different mechanisms of dynamo saturation [e.g. Beck, 2015; Vishniac, 2005; Vishniac & Cho, 2001].

Notably, however, using a simple $\alpha\Omega$ dynamo model along with algebraically quenching dynamo coefficients and vertical wind (obtained from DNS data), we were also able to reproduce the entire time evolution of vertical profiles of mean magnetic field components in the kinematic and the dynamical phase. It promptly turned out that the sustained growth of magnetic energy in the dynamical phases of low SN rate models Q and H is consistent with the prolonged turbulent diffusion time scales for quenched dynamo coefficients, which are insufficient to stop the growth of magnetic energy. Whereas,

the dynamical saturation seen in model F is a result of outward advective transport of magnetic flux due to wind. We moreover pointed out that observationally inconsistent small values of pitch angles seen in the dynamical phases of models Q and H can be attributed to the increasing contribution (due to quenching of dynamo coefficients) of azimuthal winding-up in the amplification of $\overline{B_y}$. However, this problem is resolved in model F, in which the saturation is mainly caused by the excessive outward wind, without having to suppress the dynamo coefficients to a significant degree (and pitch angle is $\sim 18^o$). This result provides another approach to rectify a general discrepancy seen between the observed magnitudes of pitch angles and the ones predicted by mean field models. Although it must be mentioned that it is nontrivial to support it with observational evidence in the form of correlation between pitch angles and the outflow velocities. The systematic parameter space analysis of nonlinear dynamo presented by Chamandy & Taylor [2015] complements our result. However, it should be pointed out that they have excluded the quenching of turbulent diffusivity. We further note that this quenching mechanism should be supplemented with constraints arising from the conservation of magnetic helicity [e.g. Sur et al., 2007], which might even substantially contribute in higher magnetic Reynolds number situations [Del Sordo et al., 2013]. This scenario therefore needs to be further tested while including the high density ISM component in numerical simulations, which might be crucial on the smaller length scales. Nevertheless, the remarkable similarity between DNS results and the results of 1D dynamo model justifies this model as a viable subgrid model in the global simulations of spiral galaxies. Such 'hybrid' dynamo simulations [e.g. Gressel et al., 2013] could be useful in predicting the observational consequences of large scale galactic magnetic fields.

In order to explore a further unknown aspect, namely the influence of cosmic rays on the growth of magnetic field, we have separately incorporated the hydrodynamical cosmic rays model along with the magnetic field aligned diffusion. SN explosions are simulated either as localized injections of thermal energy or cosmic rays energy (or both). To verify its effect on the turbulent transport properties, we have compared the outcomes of two models, one including SN explosions containing thermal energy and another with SN explosions including thermal + cosmic rays energy. However, we have not been able to run the simulations up to the dynamical phase yet, which we plan to do in the future. In both of these cases, magnetic energy grows exponentially with e-folding time of ~ 70 Myr [consistent with the simulations by Hanasz et al., 2004, 2009], while the corresponding

mean magnetic field profiles grow to a double peaked symmetric mode. The distinctive feature of cosmic ray models, however, is the enhanced outward wind in the outer halo parts (above $\sim 1\,\mathrm{kpc}$), which is excessive compared to its expected magnitude from the SN rate dependencies obtained in purely thermal SN models (Q, H and F). This may be due to additional CR pressure. Moreover, for model including thermal and cosmic rays energy, the excess thermal part seemingly affects only in the inner part ($|z| < 1\,\mathrm{kpc}$). To analyze the influence of anisotropic cosmic ray diffusion on the turbulent transport processes, we calculate corresponding dynamo coefficients in these direct simulations as well. Noticeably, in cosmic ray models, off-diagonal contribution of α term is nonnegligible, as opposed to the purely thermal SN models. Another distinction in cosmic ray and thermal SN models is the nonuniform contribution of the components of turbulent intensity gradient leading to the anisotropic off-diagonal dynamo coefficient α (which is more pronounced in purely cosmic rays model). Using these values of dynamo coefficients in standard $\alpha\Omega$ model, we were able to reproduce the evolution of $\overline{\mathrm{B}_x}(z)$ and $\overline{\mathrm{B}_y}(z)$ profiles with a remarkable accuracy. The distinctive double peaked shape of mean field profiles turns out to be a combined result of nonnegligible off-diagonal turbulent diffusivity and enhanced wind profiles in the outer halo. We remark that in a more realistic scenario, one should incorporate the energy dependence of cosmic rays diffusion coefficients [e.g. Girichidis et al., 2014], preferably with a bigger box size, to include disc-halo interaction. Observational consequences of this scenario (such as cosmic ray energy spectrum, anisotropies in the high energy cosmic rays distribution, cosmic ray buoyancy, etc. e.g. Blasi & Amato [2012]; Ptuskin [2012]; Strong et al. [2007]), however, can only be inferred from the realistic global galactic simulations. Another unexplored aspect of these simulations is the influence of cosmic rays on ISM properties and its distribution in various thermal components, for which it is necessary to run these simulations up to the dynamical phase and with high resolution.

Appendix A

Non-Fickian Flux Test

Diffusion tensor for the field aligned diffusion process is defined as,

$$K_{ij} = K_{\perp}\delta_{ij} + \left(K_{\parallel} - K_{\perp}\right)\hat{\mathbf{B}}_i\hat{\mathbf{B}}_j\,, \tag{A.1}$$

where $\hat{\mathbf{B}}_i$ and $\hat{\mathbf{B}}_j$ are unit vectors in the direction of i'th and j'th component of magnetic field respectively. For the usual Fickian diffusion approach, gradient of a diffusive flux involves a term $(\nabla \cdot K_{ij}\,\nabla e_c)$. $(\nabla \cdot K_{ij})$, here represents the transport of CR energy perpendicular to field lines (and has dimensions of velocity). As Equation A.1 indicates, this transport term becomes infinite for the diverging gradients of a dyadic product $\hat{\mathbf{B}}\hat{\mathbf{B}}$.

To overcome this problem, we implement a non-Fickian approach, wherein the diffusion flux is obtained via solving a telegraph equation (Equation 2.13), which converges to a Fickian diffusive form for a low Strouhal number limit,

$$St = \frac{(K_{\parallel}\mathcal{T})}{h}\,.$$

A problem of infinite propagation speed is circumvented here, by prescribing a finite correlation time. This is demonstrated by solving a test problem described by Snodin et al. [2006] as follows.

We solve a system of equations Equation 2.1, along with Equation 2.10 (with a non-fickian flux Equation 2.13), in a computational domain of $x, y, z \in \{-\pi : \pi\}$, subject to the following initial conditions:

1. A prescribed magnetic field configuration, $\mathbf{B} = (sin(kx), -sin(ky), 0)$, with $k = 1$.
2. No initial velocity, $\mathbf{u} = 0$, and no back-reaction of CR pressure on the flow (by using $\gamma_c = 1.0$).
3. A constant value of ρ throughout the domain.
4. A Linear initial profile of e_c, given by; $e_c = x + \pi$.
5. Non-Fickian correlation time, $\mathcal{T} = 0.1\, K_{\parallel}^{-1}\, k^{-2}$.
6. Ratio of parallel and perpendicular diffusion coefficients $K_{\parallel}/K_{\perp} \sim 100$.

We apply a constant gradient boundary condition for e_c and $\mathcal{F}_{ci}$, in all directions. Since there is no CR pressure back reacting on the flow, $\mathbf{u}$, ρ, e and $\mathbf{B}$ remain constant; and only e_c evolves with a non-fickian diffusion flux $\mathcal{F}_c$.

Used configuration of $\mathbf{B}$ has an x-point at $(x, y) = (0, 0)$. Moreover an initial gradient of e_c is constant throughout the domain. This scenario under a normal diffusion approximation would lead to a diverging transport term $(\nabla\dot{\mathbf{B}}\hat{\mathbf{B}}\,\nabla e_c)$ at x-point. This problem is tacitly avoided here via a consideration of the finite correlation time $\mathcal{T}$. $e_c(z)$ thus evolves to a symmetric profile within, time $t = 4\mathcal{T} = 40K_{\parallel}^{-1}k^{-2}$, as shown in a contour plot Figure A.1

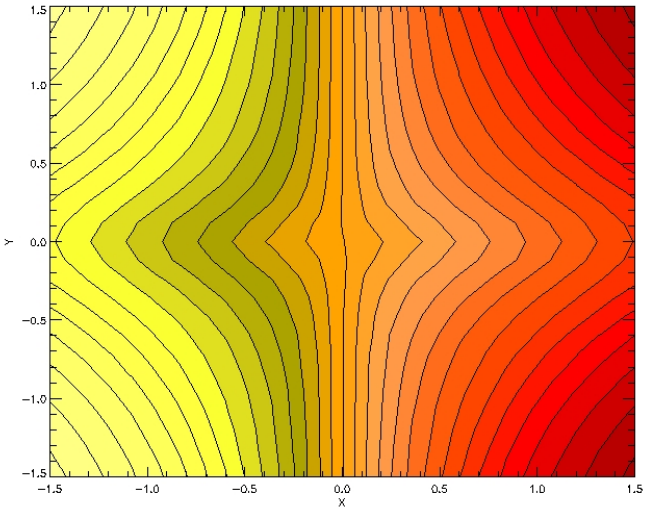

FIGURE A.1: $x - y$ contour of evolved e_c, after $t = 40K_{\parallel}^{-1}k^{-2}$, in a background magnetic field defined by $\mathbf{B} = (sin(kx), -sin(ky), 0)$. By prescribing a finite value for a correlation time $\mathcal{T}$, a Fickian singularity at $(x, y) = (0, 0)$ is avoided, and for the sufficiently small values of $\mathcal{T}$ the profile of e_c approaches to the solution of diffusion equation. Color code is normalized such that the color yellow indicates a minimum value of e_c and the red indicates maximum.

Appendix B

Implementation and Validation

Non-fickian CR flux (Equation 2.13) is defined on grid surfaces, as opposed to e_c, which is defined on the grid (as shown in Figure B.1, with a red dot for $\mathcal{F}_c$ and a blue one for e_c). Hence to calculate the ith component of a non-fickian flux, at a face centered point $\left(i-\frac{1}{2}, j, k\right)$, is necessary to monotonically interpolate the components of ∇e_c on that point as follows.

$$(\nabla_i e_c)_{\left(i-\frac{1}{2},j,k\right)} = \frac{e_{c\,(i,j,k)} - e_{c\,(i-1,j,k)}}{\Delta x}\,, \tag{B.1}$$

$$d_l\, e_c = \frac{\left[\left(e_{c\,(i,j+1,k)} + e_{c\,(i-1,j+1,k)}\right) - \left(e_{c\,(i,j,k)} + e_{c\,(i-1,j,k)}\right)\right]}{2\,\Delta y}\,,$$

$$d_r\, e_c = \frac{\left[\left(e_{c\,(i,j,k)} + e_{c\,(i-1,j,k)}\right) - \left(e_{c\,(i,j-1,k)} + e_{c\,(i-1,j,k)}\right)\right]}{2\,\Delta y}\,,$$

$$(\nabla_j e_c)_{\left(i-\frac{1}{2},j,k\right)} = \frac{d_l\, e_c + d_r\, e_c}{4}\left(1 + \text{sign}\left(d_l\, e_c\; d_r\, e_c\right)\right)\,, \tag{B.2}$$

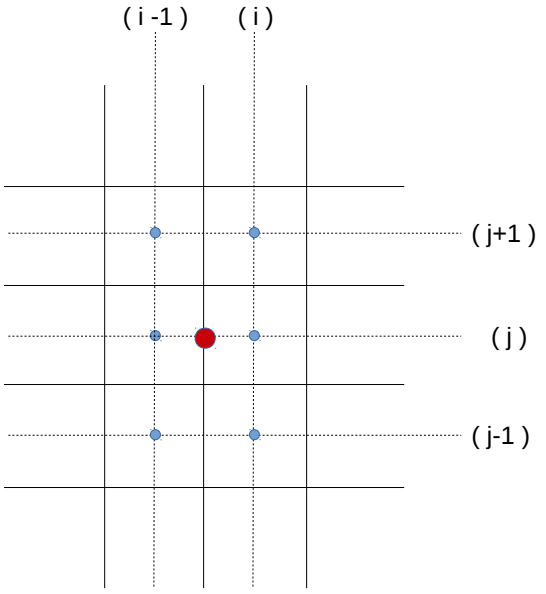

FIGURE B.1: Staggered grid used in NIRVANA, e_c is defined at a grid center (blue dot), and $\mathcal{F}_c$ is defined on a face center (red dot)

$$d_u\, e_c = \frac{\left[\left(e_{c\,(i,j,k+1)} + e_{c\,(i-1,j,k+1)}\right) - \left(e_{c\,(i,j,k)} + e_{c\,(i-1,j,k)}\right)\right]}{2\,\Delta y}\,,$$

$$d_d\, e_c = \frac{\left[\left(e_{c\,(i,j,k)} + e_{c\,(i-1,j,k)}\right) - \left(e_{c\,(i,j,k-1)} + e_{c\,(i,j,k-1)}\right)\right]}{2\,\Delta y}\,,$$

$$\left(\nabla_k\, e_c\right)_{\left(i-\frac{1}{2},j,k\right)} = \frac{d_u\, e_c + d_d\, e_c}{4}\left(1 + \mathrm{sign}\left(d_u\, e_c\;\, d_d\, e_c\right)\right)\,, \tag{B.3}$$

Magnetic field is also defined on the face centers, so the components of magnetic field other than i, are averaged to get their values at $\left(i-\frac{1}{2}, j, k\right)$ as;

$$\mathrm{B}_i{}^{\left(i-\frac{1}{2},j,k\right)} = \mathrm{B}_i{}^{\left(i-\frac{1}{2},j,k\right)}, \tag{B.4}$$

$$\mathrm{B}_j{}^{\left(i-\frac{1}{2},j,k\right)} = \frac{\mathrm{B}_j{}^{\left(i,j+\frac{1}{2},k\right)} + \mathrm{B}_j{}^{\left(i-1,j+\frac{1}{2},k\right)} + \mathrm{B}_j{}^{\left(i,j-\frac{1}{2},k\right)} + \mathrm{B}_j{}^{\left(i-1,j-\frac{1}{2},k\right)}}{4}, \tag{B.5}$$

$$\mathrm{B}_k{}^{\left(i-\frac{1}{2},j,k\right)} = \frac{\mathrm{B}_k{}^{\left(i,j,k+\frac{1}{2}\right)} + \mathrm{B}_k{}^{\left(i-1,j,k+\frac{1}{2}\right)} + \mathrm{B}_k{}^{\left(i,j,k-\frac{1}{2}\right)} + \mathrm{B}_k{}^{\left(i-1,j,k-\frac{1}{2}\right)}}{4}. \tag{B.6}$$

Absolute magnitude of magnetic field at point $\left(i-\frac{1}{2},j,k\right)$ is defined as;

$$mag = \sqrt{\mathrm{B}_i{}^{\left(i-\frac{1}{2},j,k\right)^2} + \mathrm{B}_j{}^{\left(i-\frac{1}{2},j,k\right)^2} + \mathrm{B}_k{}^{\left(i-\frac{1}{2},j,k\right)^2}}, \tag{B.7}$$

and evolution of the ith component of flux $\mathcal{F}_c$ at point $\left(i-\frac{1}{2},j,k\right)$ is defined as;

$$\begin{aligned}
\mathcal{F}_{c\,|i}{}^{\left(i-\frac{1}{2},j,k,t+1\right)} = {} & \mathcal{F}_{c\,|i}{}^{\left(i-\frac{1}{2},j,k,t\right)} \\
& - \frac{\Delta t}{\mathcal{T}} K_{\parallel} \left(\nabla_i e_c\right)_{\left(i-\frac{1}{2},j,k\right)} - \frac{\Delta t}{\mathcal{T}} \mathcal{F}_{c\,|i}{}^{\left(i-\frac{1}{2},j,k,t\right)} \\
& - \frac{\Delta t}{\mathcal{T}} \left(K_{\parallel} - K_{\perp}\right) \frac{\mathrm{B}_i{}^{\left(i-\frac{1}{2},j,k\right)} \mathrm{B}_i{}^{\left(i-\frac{1}{2},j,k\right)}}{mag^2} \left(\nabla_i e_c\right)_{\left(i-\frac{1}{2},j,k\right)} \\
& - \frac{\Delta t}{\mathcal{T}} \left(K_{\parallel} - K_{\perp}\right) \frac{\mathrm{B}_i{}^{\left(i-\frac{1}{2},j,k\right)} \mathrm{B}_j{}^{\left(i-\frac{1}{2},j,k\right)}}{mag^2} \left(\nabla_j e_c\right)_{\left(i-\frac{1}{2},j,k\right)} \\
& - \frac{\Delta t}{\mathcal{T}} \left(K_{\parallel} - K_{\perp}\right) \frac{\mathrm{B}_i{}^{\left(i-\frac{1}{2},j,k\right)} \mathrm{B}_k{}^{\left(i-\frac{1}{2},j,k\right)}}{mag^2} \left(\nabla_k e_c\right)_{\left(i-\frac{1}{2},j,k\right)}
\end{aligned} \tag{B.8}$$

This implementation is validated by analyzing behavior of a relative error in e_c with respect to grid size. For that, we solve Equation 2.10 and Equation 2.13 in a cubical domain of $x, y, z \in \{-L : +L\}$ (where, $L = 0.8\,\mathrm{kpc}$), with five different grid resolutions ($\Delta x = \Delta y = \Delta z = (25\,\mathrm{pc}, 16\,\mathrm{pc}\,12.5\,\mathrm{pc}, 8.33\,\mathrm{pc}\,6.25\,\mathrm{pc})$). Chosen values of the remaining parameters are as follows;

1. $K_{\parallel} = 3.3 \times 10^{-3}\,\mathrm{kpc}^2\,\mathrm{Myr}^{-1}$, and $K_{\perp} = 0$.
2. Initial profile of e_c is a 1D Gaussian (in the direction of z), and with a scale-length of $0.1125\,L$.
3. Constant initial profile of magnetic field in 'z' direction; $\mathbf{B} = (0, 0, 1)$
4. Non-Fickian correlation time $\tau = 2 \times 10^{-4}\,L^2 {K_{\parallel}}^{-1}$.

We calculate the values of converged relative errors in e_c, for each resolution, after time $t = 7\,\mathcal{T}$, and find that they scale quadratically with respect to the grid size, as expected (Figure B.2 (panel left)).

We furthermore compare the evolution of e_c (for the grid resolution of 8.33 pc) with a known analytical solution for the diffusion of a Gaussian function, and we find a remarkable agreement between the both. In Figure B.2 (panel right) we have shown the z profiles of e_c (diamonds), over-plotted on the corresponding analytical solutions (solid lines) at time $t = 7\,\mathcal{T}$ (red color) and at $t = 10\mathcal{T}$ (blue color).

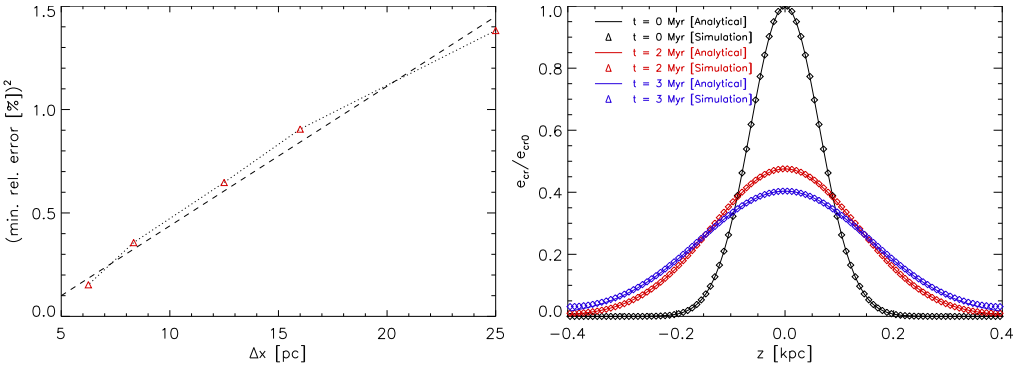

FIGURE B.2: *panel left:* Linear scaling of a square of the relative error in e_c, with respect to grid resolution (with a slope of $0.07\,\mathrm{pc}^{-1}$). *panel right:* z profiles of e_c after times $t = 7\,\mathcal{T}$ (red color) and at $t = 10\mathcal{T}$ (blue color) over-plotted on the corresponding analytical solutions (solid lines).

Appendix C

Additional Tables

Here we document the energy composition for all models in Table 3.1, within the inner disc ($|z| < 0.5\,\mathrm{kpc}$) and in the outer halo ($|z| > 0.5\,\mathrm{kpc}$).

TABLE C.1: Energy composition for all ISM thermal components, in the thermal SN models at the end of kinematic phase, averaged over a full box, and within the inner disc.

	Cold	Cool	Warm	Transition	Hot	Total
model Q						
Full Box						
E_m/E_{kin}	1.0	0.6	0.6	0.3	0.04	0.25
E_m/E_{th}	2.0	0.2	2.5	0.3	0.01	0.11
Inner Disc						
E_m/E_{kin}	1.0	1.2	2.3	0.6	0.03	1.6
E_m/E_{th}	2.0	0.8	1.0	0.6	0.01	0.8
model H						
Full Box						
E_m/E_{kin}	0.5	0.4	0.3	0.06	0.06	0.14
E_m/E_{th}	1.8	0.2	0.2	0.06	0.002	0.09
Inner Disc						
E_m/E_{kin}	0.5	1.0	1.2	0.5	0.03	0.8
E_m/E_{th}	1.8	0.6	0.9	0.5	0.02	0.6
model F						
Full Box						
E_m/E_{kin}	0.1	0.1	0.15	0.04	0.006	0.1
E_m/E_{th}	0.7	0.02	0.02	0.01	0.001	0.05
Inner Disc						
E_m/E_{kin}	0.1	0.5	0.7	0.35	0.04	0.2
E_m/E_{th}	0.7	0.7	0.8	0.3	0.02	0.2

TABLE C.2: Energy composition for all ISM components, at time t, for the models with and without net vertical flux

	Cold	Cool	Warm	Transition	Hot
model QS [$t = 1.1\,\mathrm{Gyr}$]					
Full Box					
E_m/E_{kin}	0.2	0.25	1.5	1.6	0.25
E_m/E_{th}	0.3	0.07	0.6	1.2	0.06
Inner Disc					
E_m/E_{kin}	0.2	0.22	1.2	1.5	0.1
E_m/E_{th}	0.3	0.06	0.5	1.1	0.04
model QSZ [$t = 1.1\,\mathrm{Gyr}$]					
Full Box					
E_m/E_{kin}	0.8	0.3	0.5	0.4	0.06
E_m/E_{th}	1.5	0.1	0.2	0.33	0.02
Inner Disc					
E_m/E_{kin}	0.8	0.3	0.4	0.25	0.03
E_m/E_{th}	1.5	0.1	0.15	0.25	0.01
model QZ [$t = 2.1\,\mathrm{Gyr}$]					
Full Box					
E_m/E_{kin}	1.5	0.29	0.31	0.13	0.03
E_m/E_{th}	1.6	0.1	0.13	0.12	0.007
Inner Disc					
E_m/E_{kin}	1.5	0.1	0.2	0.05	0.002
E_m/E_{th}	1.6	0.05	0.1	0.08	0.001
model AR [$t = 1.5\,\mathrm{Gyr}$]					
Full Box					
E_m/E_{kin}	1.1	0.8	0.7	0.2	0.04
E_m/E_{th}	2	0.25	0.25	0.17	0.06
Inner Disc					
E_m/E_{kin}	1.1	0.5	0.4	0.11	0.007
E_m/E_{th}	2	0.15	0.17	0.12	0.05

Appendix D

Current Helicity

Here we include the space-time contour plots of α_m and α_k along with α_{yy} calculated from DNS, for models H and F.

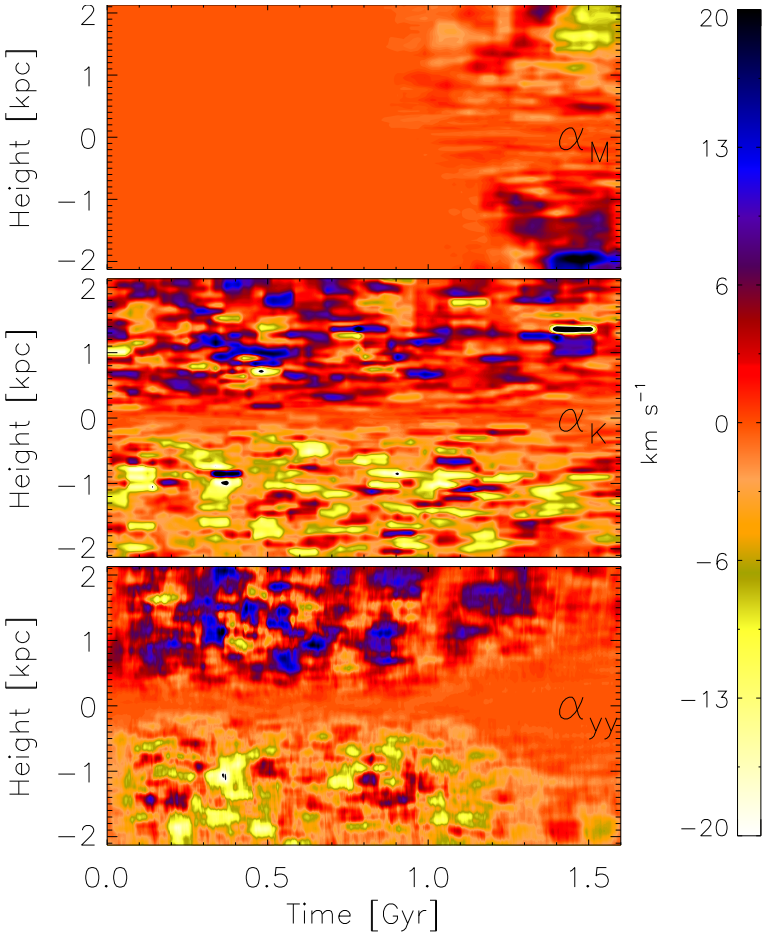

(a)

FIGURE D.1: same as Figure 5.2 but for model H.

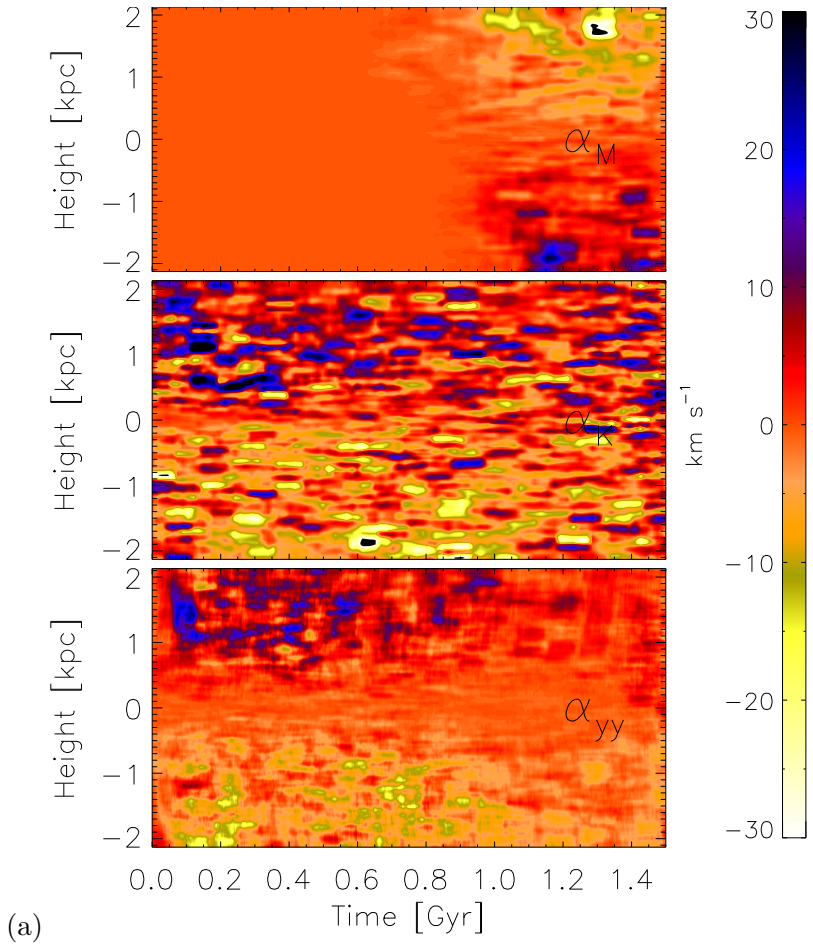

FIGURE D.2: same as Figure 5.2 but for model F.

Bibliography

Abbott, D. 1982, The Astrophysical Journal, 263, 723

Allamandola, L., Tielens, A., & Barker, J. 1985, The Astrophysical Journal, 290, L25

Arbutina, B., Urošević, D., Andjelić, M., Pavlović, M., & Vukotić, B. 2012, The Astrophysical Journal, 746, 79

Balbus, S. A. & Hawley, J. F. 1991, apj, 376, 214

Balsara, D., Crutcher, R., & Pouquet, A. 2001, The Astrophysical Journal, 557, 451

Beck, R. 2001, in The Astrophysics of Galactic Cosmic Rays (Springer), 243–260

Beck, R. 2007, Astronomy & Astrophysics, 470, 539

Beck, R. 2009, Astrophysics and Space Sciences Transactions, 5, 43

Beck, R. 2015, The Astronomy and Astrophysics Review, 24, 1

Beck, R., Brandenburg, A., Moss, D., Shukurov, A., & Sokoloff, D. 1996, Annual Review of Astronomy and Astrophysics, 34, 155

Beck, R. & Wielebinski, R. 2013, in Planets, Stars and Stellar Systems (Springer), 641–723

Bell, A. 1978, Monthly Notices of the Royal Astronomical Society, 182, 443

Bell, A. 2004, Monthly Notices of the Royal Astronomical Society, 353, 550

Bendre, A., Gressel, O., & Elstner, D. 2015, Astronomische Nachrichten, 336, 991

Blandford, R. D. & Ostriker, J. P. 1978, The Astrophysical Journal, 221, L29

Blasi, P. & Amato, E. 2012, Journal of Cosmology and Astroparticle Physics, 2012, 010

Boulares, A. & Cox, D. P. 1990, The Astrophysical Journal, 365, 544

Brandenburg, A. & Sandin, C. 2004, Astronomy & Astrophysics, 427, 13

Brandenburg, A. & Subramanian, K. 2005, Physics Reports, 417, 1

Breitschwerdt, D., de Avillez, M., Feige, J., & Dettbarn, C. 2012, Astronomische Nachrichten, 333, 486

Castellina, A. & Donato, F. 2013, Planets, Stars and Stellar Systems: Volume 5: Galactic Structure and Stellar Populations, 725

Chamandy, L. & Taylor, A. R. 2015, The Astrophysical Journal, 808, 28

Choudhuri, A. R. 1998, The physics of fluids and plasmas: an introduction for astrophysicists (Cambridge University Press)

Chyży, K. 2008, Astronomy & Astrophysics, 482, 755

Chyży, K. T. & Buta, R. J. 2008, The Astrophysical Journal Letters, 677, L17

Crutcher, R. M., Wandelt, B., Heiles, C., Falgarone, E., & Troland, T. H. 2010, apj, 725, 466

Dalgarno, A. & McCray, R. 1972, Annual review of astronomy and astrophysics, 10, 375

de Jong, T. 1977, Astronomy and Astrophysics, 55, 137

De Jong, T. 1980, Highlights of Astronomy, 5, 301

Del Sordo, F., Guerrero, G., & Brandenburg, A. 2013, Monthly Notices of the Royal Astronomical Society, 429, 1686

Draine, B. T. 1978, apjs, 36, 595

Dumke, M. & Krause, M. 1998, in The Local Bubble and Beyond Lyman-Spitzer-Colloquium, Springer, 555–558

Duric, N. 1988, Space Science Reviews, 48, 73

Duric, N. 1999, in Astronomical Society of the Pacific Conference Series, Vol. 168, New Perspectives on the Interstellar Medium, ed. A. R. Taylor, T. L. Landecker, & G. Joncas, 161

Dziourkevitch, N., Elstner, D., & Rüdiger, G. 2004, Astronomy & Astrophysics, 423, L29

Elmegreen, B. G. & Scalo, J. 2004, arXiv preprint astro-ph/0404451

Elstner, D., Gressel, O., & Rüdiger, G. 2008, Proceedings of the International Astronomical Union, 4, 467

Fermi, E. 1949, Physical Review, 75, 1169

Fermi, E. 1954, The Astrophysical Journal, 119, 1

Ferriere, K. M. 2001, Reviews of Modern Physics, 73, 1031

Fletcher, A., Beck, R., Shukurov, A., Berkhuijsen, E., & Horellou, C. 2011, Monthly Notices of the Royal Astronomical Society, 412, 2396

Gent, F., Shukurov, A., Sarson, G., Fletcher, A., & Mantere, M. 2012, Monthly Notices of the Royal Astronomical Society: Letters, sls042

Girichidis, P., Naab, T., Walch, S., & Hanasz, M. 2014, arXiv preprint arXiv:1406.4861

Glatzmaiers, G. A. & Roberts, P. H. 1995, nat, 377, 203

Gressel, O. 2010, PhD thesis, PhD Thesis, 2010

Gressel, O., Bendre, A., & Elstner, D. 2013, mnras, 429, 967

Gressel, O., Elstner, D., & Ziegler, U. 2013, Astronomy & Astrophysics, 560, A93

Gressel, O., Elstner, D., Ziegler, U., & Rüdiger, G. 2008, Astronomy & Astrophysics, 486, L35

Gressel, O. & Ziegler, U. 2007, Computer physics communications, 176, 652

Hale, G. E. 1908, apj, 28, 315

Hanasz, M., Kowal, G., Otmianowska-Mazur, K., & Lesch, H. 2004, The Astrophysical Journal Letters, 605, L33

Hanasz, M. & Lesch, H. 2000, The Astrophysical Journal, 543, 235

Hanasz, M., Wóltański, D., & Kowalik, K. 2009, The Astrophysical Journal Letters, 706, L155

Hathaway, D. H. 2010, Living Reviews in Solar Physics, 7

Hawley, J. F., Gammie, C. F., & Balbus, S. A. 1995, apj, 440, 742

Hill, A. S., Joung, M. R., Mac Low, M.-M., et al. 2012, The Astrophysical Journal, 750, 104

Ivanova, T. S. & Ruzmaikin, A. A. 1977, sovast, 21, 479

Jenkins, E. B. & Tripp, T. M. 2011, The Astrophysical Journal, 734, 65

Joung, M. R. & Mac Low, M.-M. 2006, The Astrophysical Journal, 653, 1266

Kiepenheuer, K. 1950, Physical Review, 79, 738

Kleeorin, N., Moss, D., Rogachevskii, I., & Sokoloff, D. 2002, arXiv preprint astro-ph/0205266

Kleeorin, N., Rogachevskii, I., & Ruzmaikin, A. 1995, Astronomy and Astrophysics, 297, 159

Korpi, M., Brandenburg, A., Shukurov, A., Tuominen, I., et al. 1999, The Astrophysical Journal Letters, 514, L99

Krause, F. & Rädler, K.-H. 2013, Mean-field magnetohydrodynamics and dynamo theory (Elsevier)

Krause, M. 2011, ArXiv e-prints

Krause, M. 2012, in Proceedings of the International Astronomical Union, Vol. 10, Highlights of Astronomy, 399–399

Krause, M. 2014, ArXiv e-prints

Krause, M. 2015, Highlights of Astronomy, 16, 399

Kuijken, K. & Gilmore, G. 1989, Monthly Notices of the Royal Astronomical Society, 239, 605

Kuijken, K. & Gilmore, G. 1989, mnras, 239, 571

Kulkarni, S. R. & Heiles, C. 1988, in Galactic and extragalactic radio astronomy (Springer), 95–153

Lacki, B. C. & Beck, R. 2013, Monthly Notices of the Royal Astronomical Society, stt122

Love, J. J. 2008, Physics Today, 61, 31

Mao, S., McClure-Griffiths, N., Gaensler, B., et al. 2012, The Astrophysical Journal, 759, 25

Mestel, L. & Subramanian, K. 1991, Monthly Notices of the Royal Astronomical Society, 248, 677

Moffatt, H. K. 1978, Field Generation in Electrically Conducting Fluids (Cambridge University Press, Cambridge, London, New York, Melbourne)

Mora, S. C. & Krause, M. 2013, Astronomy & Astrophysics, 560, A42

Ossendrijver, M. 2003, The Astronomy and Astrophysics Review, 11, 287

Parker, E. N. 1955, The Astrophysical Journal, 122, 293

Parker, E. N. 1992, The Astrophysical Journal, 401, 137

Pouquet, A., Frisch, U., & Léorat, J. 1976, Journal of Fluid Mechanics, 77, 321

Ptuskin, V. 2012, Astroparticle Physics, 39, 44

Rädler, K.-H. 2007, Springer, 80, 55

Rädler, K.-H. & Rheinhardt, M. 2007, Geophysical & Astro Fluid Dynamics, 101, 117

Raedler, K.-H., Wiedemann, E., Brandenburg, A., Meinel, R., & Tuominen, I. 1990, aap, 239, 413

Rohde, R., Elstner, D., & Rudiger, G. 1998, Astronomy & Astrophysics, 329, 911

Rüdiger, G. & Hollerbach, R. 2006, The magnetic universe: geophysical and astrophysical dynamo theory (John Wiley & Sons)

Ruzmaikin, A. A., Sokoloff, D., & Shukurov, A. M. 2013, Magnetic fields of galaxies, Vol. 133 (Springer Science & Business Media)

Sánchez-Salcedo, F., Vázquez-Semadeni, E., & Gazol, A. 2002, The Astrophysical Journal, 577, 768

Sarazin, C. L. & White III, R. E. 1987, The Astrophysical Journal, 320, 32

Schrinner, M., Rädler, K., Schmitt, D., Rheinhardt, M., & Christensen, U. 2005, Astronomische Nachrichten, 326, 245

Schrinner, M., Rädler, K.-H., Schmitt, D., Rheinhardt, M., & Christensen, U. R. 2007, Geophysical & Astro Fluid Dynamics, 101, 81

Sellwood, J. & Balbus, S. A. 1999, The Astrophysical Journal, 511, 660

Shapiro, M. M., Silberberg, R., & Wefel, J. P. 1991, Cosmic rays, supernovae and the interstellar medium, Vol. 337 (Springer Science & Business Media)

Shukurov, A. 1998, Monthly Notices of the Royal Astronomical Society, 299, L21

Shukurov, A. 2004, arXiv preprint astro-ph/0411739

Shukurov, A. & Sokoloff, D. 2007, Dynamos: Lecture Notes of the Les Houches Summer School, 251

Shukurov, A., Sokoloff, D., Subramanian, K., & Brandenburg, A. 2006, Astronomy & Astrophysics, 448, L33

Snodin, A. P., Brandenburg, A., Mee, A. J., & Shukurov, A. 2006, Monthly Notices of the Royal Astronomical Society, 373, 643

Sofue, Y., Fujimoto, M., & Wielebinski, R. 1986, Annual review of astronomy and astrophysics, 24, 459

Sokoloff, D., Bykov, A., Shukurov, A., et al. 1998, Monthly Notices of the Royal Astronomical Society, 299, 189

Soward, A. 1978, Astronomische Nachrichten, 299, 25

Soward, A. 1992a, Geophysical & Astrophysical Fluid Dynamics, 64, 163

Soward, A. 1992b, Geophysical & Astrophysical Fluid Dynamics, 64, 201

Spitzer Jr, L. 1990, Annual Review of Astronomy and Astrophysics, 28, 71

Stepanov, R., Shukurov, A., Fletcher, A., et al. 2014, Monthly Notices of the Royal Astronomical Society, 437, 2201

Stix, M. 1975, Astronomy & Astrophysics, 42, 85

Strong, A. W., Moskalenko, I. V., & Ptuskin, V. S. 2007, arXiv preprint astro-ph/0701517

Subramanian, K. & Mestel, L. 1993, Monthly Notices of the Royal Astronomical Society, 265, 649

Sur, S., Subramanian, K., & Brandenburg, A. 2007, Monthly Notices of the Royal Astronomical Society, 376, 1238

Tabatabaei, F., Krause, M., Fletcher, A., & Beck, R. 2008, Astronomy & Astrophysics, 490, 1005

Tabatabaei, F. S., Schinnerer, E., Murphy, E. J., et al. 2013, aap, 552, A19

Tritsis, A., Panopoulou, G. V., Mouschovias, T. C., & Pavlidou, V. 2015, mnras, 451, 4384

Van Eck, C., Brown, J., Shukurov, A., & Fletcher, A. 2015, The Astrophysical Journal, 799, 35

Van Haarlem, M., Wise, M., Gunst, A., et al. 2013, Astronomy & astrophysics, 556, A2

Vishniac, E. 2005, in The Magnetized Plasma in Galaxy Evolution, 177–184

Vishniac, E. T. & Cho, J. 2001, The Astrophysical Journal, 550, 752

Wolfire, M. G., Hollenbach, D., McKee, C. F., Tielens, A., & Bakes, E. 1995, The Astrophysical Journal, 443, 152

Yoast-Hull, T. M., Gallagher, III, J. S., & Zweibel, E. G. 2015, ArXiv e-prints

Zeldovich, I. B., Ruzmaikin, A. A., & Sokolov, D. D. 1983, in New York, Gordon and Breach Science Publishers (The Fluid Mechanics of Astrophysics and Geophysics. Volume 3), 1983, 381 p. Translation., Vol. 3

Ziegler, U. 2008, Computer Physics Communications, 179, 227

Acknowledgements

I would like to express my gratitude to many people who have been with me during the course of my Ph.D.; to all those who supported me, consoled me, offered useful suggestions and insights and assisted me in every possible way. Although it took me a rather long to complete this thesis, I can definitely say at this point that it has been overall an enjoyable and memorable experience. I thank therefore my guide Dr. Elstner for his patience and continuous scientific help. I would also like to thank him and Prof. Steinmetz for giving me this excellent opportunity. I am also thankful to my collaborator Dr. Gressel, from Neils Bohr Institute, Copenhagen, for his scientific help and guidance. Working with Dr. Gressel and Dr. Elstner has truly been a learning experience. The same goes for all my colleagues in DFG research unit.

In addition, I would also like to thank all my colleagues from Villa Turbulenze at AIP, for the insightful and thoughtful discussions. I am grateful to Prof. Denker and Prof. Müller for giving me an opportunity to work as their teaching assistant, which enriched me as a Physics student. I would like to express my sincere gratitude towards Prof. Subramaniyan from IUCAA, Pune and Prof. Pathak from the University of Pune who supervised and reviewed my masters' thesis and introduced me to the exciting field of Cosmic Magnetic Fields. I also thank the administrative staff of AIP for their prompt help and assistance. I would especially like to single out the late Frau Andrea Hans, who helped me right from finding me my first apartment when I landed just as a young kid in Germany. I thank her very much for that.

I am also thankful to all my friends who come from vastly different areas of research like Astrophysics, Quantum Mechanics, Nonlinear Dynamics, Material Science, Mathematics, Chemistry, Geology, Neuroscience, and even Linguistics, with whom I thoroughly enjoyed my social life and many intellectually stimulating discussions.

I am truly thankful to my father and first physics teacher Prof. Bendre and younger sister Ashwini for their sympathetic nature and tremendous support on a personal level. Lastly, I would like to thank my mother Rajashri, who unfortunately passed away just after I had started my PhD, but her wise counsel continues to comfort me to this day. She was an exceptional Hindi teacher and a passionate admirer of Kabir's poetry. I am sure she would have come up with some appropriate verse of his to quote here, to help me express how grateful I am to everyone I have mentioned here.

Selbständigkeitserklärung

Hiermit versichere ich, dass ich die vorliegende Dissertation mit dem Titel "Growth and Saturation of Dynamo in Spiral Galaxies via Direct Simulations" selbständig angefertigt, nicht anderweitig für Prüfungszwecke vorgelegt, alle benutzten Quellen und Hilfsmittel angegeben, sowie wörtliche und sinngemäße Zitate gekennzeichnet habe.

Pune, Nov. 24, 2016

Abhijit B. Bendre: